2016

Detection, Characterization and Mitigation of GNSS Jamming Interference Using Pre-Correlation Methods

Fadaei, Nahal

UNIVERSITY OF CALGARY

Detection, Characterization and Mitigation of GNSS Jamming Interference Using Pre-Correlation Methods

by

Nahal Fadaei

A THESIS

SUBMITTED TO THE FACULTY OF GRADUATE STUDIES

IN PARTIAL FULFILMENT OF THE REQUIREMENTS FOR THE

DEGREE OF MASTER OF SCIENCE

DEPARTMENT OF GEOMATICS ENGINEERING

CALGARY, ALBERTA

APRIL, 2016

Abstract

GNSS civil jammers are small portable sets capable of broadcasting disruptive signals in the GNSS bands. In this research, the effects of different civil jammers on GPS receivers are investigated and some techniques for detection, characterization and mitigation are proposed. Firstly, the presence of jammer signals is investigated. The detection techniques are categorized into power content analysis, power spectral density techniques and normality analysis. After detecting the jammer signal, there is a need to characterize the hostile signal parameters. Herein, different methods are considered which are classified into linear, bilinear and adaptive time-frequency representation methods. Following this, by using the estimated features of the interference signal, a clean version of the received signal is extracted. The output of this section is used as an input to the receiver. The performances of the proposed methods are assessed with different metrics including Carrier-to-Noise spectral density (C/N_0) and frequency and phase lock indicator.

Preface

Some parts of this thesis contain materials from following published papers:

Fadaei, N., A. Jafarnia-Jahromi, A. Broumandan, and G. Lachapelle (2015) “Detection, Characterization and Mitigation of GNSS Jammers Using Windowed HHT” in *Proceedings of ION GNSS+2015* (Tampa, FL, 14-18 Sep), The Institute of Navigation, 9 pages.

Jafarnia-Jahromi, A., N. Fadaei, S. Daneshmand, A. Broumandan, and G. Lachapelle (2015) “A Review of Pre-despreading GNSS Interference Detection Techniques,” in *5th ESA International Colloquium Scientific and Fundamental Aspects of the Galileo*, 27-29 Oct, Braunschweig, Germany, 8 Pages.

Acknowledgements

It is a pleasure to thank those who made this thesis possible. First, I owe my utmost gratitude to my supervisor Professor Gérard Lachapelle for his continuous guidance, financial support and encouragement throughout my M.Sc. studies. I was fortunate to have my graduate studies under his guidance. My sincere gratitude goes to my co-supervisor Dr. Ali Jafarnia-Jahromi for his continuous support, cooperation, valuable discussions and constructive suggestions. His ability to generate new ideas served as a motivation during my research work.

I acknowledge Dr. Ali Broumandan for his support and for being a role model as a talented researcher. I thank the many post-doctoral fellows, and past and current students in the PLAN Group for providing a friendly environment and wonderful experience. My special thanks to Saeed Daneshmand, Tao Lin, Srinivas Bhaskar, Ali Pirsiavash, Ashwitha, Naveen, Niranjan, Thyagaraj, Vimal, Rakesh, Ranjeeth, Srinivas Tantry, Shashi, Laura, Paul, Maryam and Lingran for providing me a home away from my home environment.

This thesis would not have been possible without the support and encouragement of my mother, father, sisters Nehzat and Noushin and unconditional love and support of my loving husband Ahmad.

Dedication

To my beloved husband,

Ahmad

Table of Contents

List of Tables

List of Figures and Illustrations

List of Symbols, Abbreviations and Notations

ADC	Analogue to Digital Converter
AGC	Automatic Gain Control
ARMA	Auto Regressive Moving Average
C/A	Coarse Acquisition
CD	Cohen Distribution
CW	Continuous Wave
CWD	Choi-Williams Distribution
CWI	Continuous Wave Interference
DSSS	Direct Sequence Spread Spectrum
DWT	Discrete Wavelet Transform
EMD	Empirical Mode Decomposition
FFT	Fast Fourier Transform
FIR	Finite Impulse Response
FM	Frequency Modulation
FrFT	Fractional Fourier Transform
FWT	Fast Wavelet Transform
GNSS	Global Navigation Satellite System
GoF	Goodness of Fit
GPS	Global Positioning System
HHT	Hilbert Huang Transform
HOS	Higher Order Spectral
IF	Intermediate Frequency
IIR	Infinite Impulse Response
IMF	Intrinsic Mode Function
JNR	Jammer to Noise Ratio
LMD	Local Mean Decomposition
MP	Matching Pursuit
OS	Open Service
PSD	Power Spectrum Density
RFI	Radio Frequency Interference
SNR	Signal to Noise Ratio
STFT	Short Time Fourier Transform
TFARMA	Time-Frequency Autoregressive Moving Average
TFD	Time Frequency Distribution
TFR	Time Frequency Representation
VCO	Voltage Controlled Oscillator
WT	Wavelet Transform
WVD	Wigner-Ville Distribution
*	Conjugate operator
η_{IF}	Digital Gaussian noise component
f_s	Sampling frequency
f_D	Frequency offset
f_{int}	Frequency of IF interference

T_{sw}	The sweep time of a chirp
i_{IF}	Digital interference component
N	Number of samples in each window
P_{int}	Interference power
R_c	Chirp rate
t	Time
$x[n]$	ADC output samples
$x(t)$	Received signal
J / N_0	Jammer power to noise spectral density ratio
$\phi_{t,f}$	Basis function
Ψ	Analyzing Wavelet function
ν	Auxiliary function of Meyer Wavelet
ω_k	k th angular frequency
I_i	i th IMF of HHT
$\tilde{I}_i$	Hilbert transform of i th IMF
Z_i	Analytical signal for the i th IMF
r_n	Residuals components
Ω	Gaussian Chirplet function
α	Rotation angle of FrFT Kernel Function
$O(\ )$	Computational complexity

Chapter One: Introduction

GNSS has been incorporated into civilian life by developing hundreds of applications affecting most aspects of life from cell phones and wristwatches to road transportation, railways, shipping containers, control of movement of aircraft and other vehicles at airports. Moreover, future systems like automated highways and lane control systems will be added to these applications. Such a wide range of application has made GNSS receivers a tempting target for intentional disruption or distortion. The increase in GNSS-integrated systems has created a proportional rise in concern for their vulnerability to jamming and interference.

1.1 GNSS Interference Signals

Radio frequency (RF) signals from any undesired source that are affecting a GNSS receiver are considered interference (Kaplan et al 2006). Despite the fact that navigation signals have a direct-sequence spread spectrum (DSSS) signal structure, which gives them an intrinsic robustness against interference signals, they are received by receiver antenna at a very low power level. Hence, these signals are vulnerable to in-band interference signals (e.g. Landry et al 1997). RF interference can cause decreased or loss of accuracy, reliability, integrity, and availability of signals. Generally, RF interference is categorized into either narrowband or wideband depending on whether its bandwidth is large or small relative to the bandwidth of the desired GNSS signal (Kaplan et al 2006). They also can be classified as intentional and unintentional according to their sources.

1.1.1 Intentional Interference

This kind of interference is due to sources that intend to deny service. The intentional interference sources can be grouped into three main sources, namely jamming, spoofing and meaconing. Among them jamming is the most common type. Jamming is an intentional emitted signal that tries to prevent the receiver from acquiring and tracking the authentic signals in the area covered. There are different types of RF jammers including single tone, chirp, pulse, narrowband and broadband signals (Mitch et al 2011). However, single tone and swept waveforms are more commonly used by jammers. Spoofing is a deceptive interference which tries to mislead its target from true navigation. In this case, a basic receiver will consider the counterfeit signal a real one. Spoofers intend to deceive the receiver without being recognized. The meaconing is composed of receiving, delaying and re-broadcasting the GNSS signal in the same frequency as the real signal to confuse the target navigation system.

1.1.2 Unintentional Interference

This kind of interference corresponds to the case of accidental interference and is created by external sources. There is a large number of telecommunication and electronic systems such as mobile satellite networks, FM/television transmitter harmonics, some personal electronic devices, and ultra-wideband radars which can transmit RF power in the GNSS receiver band. Another type of interference is multipath reflection generated by terrestrial reflectors.

1.2 Background and Motivation

In the years to come, GNSS applications will be modernized to hopefully reject multipath (Irsigler et al 2005), intra- and inter-system interference (Titus et al 2003) and external interference generated by spurious emissions of some electronic devices. Many technical improvements are occurring for GNSS, such as increasing the signal strength and number of frequencies. These methods will reduce the effect of interference signals but may not eliminate them.

Civil jammers are capable of broadcasting disruptive interference signals in the GNSS bands, block the reception of navigation signals in their vicinity and degrade the performance of the GNSS receivers. Although the use of civil jammers is illegal, there is much evidence of their usage (Mitch et al 2011). Such jammers are easily accessible (Bauernfeind et al 2012) and considering their impact on the accuracy and availability of GNSS services, their detection and mitigation are becoming increasingly important.

Currently, most available civil jammers transmit hostile signals in the L1/E1 band where the open GPS C/A service and the Galileo OS are provided. However, it is a trivial task for a jammer to adjust its center frequency and bandwidth in order to intrude new GNSS services such as L5/E5 as well as other systems such as GLONASS and BeiDou. In order to protect these navigation services, it is necessary to detect, characterize and mitigate interference sources effectively and reliably. Implementation of interference suppression algorithms within receivers would provide a higher level of integrity and continuity.

1.3 Relevant Research

There are several interference countermeasure methods proposed in the literature. An interference suppression unit (ISU) is an interference countermeasure system that consists of interference detection, characterization and mitigation sections. The ISU can generally be divided into two categories, namely pre-despreading and post-despreading techniques. Pre- despreading methods are applied before the correlation stage whereas post-spreading methods are implemented after correlation operation in the receiver (i.e. after either of acquisition, tracking or navigation solution blocks). In this research, a pre-despreading ISU is proposed. The main advantage of pre-despreading techniques is that they do not require any modification to the receiver structure. Moreover, pre-despreading methods provide a better estimation of the jammer than post-despreading since they have access to raw input signals. The downside is high processing burden due to high sampling rate before correlation. A general structure of the ISU proposed in this research is shown in Figure 1-1.

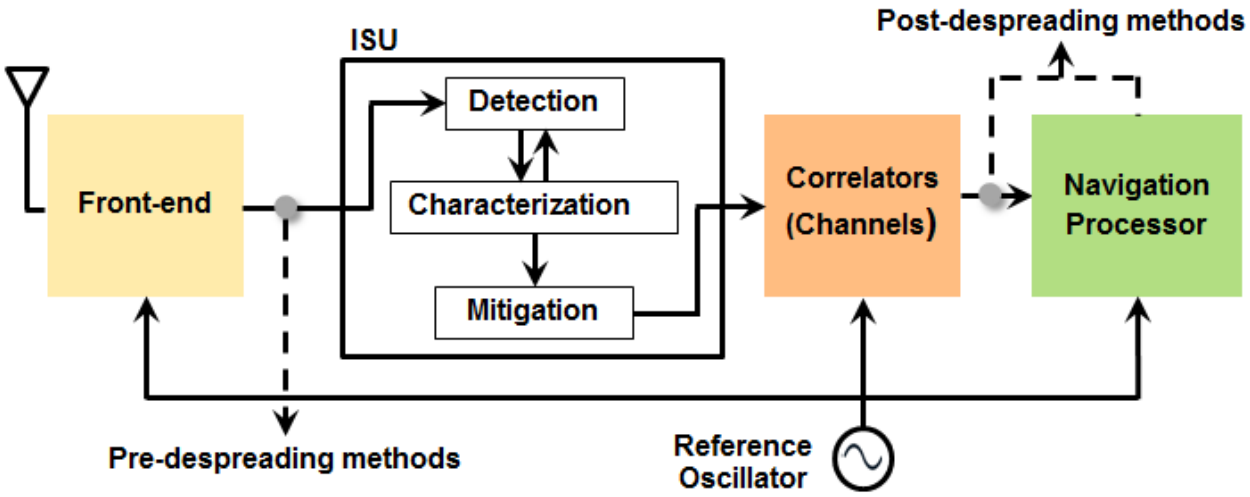

Figure 1-1 Proposed ISU structure in a GNSS receiver

The order of execution in an ISU is detecting the jammer, characterizing its parameters and eliminating the jammer's effect taking advantage of those parameters. In some of the algorithms, which will be described in the following chapters, the detection and characterization blocks are not separable and are performed simultaneously. That is why there is a two-way arrow between detection and characterization blocks in Figure 1-1.

1.3.1 Interference Detection

The first stage of ISU operation is interference detection. Several interference and jammer detectors for GNSS receivers have been proposed during the last few years based on the properties of the received signals.

This research provides an overview on the vulnerability of GPS receivers to chirp-type interference signals. Various interference detection methods will be proposed where each method focuses on a specific feature of interference signals including power content (e.g., power-law detector method), power spectral density (e.g., Welch analysis and Marti method) and input signal statistical distribution (e.g., Kurtosis method and goodness of fit method). The performance of the detection methods introduced will be evaluated in terms of detection capability, detection latency, sensitivity to interference power and computational complexity.

Power content analysis is one of the simplest and widely used techniques for pre-despreading interference detection. It measures the received signal power during a finite time interval and compares the received power with a predefined decision threshold. Power detector is optimal in the Bayesian sense (Marti 2004) for detection of

a white Gaussian signal embedded in additive white Gaussian noise (AWGN) when the expected values of signal and noise powers are known (Urkowitz 1967).

Power spectral density (PSD) analysis is performed in another class of pre-despreading detectors. In this regard, partial band and narrowband interference signals are more observable in the Welch analysis using a spectrogram operator. The spectrogram is the optimal detector when the interference is a sinusoid of unknown amplitude, phase and frequency (Kay 2009).A frequency domain metric was introduced by Marti (2004) and evaluated by Balaei (2007) for detection of a narrowband CW interference signal being captured by a GPS receiver. In this method, the spectral components were estimated by an averaged FFT. Balaei (2007) assumed that the noise parameters (mean and variance of the power) are estimated from an assessment window that is not subject to any interference in order to set a decision threshold and achieve a pre-determined false-alarm probability. The actual test statistic of Balaei (2007) is based on the difference between the estimated mean values obtained from the assessment window and the evaluation window normalized by the estimated variances.

Another class of interference detection techniques focuses on analysing the statistical distribution of the received signal samples and try to detect the presence of jamming signals based on the histogram deviation from the expected Normal distribution (Motella et al 2014). In this regard, Kurtosis and goodness of fit (GoF) methods will be used in this research. Kurtosis is a statistical parameter that describes the shape of a distribution. It denotes how ‘peaked’ a distribution is, compared to a Normal distribution (Roo et al 2007). GoF compares the histogram of the received samples with the interference free signal histogram. The algorithm involves assigning the data values into

discrete amplitude bins and counting the number of samples belonging to each bin (Motella 2014).

Another interference detection indicator is monitoring the gain value of the controllable gain amplifier before the analogue signal is fed into the ADC. This block is essential for a receiver because the input signal to the ADC is required to be matched to the dynamic range of the ADC to guarantee quantization accuracy. Therefore, within the GNSS receiver implementation an automatic gain control (AGC) circuit is normally implemented to adjust the gain value based on the output of the ADC. When the ADC input signal is higher than the nominal level due to the presence of excessive RFI, the AGC will try to lower the gain value of the adjustable gain amplifier and this rapid variation can be an indicator for the presence of interference. Several measures were proposed by Ndili et al (1998) and Borowski et al (2012) for RFI detection based on AGC variations. A detector based on the AGC level is very similar to an energy detector and therefore inherits its advantages and disadvantages. Furthermore, there are other pre-correlation techniques such as detection with antenna arrays (Montgomery et al 2009) that are out of the scope in this research.

1.3.2 Interference Characterization

The next step in ISU is to characterize the RF interference. Several methods have been proposed so far to address this issue. This research investigates various time-frequency analysis methods. They break down a received signal into several parts of finite duration. Each part of the input signal is analyzed independently.

Time-frequency interference characterization methods can be classified based on their structure and approach to the estimation problem. They can be linear, bilinear or adaptive as discussed in this section. In this research, jammer parameters such as bandwidth, sweep time and chirp start frequency are determined by characterization section.

Most of the resent GNSS papers on jammer characterization have used linear time-frequency analysis. Linear time-frequency representation is essentially a process to decompose signals into a weighted sum of a series base localized in both the time and frequency domain. Among linear time-frequency methods, the short time Fourier transform (STFT) is a commonly used one. It extracts the signal's features using a window function and Fourier transform. STFT splits the non-stationary signal into small segments that can be assumed as stationary. This is achieved by multiplying the signal to a window function that is limited in time and applying FFT operation to it. Another sophisticated technique used for linear time-frequency analysis is the Wavelet transform. In comparison to the STFT, the Wavelet transform provides more flexibility on time and frequency resolutions. In the STFT, the window width is the same for all locations in the time-frequency plane whereas in the Wavelet transform the window width is variable. The Wavelet transform uses long windows at low frequencies and short windows at high frequencies; therefore it has a higher frequency resolution at lower frequencies and higher time resolution at higher frequencies. The S-transform is another linear time-frequency analysis method that is deduced from short-time Fourier and Wavelet transforms. It provides frequency dependent resolution while maintaining a direct relationship with the Fourier spectrum.

Bilinear time-frequency distribution is a signal energy distribution in the time-frequency domain. Wigner-Ville distribution (WVD) is the basis for bilinear time-frequency distribution. Although the Wigner-Ville distribution has better resolution than most of the linear time-frequency representation methods (Cohen 1995), its applications are very limited due to the existence of the cross-term interference. The cross-term often obscures the useful pattern of the time-dependent spectra. Hence, reducing the cross-term interference without destroying the desired properties of the signal has been a challenging issue in bilinear time-frequency analysis (Qian et al 1993). Cohen distribution methods are intended to remove the WVD cross terms by smoothing the Wigner-Ville distribution through time and frequency shifting using a kernel function (Cohen 1995). In this research a Choi-Williams kernel function is proposed due to its compatibility with chirp-type jammers.

Adaptive time-frequency representation methods can be categorized into parametric and non-parametric methods. The basis of a parametric time-frequency analysis is a dictionary. A time-frequency dictionary is a collection of parameters through which the chirp signal is characterized. This method decomposes the input signal based on the approximations of its components parameters. Herein, a matching pursuit (MP) method is proposed as an adaptive parametric time-frequency technique. Adaptive non-parametric analysis approaches for jammer characterization are completely signal-driven and there is no need to construct any basis to match the signal components. In this research, the Hilbert-Huang transform (HHT) is used among adaptive non-parametric Time-frequency representation methods.

1.3.3 Interference Mitigation

Time-frequency mitigation techniques usually rely on characterization parameters. This research investigates several mitigation techniques, namely Fractional Fourier transform (FrFT), Wavelet packet decomposition (WPD), Hilbert-Huang Hough transform (HHHT) and notch filtering. The FrFT is one of the most commonly used chirp-type mitigation methods. It can be seen as a generalization to the Fourier transform introduced by Namias (1980) and is mathematically defined by McBride et al (1987). Briefly, FrFT rotates the signal in the time-frequency plane. Hence, it measures the angular distribution of the signal's energy in this plane (Ozaktas 1996). Compared to the classical Fourier transform, FrFT results in a significant performance gain due to the additional degree of freedom that is the order of the transform.

The WPD is derived from Wavelet transform. The mitigation is performed by comparing the achieved time-scale domain with a mask representing the time-scale domain of an estimate of the received GNSS signal in an interference free environment and according to a desired false alarm probability. The jamming excision is performed, blanking all the coefficients in the time-scale domain crossing the mask (Musumeci et al 2015).

The HHHT method employs the HHT characterization output as the input to the Hough transform in order to obtain more precise chirp parameters. The Hough transform is a pattern recognition method for calculating the number of points that satisfy a parametric constraint (Duda et al 1972). In this research, the constraint represents a straight line as the chirp-type jammers have a linear time-frequency relationship.

Notch filtering is one of the simplest and most practical solutions for RFI mitigation (Lung et al 2011). Notch filtering is in fact a time-domain implementation of a band-stop

filter whereby its rejection band is adjusted according to the instantaneous frequency content of the jammer.

1.4 Thesis Objectives and Contributions

Up to now, several methods have been proposed in order to characterize the signal instantaneous time-frequency properties. There are key drawbacks in linear time-frequency analysis approaches. Firstly, in order to apply these methods, the input signal must be divided into several pseudo-stationary sections. Hence, the user must have a priori information about the signal characteristics to set a proper window size. Secondly, the time-frequency resolution depends on the window size. If it is required to closely localize the time instant of higher frequency components, a shorter time window must be used. On the contrary, if the goal is to pinpoint the frequency location of lower frequency components, a longer time window is chosen. Because of the Heisenberg uncertainty principle (Nam 2013), the finest time location and the best frequency resolution cannot be reached at the same time. Hence, these methods suffer from non-adaptability. In other words, they are appropriate to analyze quasi-stationary signals with constant features in each window, but are not suitable to analyze highly transient signals such as bursts. Moreover, in case of WT it is difficult to select an optimal Wavelet basis for a specific input signal.

Non-linear time-frequency approaches have been proposed to overcome the shortcomings of linear methods for non-stationary signals in order to achieve a better time-frequency resolution. Cohen distribution, HHT and MP are presented herein as non-linear approaches. Among the bilinear methods, the Cohen distribution assumes that the interference signal is a non-stationary process, along with GNSS jamming

signal structure. Moreover, choosing a proper kernel function improves the time-frequency resolution.

Adaptive time-frequency methods such as HHT and MP have several advantages compared to conventional linear algorithms such as STFT and WT. Firstly, they compute IMFs/residuals directly from the input data and no assumptions are made for the basis functions (as opposed to the case of STFT, WT and ST). Hence, they do not impose any condition on the time-frequency variations of the input signals and adaptively change the resolution to match the signal requirements. Secondly, it is not required to introduce a predefined window size as these methods analyze the whole data set at the same time. Hence they will be investigated in this research. No previously publicly available papers exist at this time on their use for the application at hand.

Among different types of RF jammers, single tone and swept interferences are the most commonly used ones by civil jammers. Bauernfeind et al (2012) and Mitch et al (2011) presented observations of these types of interference signals at L1 and L2 frequencies. In addition, Mitch et al (2011) provided the maximum allowable jammer-to-signal ratio for commercial GPS receiver to work properly. Most of the jamming mitigation techniques (e.g. Mitch et al 2012) are based on linear time-frequency representation of the interference. These methods require some a-priori information about the interference features in order to properly overcome them. However, in practice, there might be various types of jamming signals that are unknown to a receiver and there is not enough a priori information about them. To characterize these types of jamming signals, some type of adaptive processing method is needed. There is a limited work on

implementing adaptive time-frequency analysis techniques without any primary knowledge about the jammer's characteristics.

In this work, in order to understand the interference structure, the RF jammers are modeled. Then applicable countermeasures are developed. As mentioned before, one of the drawbacks of pre-despreading interference detection techniques is proper threshold selection. Optimal threshold determination requires knowledge of signal characteristics and the noise probability distribution function. Several methods have been proposed so far for RF interference detection and each of them is associated with a kind of threshold setting. Herein, various thresholding methods will be implemented and compared with each other and analyzed in terms of complexity and required detection time.

Another part of this work focuses on implementation of several well-known adaptive pre-despreading interference suppression techniques and investigation of their advantages /disadvantages and applications. This research extends the concept of time-frequency characterization by eliminating a need for a priori information about interference and by employing adaptive time-frequency analysis methods. Linear time-frequency representations suffer from adaptability due to fixed window size. Moreover, they have limited time-frequency resolution as it was explained in the previous section. In contrast, adaptive time-frequency techniques increase the time-frequency resolution and are not dependent on the observation window size. Hence, a practical adaptive algorithm based on non-linear time-frequency signal analysis will be chosen for chirp-type jammer characterization.

In order to mitigate the jammer signals by using calculated interference features, several excision methods based on direct excision and subtraction algorithms will be considered. The input signal (which is contaminated with a RF jammer) is fed into the characterization unit that can be either a linear or a non-linear time-frequency characterization technique. Interference excision is performed by a threshold-masking operation that extracts the interference part of input signal.

Finally, to evaluate the performance of the proposed method, GPS data collection and analysis scenarios will be conducted. The received signals will be corrupted (combined) using a single tone and chirp jammer generated by a signal generator. On the receiver side, an NI RF front-end will be utilized to collect raw IF samples. Moreover, a clean version of the GPS signals will also be collected for performance comparison. Figure 1-2 illustrates the data collection block diagram.

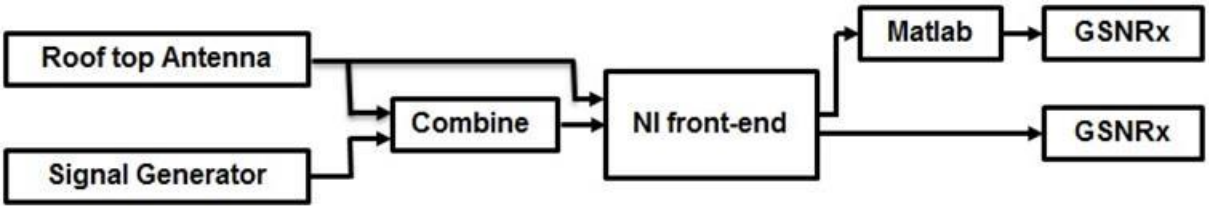

Figure 1-2 Block diagram of data collection

Therefore, the main goals of the proposed research can be summarized as follows:

1) Modeling of different kinds of civil RF jammers.
2) Proposing a jammer detection method with low complexity and fast decision time.
3) Implementing adaptive time-frequency characterization methods considering no a priori information about jammer features.
4) Implementing a time-frequency interference excision technique by jammer signal synthesis and subtraction to mitigate the interference effect.

1.5 Thesis Outline

The thesis consists of six chapters. The rest of the thesis is organized as follows:

• Chapter 2 introduces t GNSS interference models and assesses their impacts on receiver performance. Then, GPS jammers are analyzed according to their availability, categories, affected frequencies, and antennas. Finally, different types of civil jammers are modeled and investigated in these categories.

• Chapter 3 presents several pre-despreading algorithms suitable for the detection of jammer signals based on the power content analysis, PSD analysis and the normality techniques. These methods are investigated and evaluated according to their latency, detection probability for various jammer powers and window length as well as computational complexity. Moreover, a new goodness of fit algorithm is proposed for statistical jamming detection without requiring pre-calibration.

• Chapter 4 focuses on GNSS various pre-despreading interference characterization methods. Linear, bilinear and adaptive time-frequency representation of the chirp-type jammer properties will be investigated. The performance and computational complexity of these methods will be inter-compared and their advantages and limitations will be discussed.

• Chapter 5 aims at mitigating RF interference using pre-despreading methods. Different interference mitigation methods for civil jammers will be proposed and evaluated. Performance assessment will be performed through processing real GPS L1/CA data exposed to different chirp jammers.

• Conclusions and future work will be provided in Chapter 6.

Chapter Two: GNSS Interference

GNSS signals have limited transmitting power and are very weak due to the long signal propagation distance from satellites to a receiver near or on the earth surface. Thus, they can easily be interfered with in-band harmonics of radio frequency (RF) signals used in other communication and ranging systems. A signal from any undesired source received by a GNSS receiver is known as interference (Kaplan et al 2006). GNSS interferences can be generated intentionally (which are called RF jammers) or unintentionally due to other communication links such as radio and TV broadcasting. They lead to positioning accuracy deterioration or even unavailability. Thus, interference detection and mitigation is one of the major tasks in GNSS signal processing. Thus, this research focuses on these problems and addresses possible solutions, especially in the case of jammer signals.

This chapter first presents a review of GNSS signals and receiver structure. Subsequently, an overview of different types of civil GPS jammers, their mathematical models and classification is provided.

2.1 GNSS Signal Structure

GNSS provides continuous, worldwide positioning. Two GNSS systems are currently in full operation, namely GPS, developed by the U.S. Department of Defence (DoD), and the Russian GLONASS. Europe’s Galileo navigation system is expected to provide a full and highly accurate global service by 2020. In addition, the Chinese Compass (Beidou) has begun its service to customers in the Asia-Pacific region and plans to begin global service in 2020.

Civilian GNSS signal characteristics are thoroughly discussed and widely available in the literature (Parkinson et al 1996, Kaplan et al 2006). There are several signals that are transmitted by GPS satellites in the L1, L2, and L5 frequency bands (Kaplan et al 2006). In this research, only the GPS L1 C/A signal is considered since all jammer nullification techniques are inherently independent of signal carrier frequency.

2.1.1 Front-end

Figure 2-1 shows a general GNSS receiver hardware structure. This is according to the common hardware circuitry used in many commercial GNSS receivers. An antenna receives the electromagnetic wave and converts it into an electrical signal. In a generic GNSS receiver, signal conditioning components perform amplification, filtering, frequency down-conversion and quantization. A Low Noise Amplifier (LNA) amplifies the very weak signal so that other RF components can detect and process it. The down-converter uses the synthesizer output (which can be L1, L2 or L5 carrier) to bring the signal spectrum down in vicinity of baseband. IF filtering is required to eliminate out of band signals which may otherwise interfere with the GNSS signals.

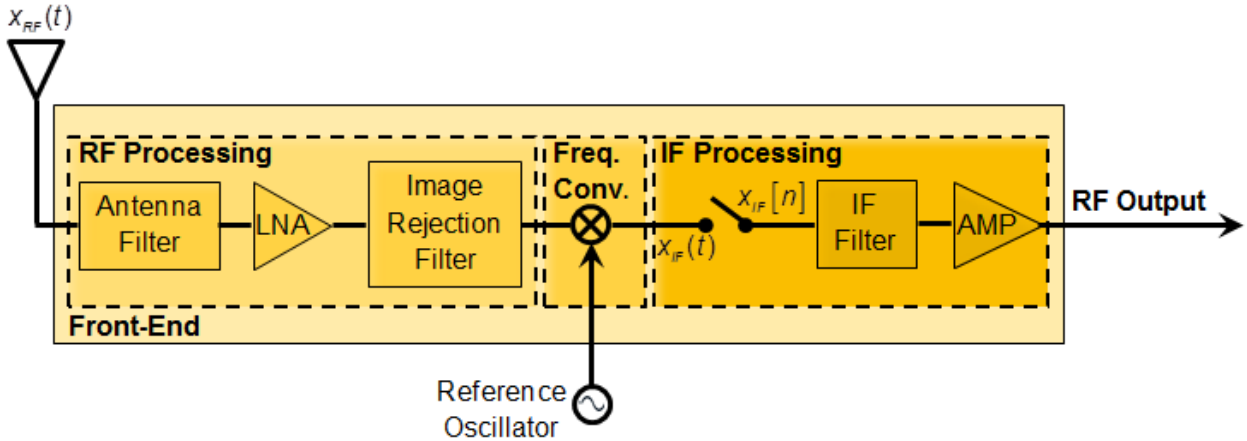

Figure 2-1 GNSS receiver schematic - Hardware section

2.1.2 Baseband Signal Processing

A general structure for GNSS baseband signal processing is shown in Figure 2-2. Baseband processing can be done either in hardware or software. Usually software processing is preferred due to higher flexibility and easier upgrade capability. The baseband processing section of a receiver is composed of four different components, namely pre-despreading signal conditioning, acquisition, tracking and PVT.

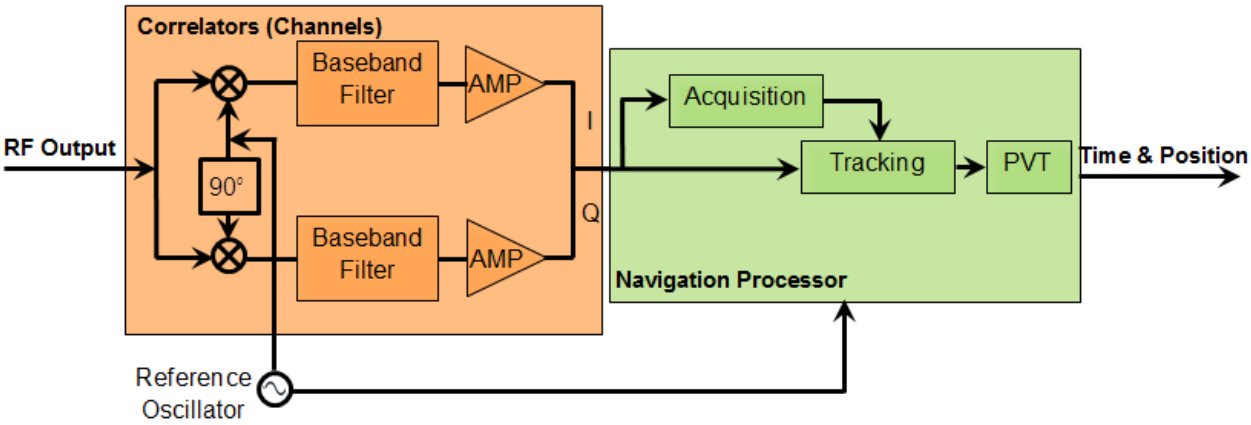

Figure 2-2 GNSS receiver schematic - Software section

Signal conditioning is the first step in GNSS baseband processing. It consists of signal conditioning filters. The main purpose of this block is to filter any out-of-band interfering signal, convert IF samples into complex (or real) baseband samples, and adjust signal amplitude levels such that ADCs can optimally quantize and sample the received signal. Signal acquisition encompasses both the detection and estimation problem. As a detection problem, it determines which satellites (which are distinguished by their unique PRN codes) are in view of the receiver. From the estimation perspective, the acquisition process tries to figure out the parameters associated with each of the detected satellites. These parameters are code delay and carrier Doppler frequency.

Although acquisition algorithms may differ in the way of estimating the incoming signal frequency and code phase, they handle input signal as a two dimensional search problem. First, it chooses a particular satellite as a search candidate. This determines which PRN code is used for acquisition. Then, a combination set of Doppler frequency offsets and code phase is used to generate a local replica signal that matches the Doppler frequency and code phase of the incoming signal. The size of the search space for Doppler frequency is a function of the line of sight velocity between the receiver and satellite as well as the receiver's clock offset. In the case of a static receiver, the conventional Doppler frequency offset and code phase search space used to acquire a GPS L1 C/A signal are ± 5 kHz with a 666 Hz spacing, and 1023 chips with a 0.5 chip spacing (Tsui 2005).

By testing different Doppler and code phase combinations, a correlation peak appears. Satellites detection is based on the correlation amplitude value. If the amplitude exceeds a predetermined threshold, the satellite is available. The maximum correlation occurs in the case that the chosen delay and Doppler pair resembles the most to true values. To perform a correlation function that describes the above, most sophisticated acquisition algorithms use a FFT algorithm to speed up the above mentioned 2D search.

After the acquisition process is fulfilled, tracking begins. Signal tracking allows a GNSS receiver to continuously estimate the incoming signal frequency, code phase and carrier phase. This permits the receiver to generate fine satellite Doppler, pseudorange and carrier phase observations used for navigation. Moreover, navigation data bits can be extracted after the incoming signals are tracked and carrier/code wipe-off are done in

this block. This data bits are used later in PVT section to calculate satellite positions, velocities and time offsets.

The main purpose of the PVT section is to provide continuous user position, velocity and precise time. To this end, a non-linear system of equations based on satellites observables (pseudoranges and pseudorange rates) and satellites information (from navigation data) should be solved. Generally, two different methods can be employed to solve these non-linear navigation equations, namely least-squares adjustment (LS) and extended Kalman filtering (EKF).

2.1.3 GNSS Jammer Suppression Techniques

The techniques dealing with RFI in a GNSS receiver can be divided into pre-despreading and post-despreading techniques. As shown in Figure 2-3, pre-despreading algorithms use the raw signal samples that are available at the output of the receiver front-end. In contrast, post-despreading techniques are applied after the correlation process. They can be applied to different sections of the navigation processor including acquisition, tracking and navigation processing. The main benefit of pre-despreading methods is that they don’t require modification of the receiver structure. The downside is high processing requirements due to high sampling rate before correlation.

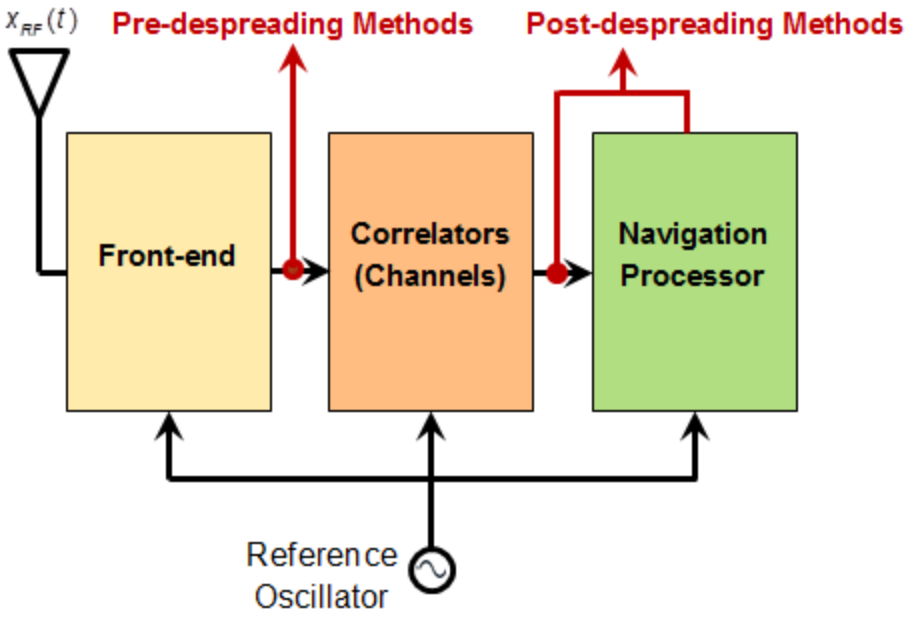

Figure 2-3 Possible locations for jammer suppression techniques in a GNSS receiver

2.2 GNSS Signal Model

The received signal is composed of different components. As shown in Figure 2-4 it contains signals of all GPS satellites in view. In addition, environmental and receiver internal noise are added to the signal mainly due to thermal noise generated in electrical devices and sky noise. Another component of received signal is interference. There are various sources of interference such as multipath, which exists due to satellite signal reflection from nearby objects, and radio frequency interference. Intentional RFI, also known as jamming, consists of hostile signals that adversely impact receiver operation.

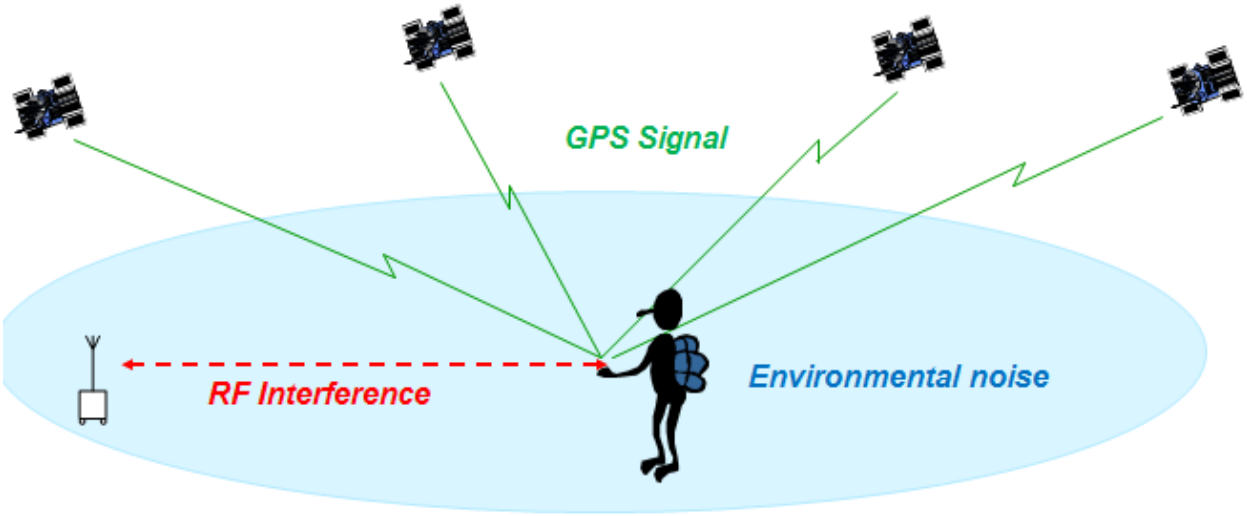

Figure 2-4 Generic GNSS receiver situation

GNSS signals at the receiver antenna contaminated with RF interference can be represented by

$$x_{RF}(t) = \sum_{l=1}^{S_{sv}} s_{RF,l}(t) + i(t) + \eta(t) \qquad (2.1)$$

where S_{sv} is the number of visible satellites, $s_{RF,l}(t)$ comprises the l^{th} satellite received GNSS signal, $i(t)$ is an interfering signal and $\eta(t)$ denotes additive white Gaussian noise (AWGN). Before acquisition and tracking block, the signal is down-converted into an intermediate frequency, sampled and quantized in the receiver front-end. Therefore, the composite received signal at the output of ADC is (Borio 2010)

$$x_{IF}[n] = x_{IF}(nT_s) = \sum_{l=1}^{S_{sv}} s_{IF,l}(nT_s) + i(nT_s) + \eta(nT_s) \qquad (2.2)$$

where T_s is the sampling frequency. Moreover, $i(nT_s)$ and $\eta(nT_s)$ are the digital interference and the digitized Gaussian noise components. In the rest of this thesis, the

satellite index is omitted for the sake of simplicity. For the single digitized GNSS signal affected by noise and interference, the received signal is

$$x_{IF}[n] = \sqrt{2P_s}\,d(n - n_0) \times c(n - n_0) \times \cos(2\pi(f_{IF} + f_D)nT_s + \phi_0) + i[n] + \eta[n] \quad (2.3)$$

where P_s is the received GNSS signal power. d and c denote the data modulation and spreading code with chip duration of T_c. $n_0 = \tau_0 / T_s$ is called digital code delay where τ_0 represents the initial code phase. In addition, f_{IF} is the IF frequency f_D representing the Doppler shift and ϕ_0 is the code delay.

2.3 Received GPS Signal Power

Several factors such as transmitter and receiver antenna gains and space propagation loss impact the received signal power. The GNSS transmitted power is approximately 27W (Misra et al 1996). The received power of Equation (2.3) is given by

$$C = \frac{2 * P_s}{2} = \frac{A_s^2}{2} \quad (2.4)$$

where A_s is the amplitude of the received signal. The typical antenna gain for consumer-grade receivers is from -5 dBic[1] to 4 dBic, depending on the satellite elevation angle seen at the receiver antenna. Thus, the received signal power at the receiver antenna output is approximately -158.5 dBW (GPS ICD, 2000).

[1] dBic: dB (isotropic circular) – The forward gain of an antenna above the gain of a circularly polarized isotropic antenna.

2.4 Thermal Noise

The noise $\eta(t)$ is assumed to be a zero-mean stationary additive white Gaussian noise process with power spectral density (PSD) $N_0/2$ [W/*Hz*]. Moreover, the spectral characteristics of the discrete-time random process $\eta[n]$ depend on the filtering type, and the sampling adopted in the front-end. If sampling frequency is based on $F_s = 2B_{IF}$ is adapted, the IF signal and noise are sampled at the Nyquist rate where B_{IF} is the bandwidth of the front-end. In this case, the noise variance can be calculated by

$$\sigma_{IF}^2 = E\left\{\eta^2[n]\right\} = B_{IF}N_0 = \frac{F_s}{2}N_0 \qquad (2.5)$$

2.5 RF Interference

The main and most important issue with RFI is service denial. In most situations, service outage is dangerous or costly. Ground based augmentation systems (GBAS) for aviation, continuously operating reference station networks for various positioning services, and synchronization problem in power grids are a few examples in which GNSS outages are devastating.

In a less destructive case, jammers can affect the acquisition and tracking stages of a receiver which results in reduced accuracy. However, this performance degradation depends on jammers type and power, its distance to receiver, and receiver structure. For instance, long time GPS outages in integrated GPS/INS receivers increase INS errors and introduce biases in the results which degrade navigation accuracy. Hence, RF interference is a challenging and significant issue. In general, RF interference can be classified based on different parameters (Kaplan et al 2006). Table 2-1 shows a list

of RFI along with their types and sources. From one point of view, they can be classified based on their bandwidths into narrow, partial-band, and wide-band with respect to authentic GNSS signals. With regards to source, RFI are divided into intentional and unintentional transmitter. Considering signal structure and modulation type, interference sources can be classified into continuous wave, amplitude modulation (AM), frequency modulation (FM), phase modulation (PM), pulse modulation, chirp, or matched spectrum.

Furthermore, Table 2-1 provides a list of real jammer examples. One of the major unintentional interference sources is CW. For example, any imperfection in the local oscillator of a general purpose transmitter may lead to spur leakages which translate into one or more CW interferences. This situation depends on the local oscillator quality and RF synthesizer structure. Improper shielding is also another reason for CW interference. Moreover, radio, television and microwave communication links can also introduce narrow to wide band interference with different modulations. This situation is more destructive in low-cost receivers which are not generally effective at image rejection in their RF mixers. Therefore, signals with centre frequency even far from GNSS frequencies can come into a GNSS band after down-conversion. Likewise, pulse interference is also generated due to pulse-based communications and ranging systems such as ultra wide band (UWB), radar and distance measuring equipment (DME) in aviation.

For intentional interference cases, RF jammers, GNSS repeater and spoofers can be considered as hostile transmitters. The primary goal of a jammer is to deny receiver operation. For example a driver of a transportation fleet may be motivated to hide

his/her position by jamming the receiver mounted on his vehicle; or a fishing vessel crew would like to jam the GPS installed on the ship and go fishing in forbidden zones. Personal privacy devices (PPDs) are small and low cost versions of RF jammers. PPDs will be discussed in Section 2.6.

Table 2-1 RF interference classification

Instances	Modulation	Source	Bandwidth
LO spurs leak-through, improper in-board shielding	CW	Unintentional	Narrow
Harmonicas from radio broadcasting	AM/FM	Unintentional	Narrow/ Moderate
UWB communication, Radar systems, Distance Measuring Equipment (DME), Tactical Air Navigation (TACAN)	UWB/pulse	Unintentional	Wide
TV broadcasting, microwave links, Spread Spectrum Comm.	AM/FM/PM	Unintentional	Wide
Personal Privacy Devices (PPDs)	CW/chirp/pulse	Intentional	Narrow/ Moderate Wide
GNSS repeater, Pseudolites, Spoofers, Self-Interference (Intra-System Interference)	Matched Spectrum	Unintentional or Intentional	Wide
Inter-System Interferences (e.g. GPS and Galileo)	Other GNSS Spectrums	Unintentional	Wide

2.6 Overview of Civil GPS Jammers

There are small/low cost jammers for civilian purposes known as personal privacy devices or civil GPS jammers. These kinds of jammers transmit high power signals within the GNSS frequency band. Examples of these jammers are shown in Figure 2-5.

Figure 2-5 Civil (low cost) jammers

In the following, mathematical models for RF jammers are shown. These models are used for the development of interference suppression techniques.

2.6.1 Civil Interference Classification

The focus of this research is civilian chirp-type jammers that are commonly used by personal privacy devices. Although it is possible to have more sophisticated jammers such as matched spectrum or CDMA-type signals, the main focus is on narrowband and chirp type jammers that are easily accessible at a low cost and can generate a serious threat against GNSS receivers. Some interference analyses (e.g. Kraus et al 2011, Mitch et al 2012) have shown that most available civil jammers are chirp signals and similar structures. Some instances of available civil jammers are depicted in Figure 2-5. These jammers can be classified into three groups according to their spectral characteristics, namely continuous wave signals, chirp signal with one/multi saw-tooth function(s) and chirp signal with burst frequency.

2.6.1.1 Group I: continuous wave narrowband jammers

The jammers, which can be plugged directly into the cigarette lighter of a car, generate this kind of interference. The structure of the jammer's device includes a voltage-controlled oscillator (VCO) which generates a fixed frequency. Figure 2-6 shows the instantaneous frequency and output of CW interference. As shown, CW interference is a narrowband interference including a pure sinusoidal tone with a fixed frequency. The CW interference is represented by

$$i[n] = \sqrt{2P_{\text{int}}}\sin\left(2\pi f_{\text{int}} n T_s + \phi_{\text{int}}\right) \tag{2.6}$$

in which f_{int} is the interference frequency. The transmitted interference amplitude P_{int} is assumed to be constant. Herein, ϕ_{int} is a random initial phase uniformly distributed in the interval $(-\pi, \pi]$ and T_s is the sampling frequency.

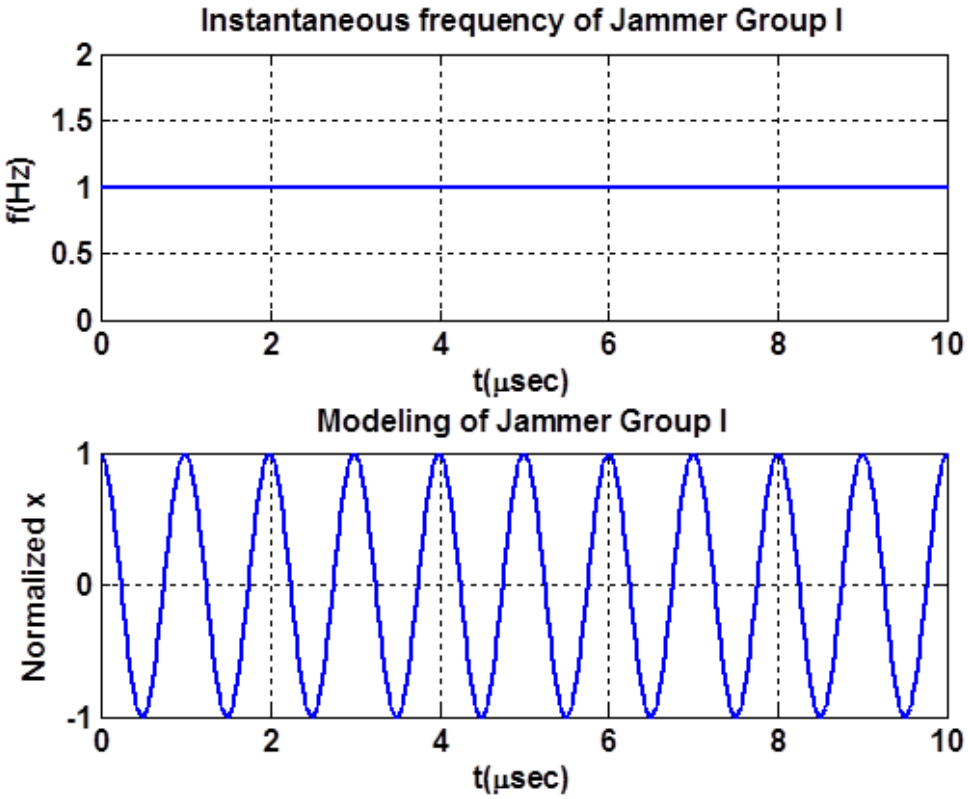

Figure 2-6 Simulation of instantaneous frequency and output of CW jammers

2.6.1.2 Group II: chirp signal with one/multi saw-tooth function(s)

These jammer signals are the most popular civil jammers (Mitch et al 2012, Bauernfeind et al 2012). As shown in Figure 2-7 and reported by Bauernfeind et al (2012), the generic construction of a civil jammer chirp signal is usually done by a voltage controlled oscillator (VCO) with an input voltage of at least one saw-tooth function. The instantaneous frequency is equivalent to the voltage input for the VCO within the civil jammers.

Mitch et al (2012) surveyed the signal properties of commercial GPS jammers based on experimental data and characterized the available civil GPS jammer signals.

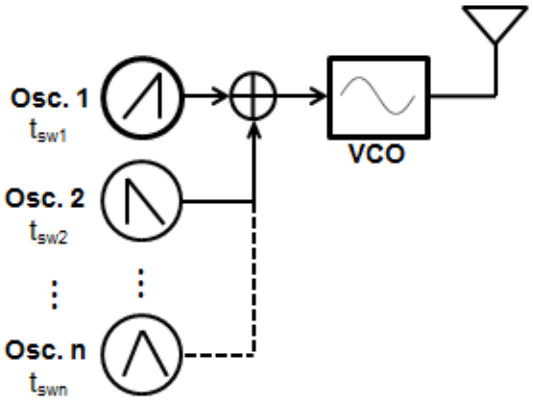

Figure 2-7 Schematic of the internal structure of a civilian jammer of Group 2

In general, a chirp signal is a sinusoid function whose frequency linearly changes over time. The jammers features such as sweep time (T_{sw}), bandwidth (BW) and centre frequency (f_0) are shown in Figure 2-8. According to Mitch et al (2012), the sweep rate of the jammers on average is about 1×10^{12} Hz/s.

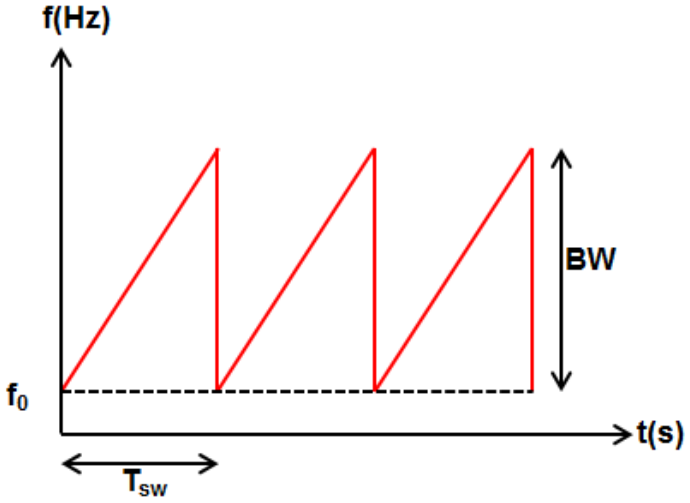

Figure 2-8 Time-frequency presentation of a chirp signal

Hence, the chirp signal with one saw-tooth function used in this research is modeled as

$$i[n] = \sqrt{2P_{\text{int}}}\sin\left(2\pi n T_s\left(\mathrm{F}_{saw}\right) + \phi_{\text{int}}\right) \tag{2.7}$$

where P_{int} is the interference signal power and ϕ_{int} is the initial phase. Once the signal is sampled through ADC, F_{saw} can be expressed as

$$\mathrm{F}_{saw} = f_0 + \frac{R_{c_i}}{2F_s} n = f_0 + \frac{\Delta f}{2} n \tag{2.8}$$

where f_0 denotes the initial frequency of the interference. R_{c_i} and F_s refer to sweep rate of the interference and the sampling frequency. The sweep period of a chirp is T_{sw}. Hence, the frequency of the chirp type interference is modeled as

$$f_n = f_0 + \Delta f \times \mathrm{mod}(n, \lfloor T_{sw} \times F_s \rfloor) \tag{2.9}$$

Figure 2-9 shows the instantaneous frequency and output of a chirp interference with one saw-tooth function. The sweep rate is set to $1 \times 10^{12} Hz/\mathrm{s}$ and the initial frequency is configured to be zero.

In case of multi saw-tooth functions, Equation 2.9 must be modified to

$$\mathrm{F}_{saw,i} = f_{0,i} + \frac{R_{c_i}}{2F_s} n = f_{0,i} + \frac{\Delta f_i}{2} n \tag{2.10}$$

where $\mathrm{F}_{saw,i}$ is the instantaneous frequency for each saw-tooth function.

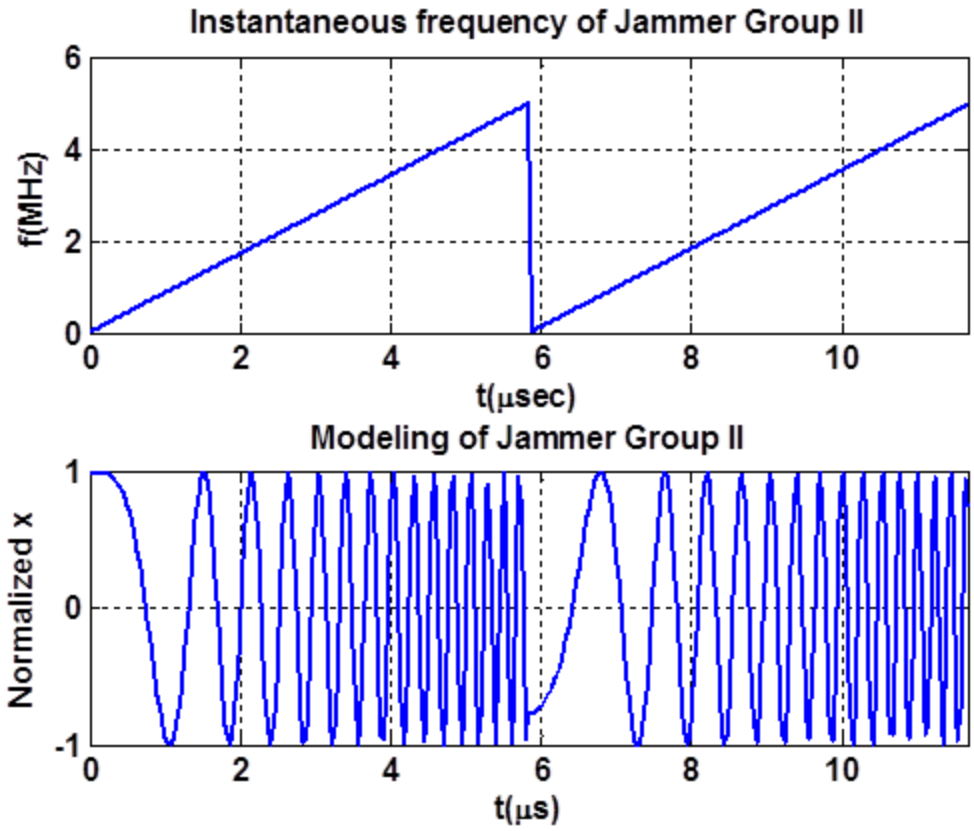

Figure 2-9 Simulation of instantaneous frequency and the output of chirp jammers with one saw-tooth function

The interference is calculated by

$$i[n] = \sqrt{2P_{\text{int}}} \sin\left(2\pi n T_s \left(\sum_{i=1}^{S_{saw}} \mathrm{F}_{saw,i} \right) + \phi_{\text{int}} \right) \qquad (2.11)$$

The notations are the same as in Equation 2.6 and S_{saw} is the number of saw-tooth functions.

Figure 2-10 shows an example of the instantaneous frequency and the output of a chirp interference with multi saw-tooth functions.

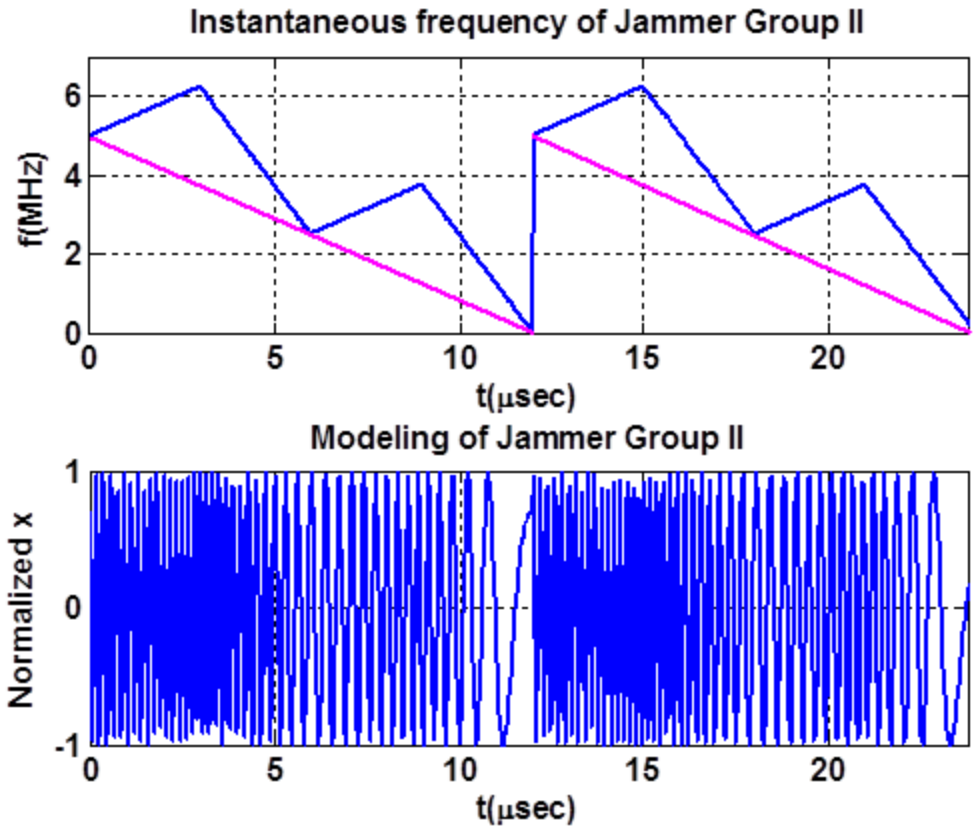

Figure 2-10 Instantaneous frequency and output of chirp jammers with multi saw-tooth functions

2.6.1.3 Group III: chirp signal(s) with frequency bursts

This group is the most complex one with several oscillators controlling the VCO. The signal structure is similar to Group II, however there are bursts of wideband noise added to the VCO output frequently for a very short time frame. Figure 2-11 shows the instantaneous frequency and the output of a chirp interference frequency burst. Within a short time window without any burst, its time-frequency behavior is similar to the chirp jammer with multi saw-tooth functions. Figure 2-12 shows this jammer behaviour over a longer time.

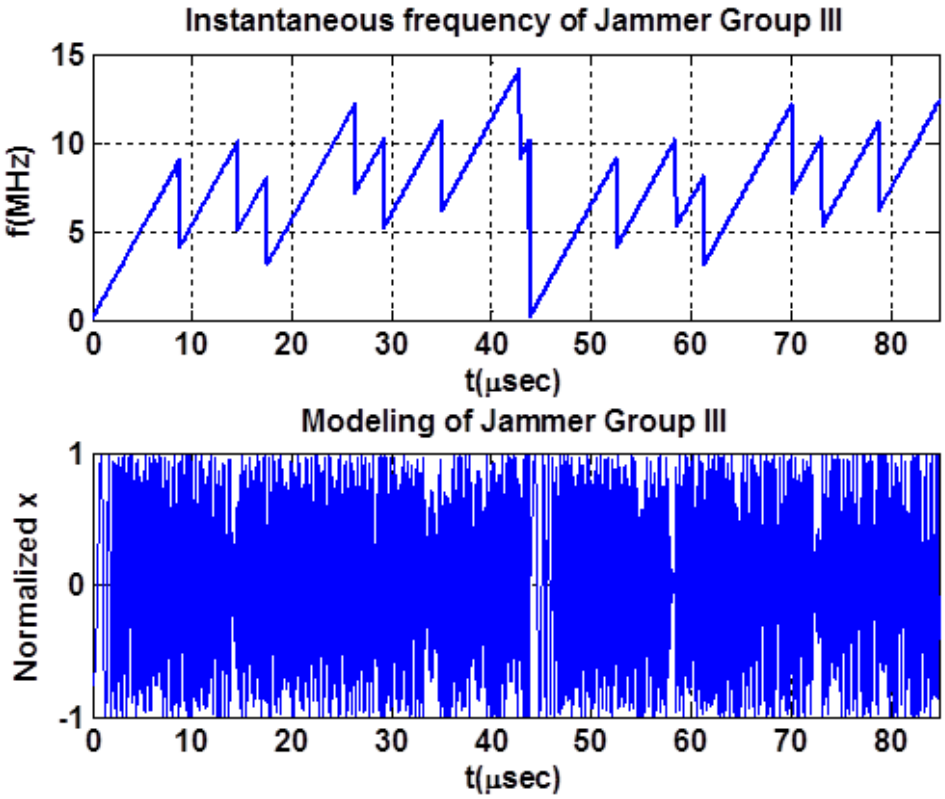

Figure 2-11 Simulation of Instantaneous frequency and output of chirp jammers with frequency burst within a short time

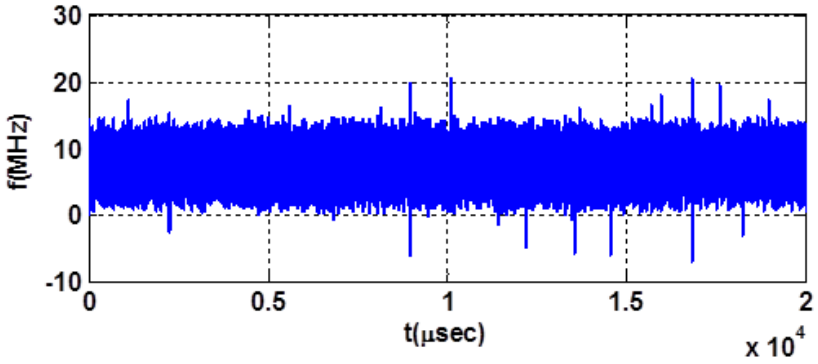

Figure 2-12 Simulation of Instantaneous frequency of chirp signal with frequency burst for a long time

2.6.2 Jammer-to-Noise Ratio

To classify the effectiveness of a jammer, the jammer-to-noise ratio (JNR) is defined as

$$JNR = 10\log_{10}\left(\frac{P_{\text{int}}}{P_{noise}}\right) \tag{2.12}$$

in which P_{int} and P_{noise} are the jammer and noise power. The sampling rate $F_s = 1/T_s$ of the IF signal is equal to twice that of the IF front-end bandwidth, B_{IF}. The JNR can be defined as (Abdizadeh 2013)

$$JNR = \frac{P_{\text{int}}}{\sigma_n^2} = \frac{\frac{1}{2}A_{\text{int}}^2}{\sigma_n^2} = \frac{A_{\text{int}}^2}{F_s N_0} \tag{2.13}$$

where A_{int} is the amplitude of the jammer's signal. For multiple-interference cases, *JNR* is defined by interference components (Abdizadeh 2013):

$$JNR = \frac{J}{N} = \frac{\sum_{i=1}^{M} A_{\text{int,i}}^2}{2N_0 B_{IF}} \tag{2.14}$$

2.6.3 Duty Cycle

The duty cycle is defined for signals with a periodic on-off characteristic. In general, duty cycle is the percentage of one period in which a signal is active. In the jammer concept, the duty cycle is defined as the percentage of the time that the jammer is active and is given by (Bauernfeind et al 2014)

$$DC = \frac{BW_{front-end}}{BW_{jammer}} \tag{2.15}$$

in which the bandwidth of available chirp jammer signals varies from 10 MHz to 30 MHz. Figure 2-13 illustrates some duty cycles for different receiver and jammer bandwidths.

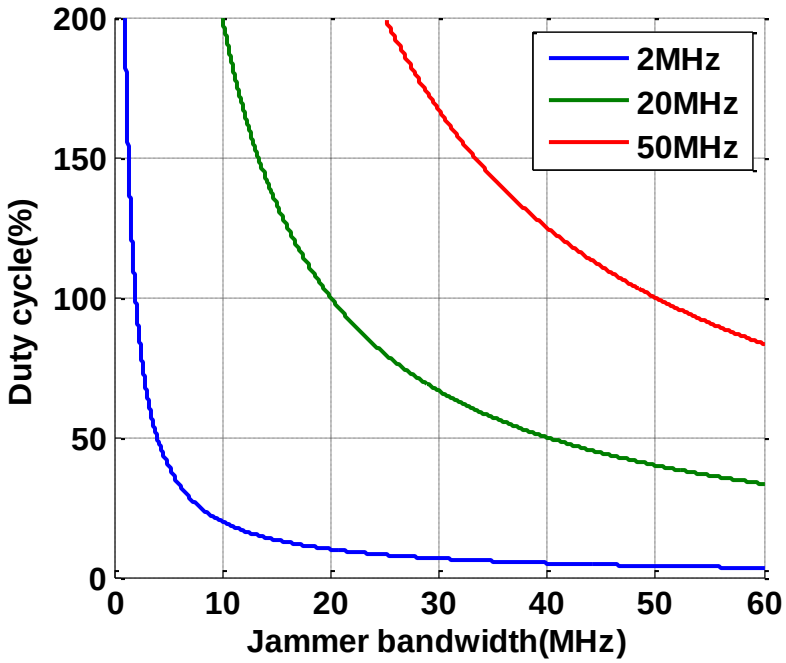

Figure 2-13 Duty cycle for different receiver and jammer bandwidth combinations

2.6.4 Availability and Claims

Devices claiming to jam or block GPS signals are widely available through a number of websites, although their possession and use is illegal (in Canada). The cost of these devices ranges from a few tens of dollars to several hundreds. Their effective ranges are from a few metres to several tens of metres. However, as shown by Mitch et al (2012), their actual effective ranges are significantly greater. Moreover, power consumption range from a fraction of a Watt to several Watts.

2.6.5 Jammer Antennas

There are two types of antenna used by civil jammers so far, namely monopole antennas and short helical antennas, the former being the most common. Helical antennas have approximately the same gain pattern as monopole antennas. However, they have a wider antenna bandwidth as compared to monopole antennas. Mitch et al

(2012) showed that the antennas on jammer's broadcasts have linearly polarized radiation, as opposed to GPS satellites which broadcast right-hand circularly polarized signals. The polarization mismatch will cause some loss in received jammer power at the receivers, which typically use right hand circularly polarized antennas. However, this loss is insignificant considering the jammer power with respect to GNSS signal power.

Chapter Three: GNSS Interference Detection Based on Pre-Correlation Methods

3.1 Introduction

The increased probability of RFI propagation in various GNSS bands necessitates the development and implementation of RFI suppression units to avoid deterioration of GNSS signals. There is a need for ensuring that harmful interference to GNSS with a potential impact on safety is prevented and, if possible, promptly removed should it occur. The first step of the suppression unit is detection. In this chapter, the principle of several detection techniques along with their characteristics, performances and complexities are presented.

This chapter first reviews detection theory. Subsequently, an overview of detection methods based on power content, PSD (power spectral density) analysis and normality methods is provided. Then, the performance of the detection methods is evaluated and compared in term of their ROC curves, detection probability versus window length, and detection probability versus jammer power. Finally, the computational complexity of different methods is compared and a summary of their performance is reported.

3.2 Detection Theory

The concept of detection theory has been a well-studied topic for several decades. The introduction of detection theory is thoroughly discussed in the literature (e.g. Van Trees 2001, Kay 2009). In the following subsections, some of the principles of detection theory that are needed for discussing the RFI detectors are presented.

3.2.1 Hypothesis Testing

This detection approach determines whether a jammer signal exists or not. The decision is based on hypothesis testing which is divided into binary and multiple hypothesis tests. The binary hypothesis test includes two cases, namely H_0 and H_1, as null and alternative hypotheses which in this context represent the absence or presence of an RFI. In this research, only binary hypothesis testing is considered. The simplest method to discriminate between two hypotheses for a *N*-point sequence is written as

$$\begin{aligned} H_0 &: x[n] = e[n] \qquad n = 1,2,...,N \\ H_1 &: x[n] = i[n] + e[n] \qquad n = 1,2,...,N \end{aligned} \tag{3.1}$$

where $x[n]$ is the received signal, $e[n]$ represents the GNSS signal plus environment noise, and $i[n]$ is interference signal which must be detected:

$$e[n] = s[n] + \eta[n] \tag{3.2}$$

A decision on each hypothesis is achieved by forming a test statistic $\Gamma(\mathbf{x})$ on the received data samples $\mathbf{x} = \begin{bmatrix} x[1] & x[2] & ... & x[N] \end{bmatrix}^T$, and comparing $\Gamma(\mathbf{x})$ with a threshold γ. Signal jamming event is detected if $\Gamma(\mathbf{x})$ exceeds the threshold. In other words,

$$\begin{aligned} H_0 &: \Gamma(\mathbf{x}) < \gamma \\ H_1 &: \Gamma(\mathbf{x}) > \gamma \end{aligned} \tag{3.3}$$

Hence, the main problem in designing a detector is choosing a proper test statistic $\Gamma(\mathbf{x})$ and setting a decision threshold γ in order to achieve an optimal detection performance.

3.2.2 Receiver Operating Characteristics

The case wherein the H_1 hypothesis is wrongly detected while it is not actually present is called a false alarm. The Probability of false alarm (P_{FA}) can be expressed as (Kay 2009)

$$P_{FA} = P(H_1; H_0) = \Pr\{\Gamma(\mathbf{x}) > \gamma; H_0\} \tag{3.4}$$

Usually, P_{FA} is a small value in order to avoid the disastrous effects that may ensue (Kay 2009). To design an optimum detector, the next step is finding the maximum value for $P(H_1; H_1)$. This probability means the H1 hypothesis is detected while it is present and is called probability of detection. It is denoted by P_D as follows (Kay 2009):

$$P_D = P(H_1; H_1) = \Pr\{\Gamma(\mathbf{x}) > \gamma; H_1\} \tag{3.5}$$

The performance of a detector is quantified in terms of its receiver operating characteristics (ROC). ROC is a way to show the efficiency of a detector by plotting P_D versus P_{FA} at a certain jammer power to noise spectral density ratio (J/N_0). J/N_0 is defined as

$$\left(\left[J / N_0\right]\right)_{dB} = \left(\frac{\left[P_j\right]}{\left[N_0\right]}\right)_{dB} \tag{3.6}$$

where P_j is the total jammer power in watts received at the GNSS equipment and N_0 is a white noise process at the antenna output. This white noise process has a flat power spectral density of $N_0/2$ [W/Hz]. Therefore, J/N_0 is expressed in the log scale in unit of [dB-Hz].

Each point on the ROC curves corresponds to a pair of (P_{FA}, P_D) for a decision threshold γ. There is a trade-off between detection and false alarm probabilities. As γ increases, P_{FA} and P_D decrease and vice versa. A detector is optimum when for a given P_{FA}, P_D is maximum.

3.3 Effective Jammer Power Range

A jamming signal reduces the effective C/N_0 of a GNSS receiver by increasing the noise spectral density. Figure 3-1 shows effective C/N_0 at a GPS L1 C/A receiver's correlator output with respect to J/N_0 for the civilian jammers introduced in Section 2.6.1. The effective C/N_0 is calculated based on the equation provided by Betz (2001). Herein, J/N_0 is changed in a range of 40 dB-Hz to 100 dB-Hz which is equal to a jammer power in an approximate range of -163.8 dBW to -103.8 dBW. Moreover, the receiver front-end bandwidth of 10 MHz is chosen. Table 3-1 shows the simulation parameters for the jammers. As shown, all kinds of jammers have insignificant impact on the effective C/N_0 when J/N_0 is less than 60 dB-Hz. In contrast, for J/N_0 equal or more than 60 dB-Hz the adverse effect of jammer is extensive.

As shown in Figure 3-1, all jammers show similar behaviour. The higher the jammer power, the less the effective C/N_0. For the upcoming simulations, only Group II jammers are considered due to the similarity of their effects on the effective C/N_0. Increasing the jammer bandwidth beyond GNSS signal bandwidth reduces its adverse effect on receiver performance. It is due to the fact that the chirp signal spectrum does not completely coincide within GNSS signal bandwidth and consequently the whole jammer power does not pass through correlator filters (Jafarnia-Jahromi et al 2015).

Table 3-1 Jammer signal parameters (Bauernfeind et al, 2012)

Group	**Centre frequency**	**Bandwidth**	**Sweep time**
I	1.5747 GHz	0.92 KHz	-
II	1.5713 GHz	5 MHz	T_{sw1} = 12 μs
III	1.5732 GHz	5 MHz	T_{sw1} = 9 μs, T_{sw4},1 = 1.1 ms, T_{sw2} = 44 μs, T_{sw4},2 = 1.4 ms, T_{sw3} = 140-184 μs, T_{sw4},3 = 2.3 ms,

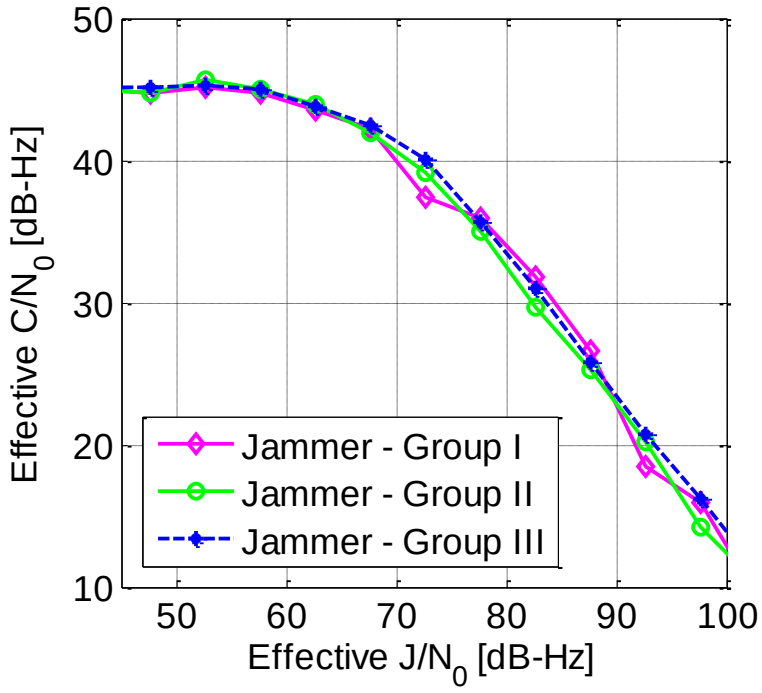

Figure 3-1 C/N_0 vs J/N_0 for different civil jammer groups

3.4 Detection Methods

According to Section 3.1.1 and 3.1.2, the main components of a statistical test are the null hypothesis (H_0), alternative hypothesis (H_1), test statistic ($\Gamma(\mathbf{x})$) and rejection region which is calculated by a threshold (γ). Statistical tests are solved by different detection approaches and based on the structure of interference signals. In this research, RFI detection methods can be generally divided into power content, PSD analysis techniques and normality techniques that are discussed in the sequel (Jafarnia-Jahromi et al 2015).

3.4.1 Power Content Analysis

These methods measure the received signal energy over a specified time period. The measured value is compared to a predefined threshold to decide whether an

interference signal is present or not. Based on Equation 3.1, the null hypothesis only includes noise samples and low energy GNSS signals. However, the signal energy level increases once interference signals are added. The basic idea behind energy based detection methods is that if the average energy of the received signal samples is larger than a predefined threshold, interference signals are present. Herein, the power-law detector (PLD) described by Lehtomäki (2005) is used. This method works based on accumulation of energy of the input samples. If the input signal is divided into several windows with length N, PLD is calculated by

$$f_{\nu} = \sum_{n=1}^{N} \left| x[n] \right|^{2\nu} \tag{3.7}$$

where ν is the power-law parameter and has a positive integer value (Lehtomäki 2005). $\nu = 1$ corresponds to the square-law energy detector which is commonly used in the literature. This is the optimal non-coherent detector for unknown Gaussian interference signal $x[n]$ buried in Gaussian noise and if $x[n]$ blocks are independent with Gaussian distribution (Atapattu et al 2014).

The detection threshold is defined based on an interference free window of received signals. The power of the first window is the variance of signal under H_0 (σ_0^2). The square-law energy detector can be normalized with respect to the block length N and σ_0^2 as

$$\Gamma(x_l) = \frac{\sum_{n=1}^{N} x[n]^2}{N \times \sigma_0^2} \tag{3.8}$$

where x_l is the l^{th} window of input signal $x[n]$. Herein, the detection threshold can be expressed as (Atapattu et al, 2014)

$$\gamma = \left(Q^{-1}\left(P_{fa}\right) + \sqrt{N}\right) \times \sqrt{N} \times \sigma_0^2 \tag{3.9}$$

where Q is the Gaussian Q-function, defined as

$$Q(b) = \frac{1}{\sqrt{2\pi}} \int_b^{\infty} e^{-\frac{u^2}{2}} du \tag{3.10}$$

Figure 3-2 shows an example of the square-law energy detector method. In this case, J/N_0 is equal to 65 dB-Hz, the jammer bandwidth is 5 MHZ, P_{FA} is 10^{-6} and the window length is equal to 1 ms. The interference is added to the authentic signal from 500 μs onwards.

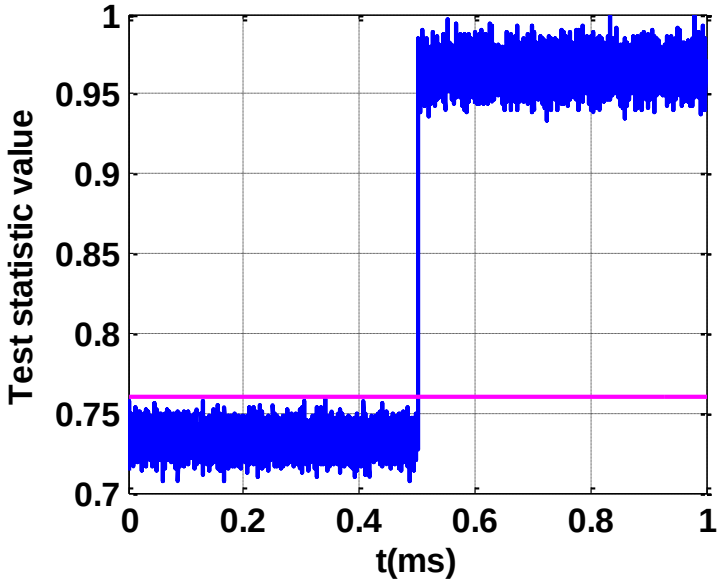

Figure 3-2 An example of square-law energy detector

The square-law energy detector ROC curves for different J/N_0 values are shown in Figure 3-3. The simulation settings are shown in Table 3-2. The jammer parameters are

available in the second row of Table 3-1. For J/N_0 equal or higher than 60 dB-Hz, the detection probability curves are very close to one and indistinguishable. The detection performance degrades for jammers as weak as 55 dB-Hz.

Table 3-2 Simulation settings

	Front-end bandwidth (MHz)	Window length (ms)	P_{FA}
ROC curves	10	1	-
P_D vs. Length	10	-	10^{-6}

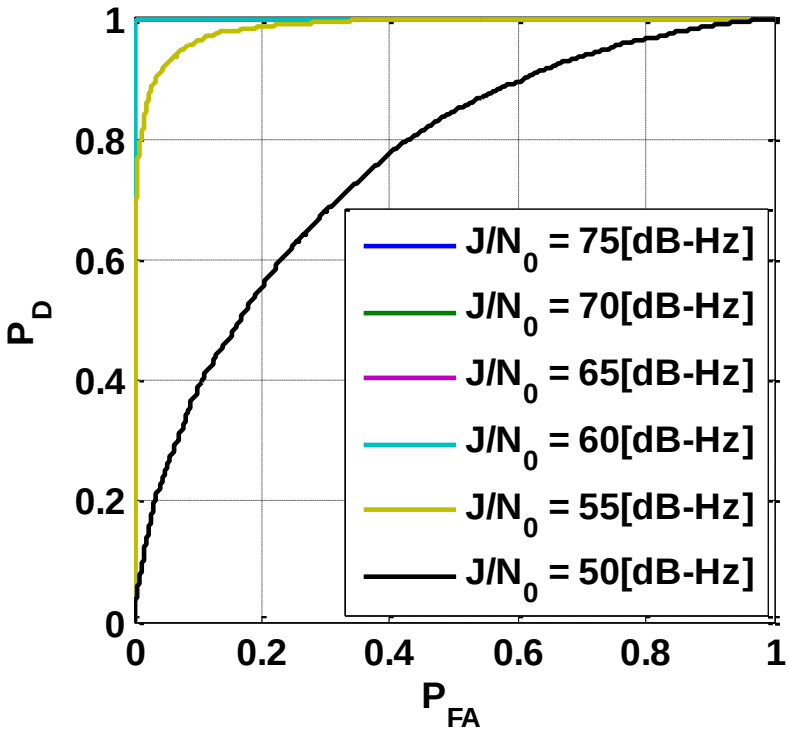

Figure 3-3 ROC for the square-law energy detector with different interference power levels

Figure 3-4 shows the detection probability of the power-law detector versus window length where, window length changes from 10 μs to 1 ms, and for different J/N_0 values using the settings of Table 3-2. The larger the window length, the better the detector

performance due to the additional information fed into the detector. As shown, larger window lengths may compensate for weaker jammer powers.

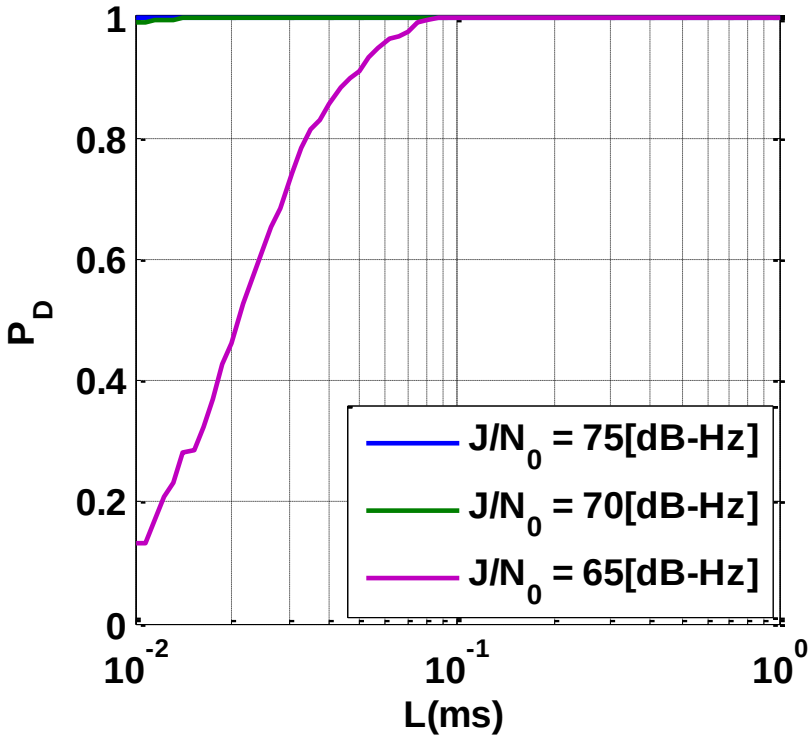

Figure 3-4 P_D vs window length for the square-law energy detector with different interference power levels

3.4.2 PSD Analysis

PSD techniques are based on the Fourier transform and are implemented by a FFT block. The test statistics can be defined as

$$\Gamma\left(k_{\max}\right) = \left|X\left(k_{\max}\right)\right|^2 \tag{3.11}$$

where $X\left(k\right)$ is equal to the k^{th} FFT frequency bin defined as

$$X\left(k\right) = \sum_{n=0}^{N-1} x\left[n\right] \exp\left(-j\frac{2\pi nk}{N}\right) \tag{3.12}$$

and $\left|X\left(k\right)\right|^2$ has its maximum value at $k_{\max}$. Then, this value is compared with a threshold γ. Detection occurs when $\left|X\left(k_{\max}\right)\right|^2 \geq \gamma$. This detector is optimum when the interference is sinusoidal (Gerdner 1988) and if the frequency in each window is fixed. This frequency value is equal to $\frac{2\pi k_{\max}}{N}$.

The above method is called periodogram and works properly for chirp signals when the jammer bandwidth is less than the front-and bandwidth.

3.4.2.1 Welch Analysis

Periodogram variants include Bartlett and Welch methods. In the Bartlett algorithm, the input signal is divided into M non-overlapping windows where each window has length P. The Welch algorithm is an extension of the Bartlett method by allowing overlapped windows and is chosen hereafter. The size of each window (P) is very small such that the frequency content can be assumed constant for each of them. For each window, the periodogram is calculated and the Welch power spectrum estimation is obtained through averaging the periodograms for the *M* consecutive windows. For the N-point sequence x[n], the method can be expressed as (Ahmed et al 2006)

$$\Gamma\left(k\right) = \frac{1}{N}\sum_{i=0}^{M-1}\left|\sum_{n=0}^{P-1} x_i\left(n\right)\exp\left(-j\frac{2\pi nk}{P}\right)\right|^2 \tag{3.13}$$

where k is the FFT index and

$$x_i\left(n\right) = x\left(i\times P + n\right)\ ,\ \ i = 0,1,...,M-1 \tag{3.14}$$

The threshold for this method can be calculated as (Ahmed et al, 2006)

$$\gamma = \frac{\sigma_0^2}{N} \mathrm{K}^{-1}\left(\left(1 - P_{fa}\right)^{\frac{2}{P-4}}, M \right) \tag{3.15}$$

where σ_0^2 is the variance of noise in a clean window and Φ is called incomplete gamma function which is defined by

$$\mathrm{K}\left(x, a\right) = \frac{1}{\Upsilon\left(a\right)} \int_0^x \exp\left(-t\right) \times t^{a-1} dt \tag{3.16}$$

which in $\Upsilon\left(a\right)$ is the value of gamma function in a.

The Welch ROC curves for different J/N_0 are shown in Figure 3-5. The simulation settings and jammer parameters are shown in Table 3-2 and the second row of Table 3-1. Herein, the FFT size (P) is 100 μs. In addition, M is equal to 20, which results in 1 ms data per each periodogram with a 50% overlap. As depicted, for J/N_0 values equal to or more than 65 dB-Hz, the detection probability is very close to 1. The detection performance degrades for jammers as weak as 60 dB-Hz.

Figure 3-6 shows the detection probability of the Welch detector with respect to window length for different J/N_0 values. In this case, the window length is chosen in the range of 10 μs to 1 ms. Moreover, the same as the ROC, the FFT size (P) is 100 μs and M is changed according to the size of window length. It is evident that for chirp-jammers with J/N_0 of equal or more than 65 dB-Hz, the detector has a good performance even with a small window length. In contrast, for weaker interference, the window length must be increased.

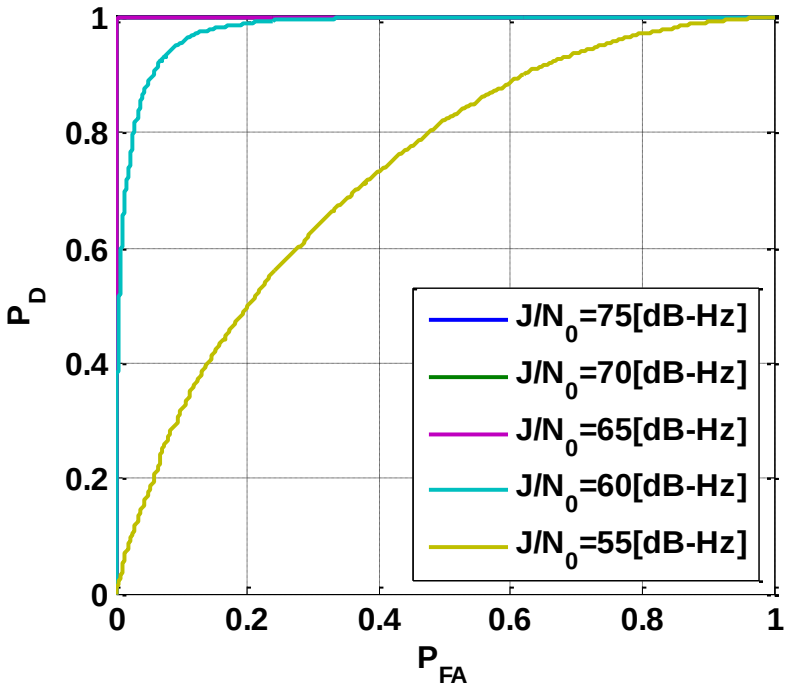

Figure 3-5 ROC for the Welch detector with different interference power levels

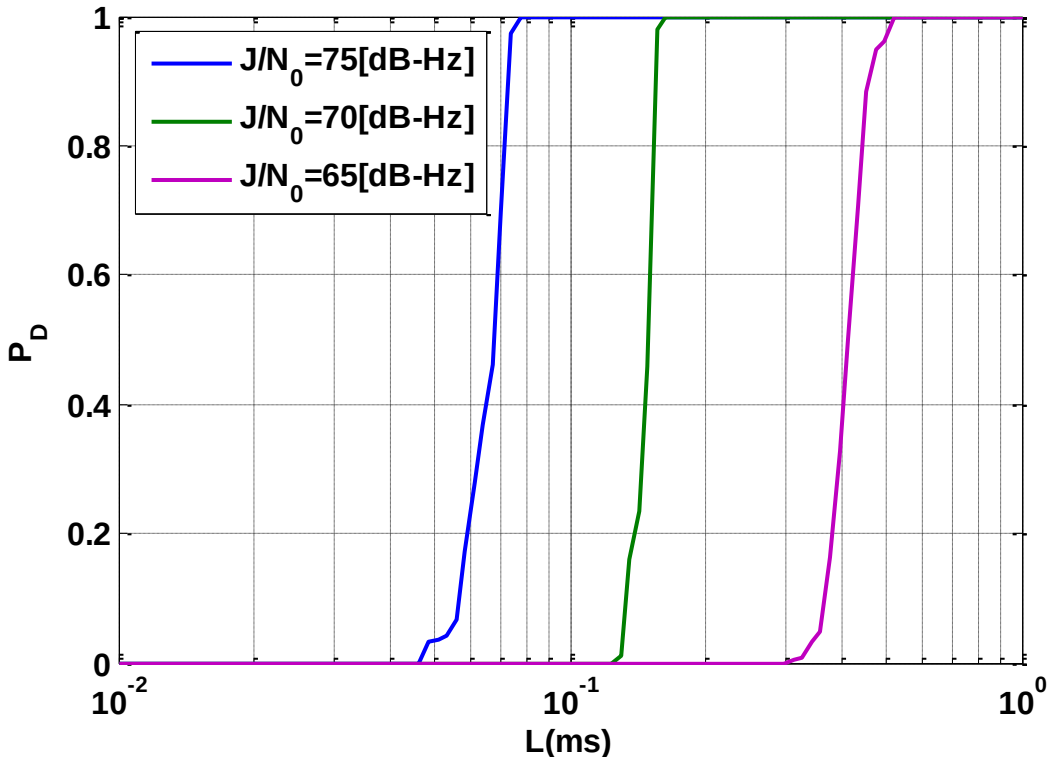

Figure 3-6 P_D vs window length for the Welch detector with different interference power levels

3.4.2.2 PSD Distribution Analysis

This technique, which also calls the Marti method, is able to detect interfering signals by recording the background noise and looking for significant changes. Here, a two-population t-test is used to detect interference in the frequency domain.

For detection of GNSS interference signals in the receiver, a non-parametric large sample t-test was introduced by Marti (2004) and evaluated by Balaei (2007).

The algorithm incorporates an assessment window consisting of p samples, which allows for assessment of the statistical properties of the random process. In the time period when the statistical properties of the process are gathered, it is assumed that no interference is present in the received signal. In addition, this method also incorporates an evaluation window of size k, which is shifted over the incoming data stream as shown in Figure 3-7.

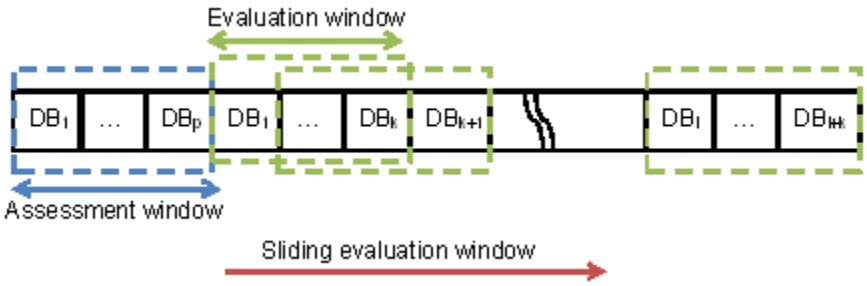

Figure 3-7 Assessment and evaluation window

In the absence of interference, the power spectral density in each frequency bin of the assessment window has the same mean over all of the data blocks of this window as that of the corresponding frequency bin of the evaluation window.

The t-test null hypothesis assumes that the two windows is normally distributed with the same sample mean and equal but unknown variances. However, the alternative hypothesis is that the means and variance are not equal. The only assumption is that

two populations are identically independent. The test static is given by

$$\Gamma(x_l) = \frac{\hat{\mu}_{assessment} - \hat{\mu}_{evaluation}}{\sqrt{\hat{\sigma}^2_{assessment} + \hat{\sigma}^2_{evaluation}}} \tag{3.17}$$

where $\hat{\mu}$ is the sample mean and $\hat{\sigma}$ represents the sample variance of each population. Moreover, x_l is the l^{th} frequency bin of the input signal $x[n]$. To detect interference by revealing fluctuations of the received signal power, the test is performed on the second moment energy estimator $\hat{U}$ given by

$$\hat{U} = E\left[X^2\right] = \frac{1}{N}\sum_{n=0}^{N-1} X_n^2 \tag{3.18}$$

where N is the number of samples of a window. It is shown by Marti (2004) that $\hat{U}$ converges to a normal distribution as N increases. The pairs of ($\mu_{H_0}, \sigma^2_{H_0}$) and ($\mu_{H_1}, \sigma^2_{H_1}$) are defined as mean and variance of the null and alternative hypothesis and are shown in Figure 3-8.

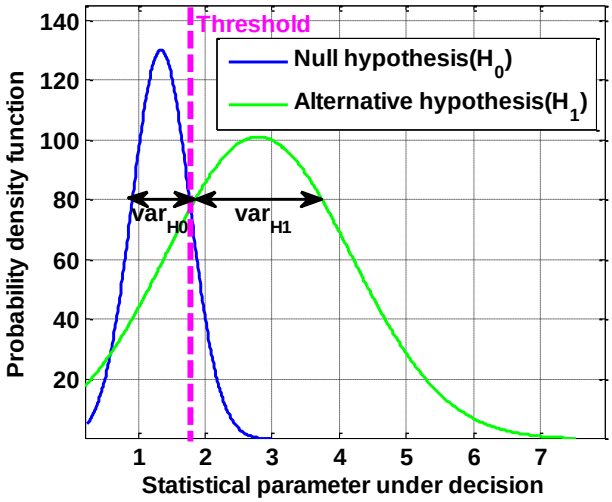

Figure 3-8 Difference between PDFs of assessment and evaluation windows

Defining the threshold for the Marti method is based on the definition of the p-value. The p-value, or attained significance level, is the smallest level of significance P_{fa} for which the observed data indicates that the null hypothesis should be rejected (Wackerly et al 2008). Herein, threshold is given by

$$p-value=\int_{Y}^{\infty} f_{H_0}(y)dy \tag{3.19}$$

where

$$f_{H_0} \sim N\left(\mu_{assessment}-\mu_{evaluation},\sqrt{\sigma^2_{assessment}+\sigma^2_{evaluation}}\right) \tag{3.20}$$

and the Y parameter is calculated by

$$Y=Q^{-1}(2P_{FA})\times\sigma_{assessment}\times\sqrt{2}+\mu_{assessment} \tag{3.21}$$

where Q is given by Equation 3.10.

The ROC curves in the Marti method are shown in Figure 3-9 using the jammer parameters and simulation settings of the second row of Table 3-1 and Table 3-2. The assessment and evaluation window length are 200 μs and 1 ms, respectively. In this case, the evaluation window consists of 10 PSD blocks of 100 μs length.

Figure 3-10 shows the detection probability of the Marti method for various window lengths and J/N_0 values. In this case, $P_{FA} = 10^{-4}$ is considered and the window length is chosen in the range of 10 μs to 1 ms. The other parameters are similar to those of the Figure 3-9 simulation. It is evident that for jammers with J/N_0 values of 70 dB-Hz or more, the detector has a good performance even with a small window length. In

contrast, for weaker interference, a longer window is required to achieve the same performance.

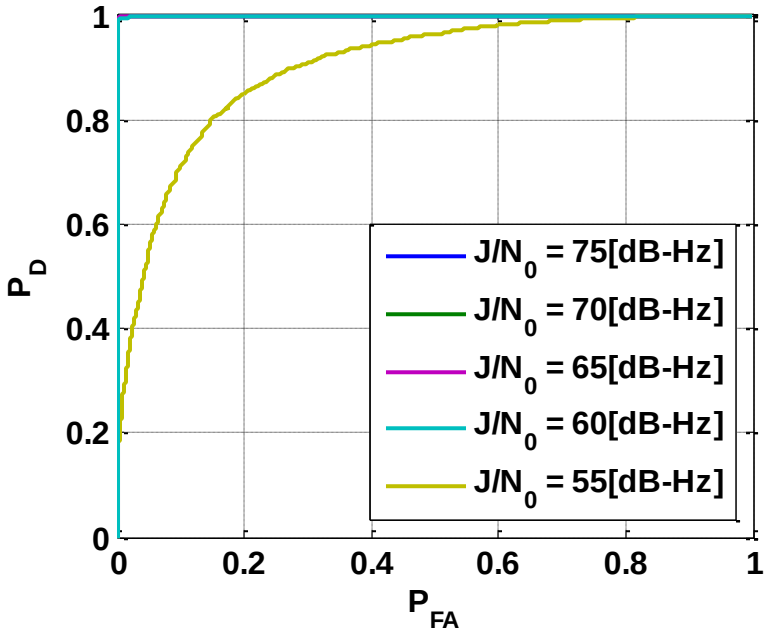

Figure 3-9 ROC for the Marti detector with different interference power levels

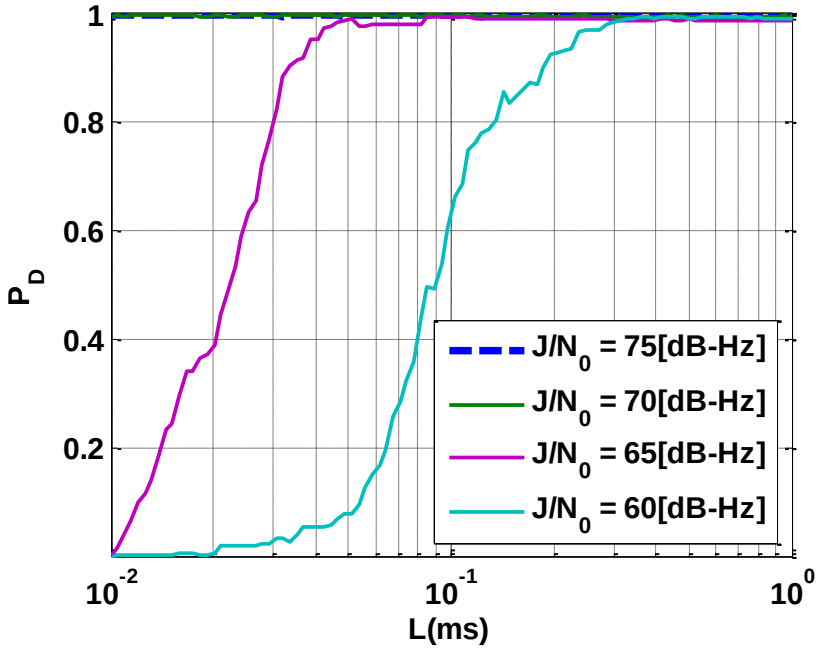

Figure 3-10 P_D vs window length for the Marti detector with different interference power levels

3.4.3 Normality Technique

Normality methods are statistical techniques that can be implemented in the time and/or frequency domain and are based on the fact that RFI free signals are zero mean Gaussian random variables. Therefore, the PDF (probability density function) associated with the RFI free signal is assumed beforehand. The amplitude PDFs of authentic signals as well as various civil jammer signals is shown in Figure 3-11. Obviously, the presence of RFI completely changes the amplitude distribution and this characteristic can be utilized for jammer detection.

Several normality tests have been reported in the literature (Tarongi et al 2010). In the following, several types of normality interference detection methods are presented.

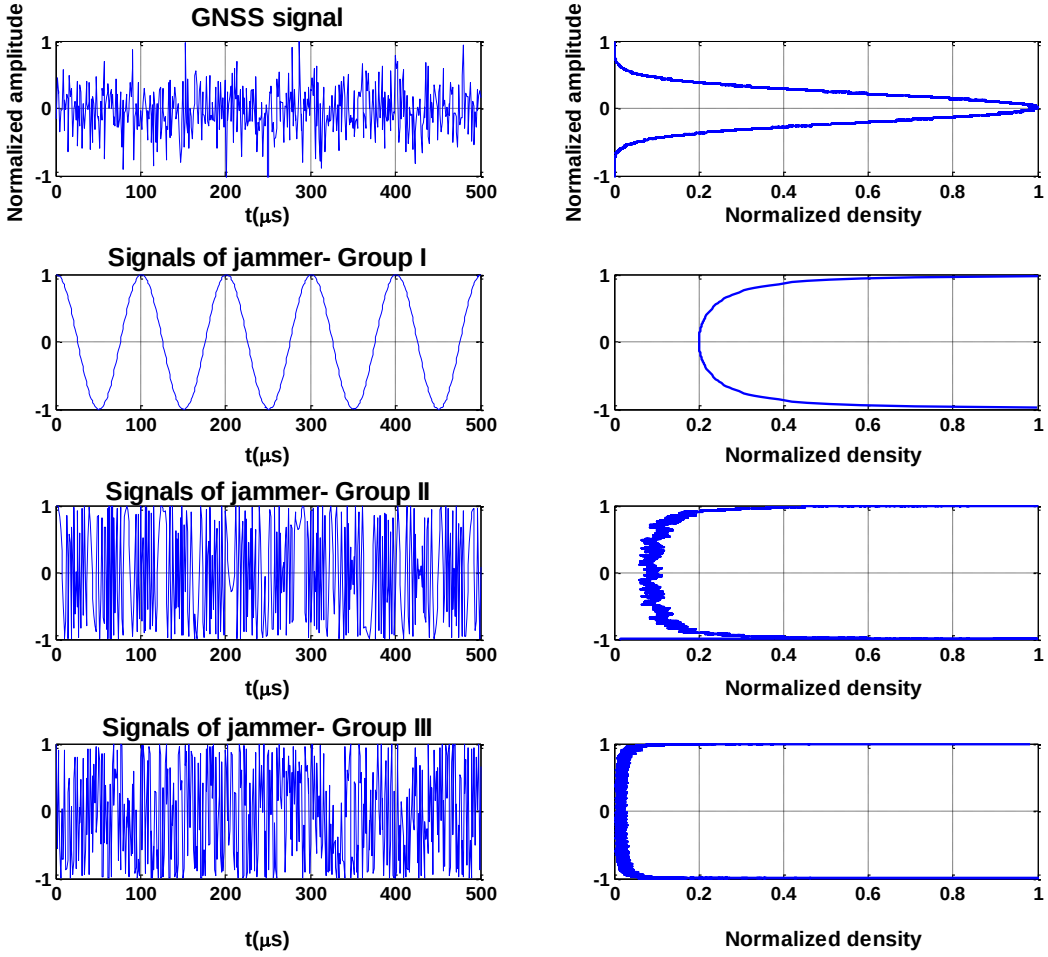

Figure 3-11 Example of GNSS and jammer signals and their PDFs. Time domain representations of the signals are on the left along with their corresponding PDFs on the right.

3.4.3.1 Kurtosis Method

The Kurtosis ($\hat{K}$) is a statistical parameter defined as the forth central moment normalized by the square of the second central moment (variance). This method is defined as follows for a zero mean random variable (De Roo et al, 2007):

$$\Gamma(x) = \hat{K} = \frac{\hat{\mu}_4}{\hat{\sigma}^4} = \frac{m_4}{m_2^2} = \frac{\frac{1}{N}\sum_{n=1}^{N}\left(x[n]-\mu\right)^4}{\left(\frac{1}{N}\sum_{n=1}^{N}\left(x[n]-\mu\right)^2\right)^2} \tag{3.22}$$

where N is the number of samples and μ represents the mean of x. Moreover, $\hat{K}$ is the kurtosis estimator and m_j is the j[th]-moment of the resulting signal.

As shown in Equation 3.22, the distribution of the Kurtosis method depends on the window length (N), which is illustrated in Figure 3-12. For shorter sample size N, the upper tail is longer than the lower tail. By increasing the window length, both side tails tend to 3.

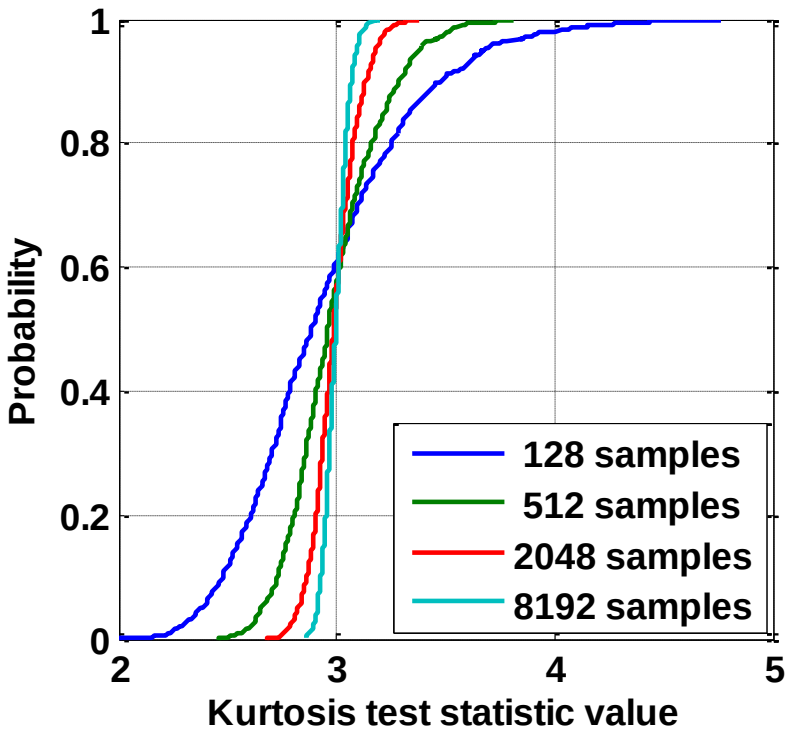

Figure 3-12 CDF of Kurtosis test statistic for the RFI free case

Assume that RFI is modeled as a sinusoidal wave with a duty cycle of DC and amplitude of A. The PDF of clean signal ($g(x)$) is given by

$$g(x) = \frac{1}{\sigma_0\sqrt{2\pi}} e^{\frac{-x^2}{2\sigma_0^2}} \tag{3.23}$$

where σ_0 is the standard deviation of the input signal $x[n]$. The PDF of The RFI ($f(x)$) can be represented by

$$f(x) = (1-DC)\delta(x) + \frac{DC}{\pi\sqrt{A^2 - x^2}} \tag{3.24}$$

where $x[n]$ is the input signal. These two signals are statistically independent. Thus, the probability distribution of the composite signal is given by the normalized version of the following equation:

$$r(x) = f(x) * g(x) \tag{3.25}$$

In order to calculate the Kurtosis, it is required to calculate the first four moments of the resulting signal. These moments can be calculated as follows:

$$\begin{aligned} m_1^{g+f} &= 0 \\ m_2^{g+f} &= \sigma_0^2 + \frac{(DC)A^2}{2} \\ m_3^{g+f} &= 0 \\ m_4^{g+f} &= 3\sigma_0^4 + 2(DC)A^2\sigma_0^2 + \frac{3(DC)A^4}{8} \end{aligned} \tag{3.26}$$

Hence, the Kurtosis for a Gaussian distribution in the absence of RFI is given by

$$K = \frac{m_4}{m_2^2} = \frac{3\sigma_0^4}{\left(\sigma_0^2\right)^2} = 3 \tag{3.27}$$

For a normally distributed signal, the Kurtosis is 3 and independent of σ_0. In the presence of RFI, the moment ratio becomes

$$K = \frac{m_4^{g+f}}{\left(m_2^{g+f}\right)^2} = \frac{3\sigma_0^4 + 2(DC)A^2\sigma_0^2 + \frac{3(DC)A^4}{8}}{\left(\sigma_0^2 + \frac{(DC)A^2}{2}\right)^2} = \frac{3P_s^2 + 4P_sP_j + \frac{3}{2(DC)}P_j^2}{\left(P_s + P_j\right)^2} \tag{3.28}$$

where P_s and P_j are noise and jammer power, respectively. Herein, P_s is equal to σ_0^2 and P_j is $\frac{(DC)A^2}{2}$.

In case the input signal is corrupted by RFI, the PDF may deviate from a Gaussian distribution. Hence, the Kurtosis value may deviate from 3.

According to Equation 3.28, in some cases, in spite of the presence of a RFI signal, the Kurtosis becomes 3. Therefore, the algorithm cannot detect the interfering signal. These cases are called blind-spots. Four conditions are possible for which the Kurtosis ratio becomes 3, including the following tow:

- $A \neq 0, (DC) = 0.5$, and $\sigma_0^2 \approx 0$. In this condition, a special case happens when the duty cycle is 50%. In this case, if the thermal noise is very small compared to the RFI signal, the RFI cannot be detected. This is the first case of blind-spot.

- $A \neq 0, (DC) \leq 0.5$, and $\frac{P_s}{P_j} = \frac{2\sigma_0^2}{(DC)A^2} = \frac{|6(DC)-3|}{4(DC)}$. This condition represents another blind-spot potential. If the relationship among duty cycle, RFI power and thermal power is as shown, this detection algorithm fails. The relationship between the thermal to RFI power ratio and duty cycle of the sine pulse under this condition is shown in Figure 3-13.

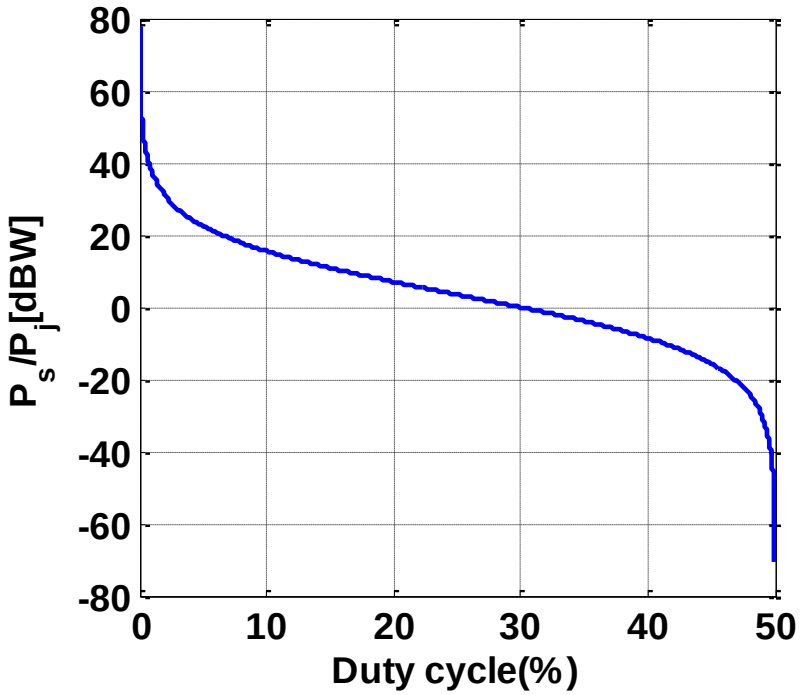

Figure 3-13 Power ratio vs duty cycle for blind spot

The Kurtosis threshold is defined by De Roo et al (2007) in a range of $\gamma = 3 \pm z \times \sigma_0$ for which the z value is determined by the desired P_{FA} for the blind spots of the algorithm. The z value is determined by

$$z = Q^{-1}(1 - 2 \times P_{FA}) \times \sqrt{2} \tag{3.29}$$

Moreover, the large sample variance in the absence of RFI is denoted by σ_0^2, which is equal to $24/N$ where N is the number of input samples (De Roo et al 2007).

The ROC curves of Kurtosis method is shown in Figure 3-9 using the settings of Table 3-1 and Table 3-2. In this case, the ROC curves for J/N_0 values of 70 dB-Hz or higher are indistinguishable.

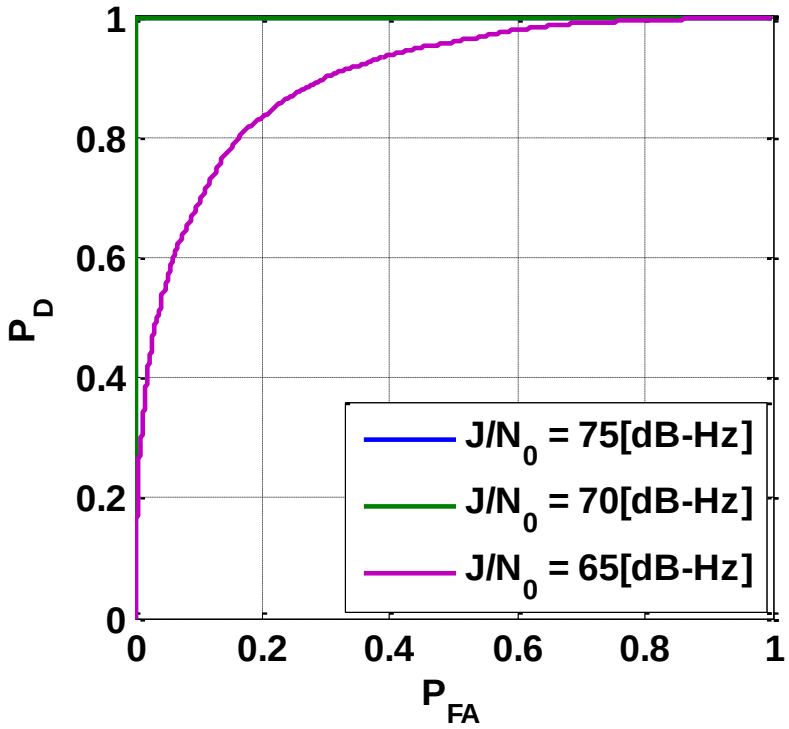

Figure 3-14 ROC for the Kurtosis detector with different interference power levels

Figure 3-15 shows the detection probability of the Kurtosis method for various window lengths and J/N_0 values. In this case, the parameters are shown in Table 3-2, and the window length is chosen in the range of 10 μs to 1 ms. Compared to the other methods presented, this algorithm has poorer performance even for jammers with J/N_0 values of 70 dB-Hz or higher when a small window length is utilized.

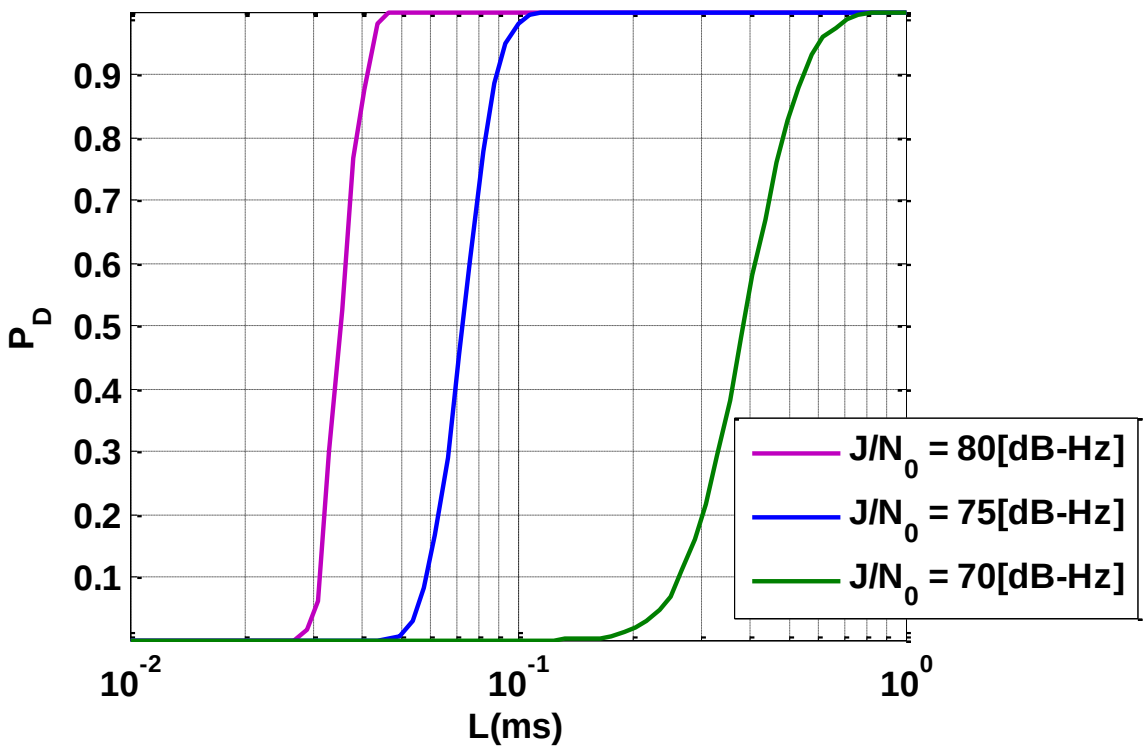

Figure 3-15 P_D vs window length for the Kurtosis detector with different interference power levels

3.4.3.2 Goodness of Fit (GoF) Method

The Goodness of fit method is proposed in order to find the discrepancy between the observed and expected values of a normality model. A lack of fit can indicate the presence of an alternative hypothesis. In the following, the most useful GoF techniques are presented.

Motella et al (2014) have proposed a test statistic of a Chi-square GoF method for detecting a jammer attack described as follows: At first, the PDF in the absence of interference $i[n]$ is evaluated. The values are then grouped into K non-overlapping regions that are represented by different bins (b_i). A vector $E = \{E_1, E_2, ..., E_k\}$ is defined where

$$E_i = N \Pr\left(x \in b_i\right) \tag{3.30}$$

E_i shows the number of samples expected in bin b_i in a null hypothesis. Then, a real input signal $x[n]$ is considered. Likewise, the input samples are divided into several bins in which x_l is the l^{th} bin of input signal $x[n]$. Accordingly, two histograms can be defined, namely the expected histogram E_i and observed histogram O_i, which show the PDFs of $e[n]$ and $x[n]$ stationary random processes. These processes represent the presence and absence of interference, respectively. The test statistic can be evaluated as

$$\Gamma\left(x_l\right) = T_\chi\left(x_l\right) = \sum_{i=1}^{k} \frac{\left(O_i - E_i\right)^2}{E_i} \tag{3.31}$$

Figure 3-16 shows the difference between the expected and observed histograms. A larger $T_\chi\left(x_l\right)$ value represents more histogram dissimilarity. In this figure, the expected and observed PDFs are related to clean and jammed data sets. For the simulation, the front-end bandwidth is 10 MHz and the window length is 1 ms. A type II jammer (Table 3-1) is used in this experiment.

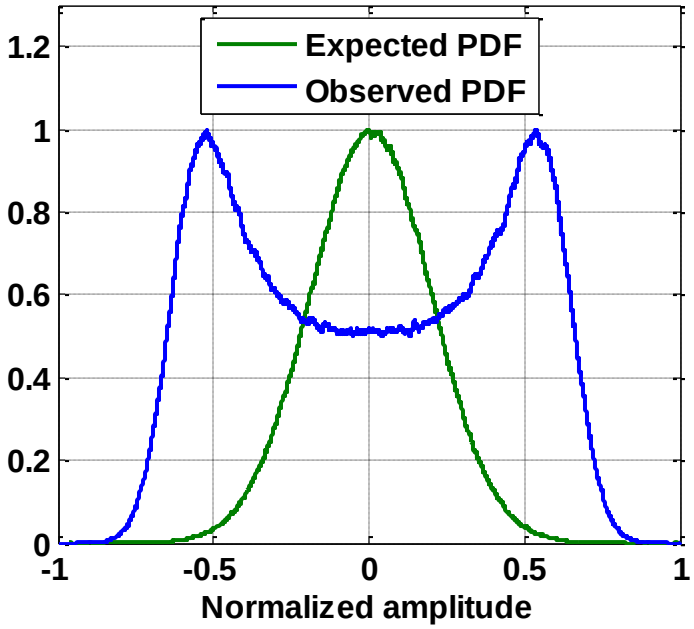

Figure 3-16 Expected and observed PDFs

In case the histograms match together, the value of the test statistic is $T_\chi(x_l)=0$. The next step is to find a proper threshold for decision making in the binary hypothesis test. A constant threshold γ is defined as

$$\gamma = Pr\left\{T_\chi(x) > T_{\chi,\alpha}\right\} \tag{3.32}$$

where $T_{\chi,\alpha}$ is known as the critical value. The test statistic approaches a Chi-square distribution with k-3 degrees of freedom for a large number of input samples where K is the number of bins in both histograms (Bauernfeind et al 2014).

The ROC curves associated with GoF method are shown in Figure 3-17. The simulation parameters are provided in Table 3-1 and Table 3-2. As depicted, for J/N_0 values of 65 dB-Hz or higher, the detection probability is very close to 1. The detection performance degrades for jammers lower than 60 dB-Hz.

Figure 3-18 shows the detection probability of the GoF method for various window lengths and J/N_0 values. In this case, the parameters are shown in Table 3-2 and the window length is chosen in the range of 10 μs to 1 ms. As shown, larger window lengths may compensate for weaker jammer powers in terms of detection performance.

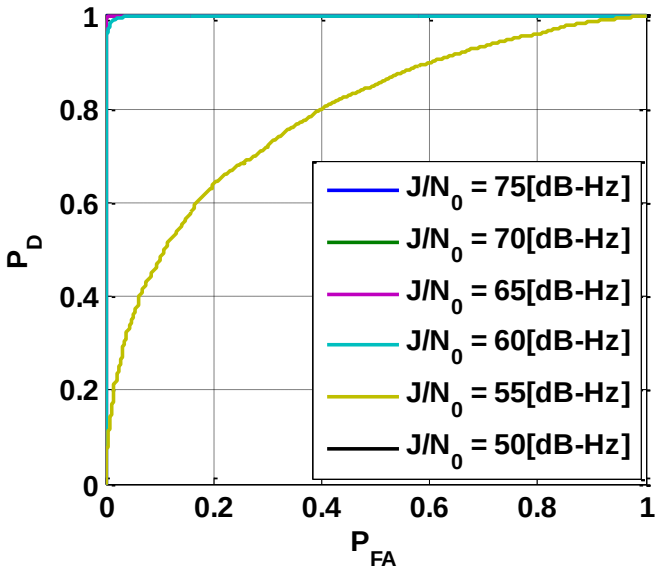

Figure 3-17 ROC for the GoF detector with different interference power levels

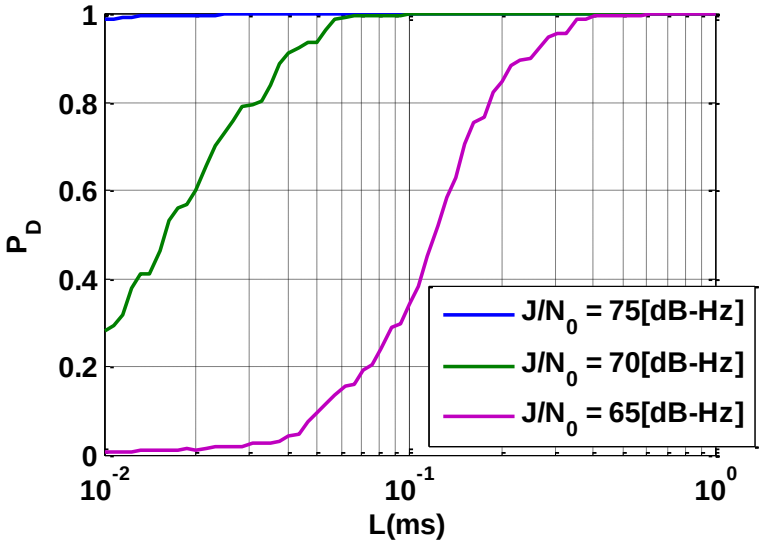

Figure 3-18 P_D vs window length for the GoF detector with different interference power levels

The GoF method identifies the dissimilarities between the expected and observed histograms. In the case of GNSS signals under RFI attack, it can be assumed that in the absence of interference the signal has a Gaussian distribution. In contrast, the presence of RFI causes the PDF to deviate from it.

One of the drawbacks of the GoF method is its requirement for initial information. In other words, a clean window must be fed into the GoF in order to evaluate the expected histogram. Herein, a variant to GoF is proposed in which the initial information is not required. Hence, this methods is called as blind-GoF.

In this method, different windows are tested independently and are evaluated with respect to their corresponding Gaussian distribution. In this way, the mean and variance of each window is calculated and a normal distribution with the same mean and variance as the expected window is assumed. In case there is no RFI, the observation window's PDF is also Gaussian and is matched with the expectation of 1. Hence, the test statistic (Equation 3.31) is almost zero. In contrast, when RFI is present, the test statistics become larger depending on the interference power.

The ROC curves associated with the proposed method are shown in Figure 3-19, using the simulation parameters of Table 3-1 and Table 3-2. This algorithm exhibits poor performance even for jammers with J/N_0 of 65 dB-Hz or lower. Moreover, the performance degrades rapidly for J/N_0 values below 70 dB-Hz. The detection probability of this method for various window lengths and J/N_0 values is shown in Figure 3-20 using the parameters of Table 3-2, and window length is chosen in the range of 10 μs to 1 ms.

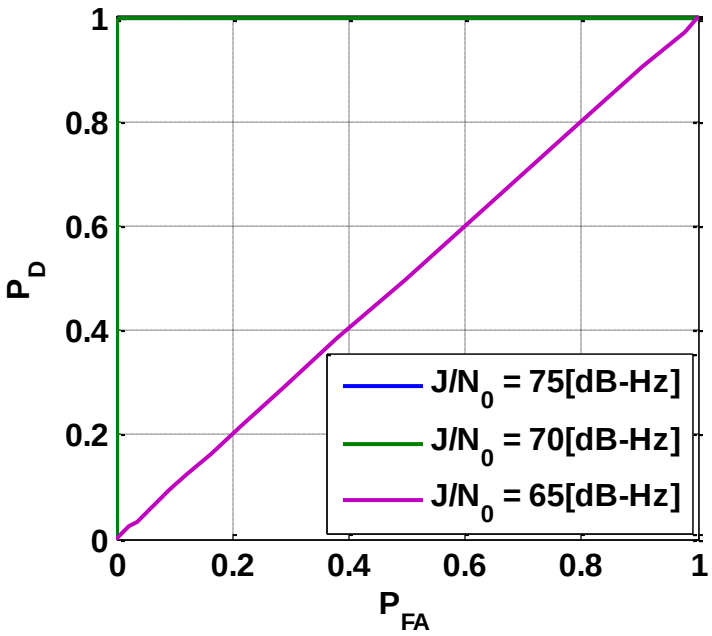

Figure 3-19 ROC for the blind-GoF detector with different interference power levels

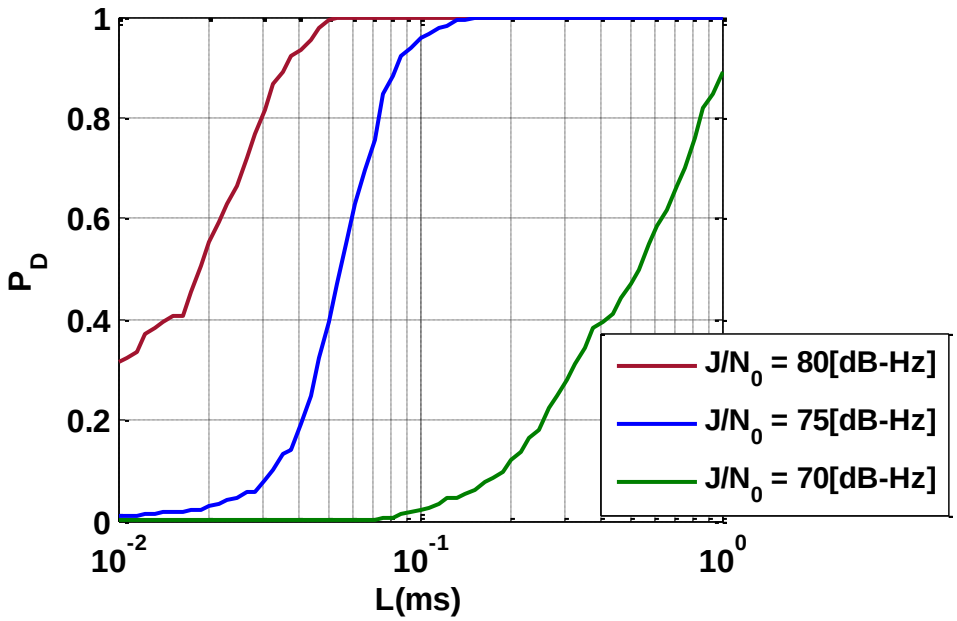

Figure 3-20 P_D vs window length for the blind-GoF detector with different interference power levels

3.5 Performance Comparison

This section compares the performance of the aforementioned detectors. Figure 3-21shows the simulation results of ROC curves for different methods.

The GoF method is GOF_1 and the modified GoF method (i.e. the proposed method) is GoF_2. The PDS distribution method is Marti method.

It is evident that the GoF_2 and Kurtosis methods have the poorest performance, though the latter has better performance than the former.

According to the previous section, for strong jammers (J/N_0 of 75 dB-Hz or higher) all methods have good performance with detection probability very close to 1. Moreover, for a moderate jammer power (i.e. J/N_0 = 65 dB-Hz) all methods except the blind-GoF and Kurtosis methods have very similar performance. As jammer power decreases more (i.e. J/N_0 = 55 dB-Hz), the PLD method shows the best ROC performance. The Welch, Marti and standard GoF methods are next best ones.

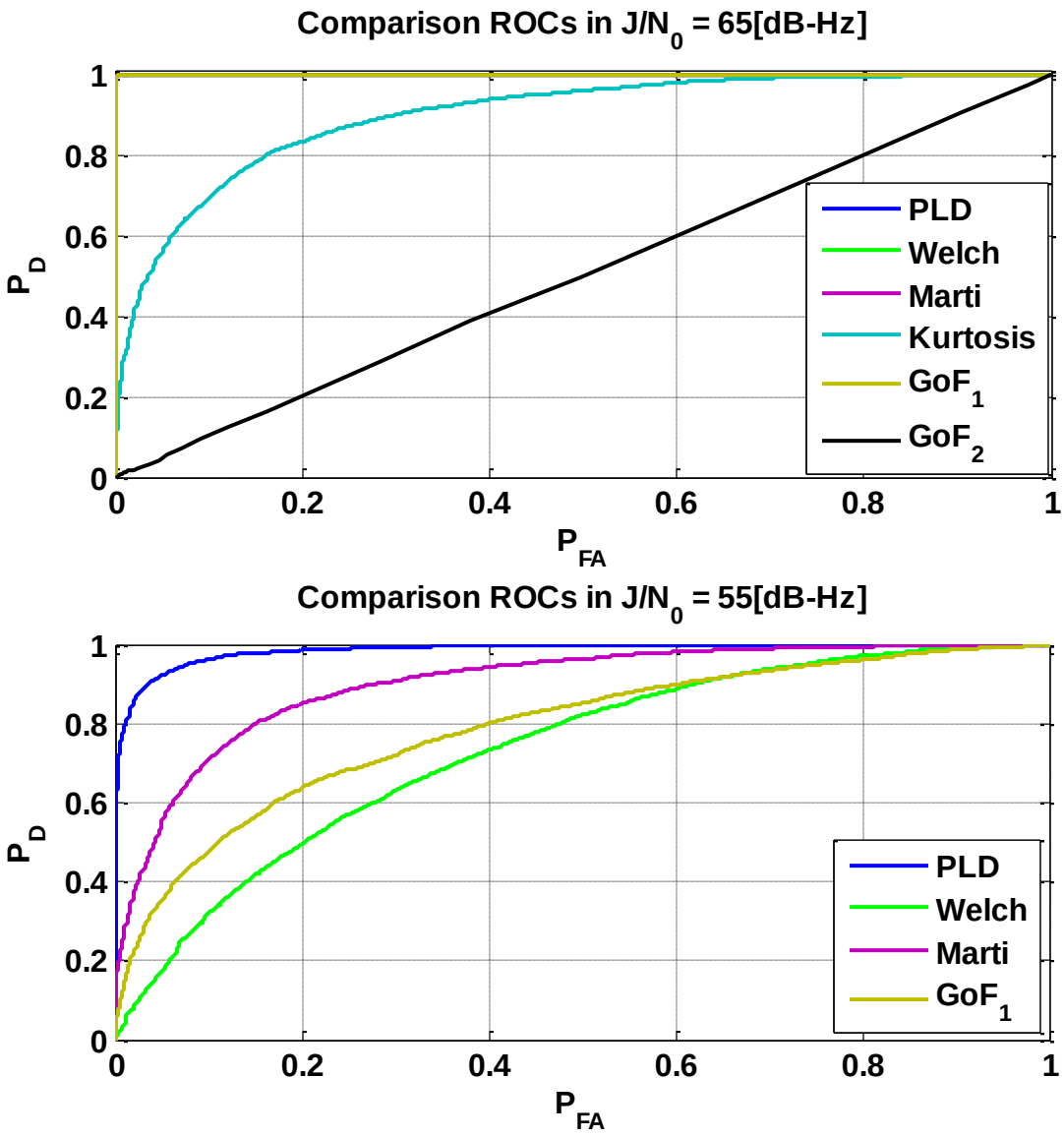

Figure 3-21 ROC curves for various detectors

Figure 3-22 shows the detection probability with respect to window length for various detection methods. Again, GoF method exhibits the poorest performance. In addition, PLD, Welch and Marti methods requires shorter window size for the same detection probability and thereby they are more efficient for high frequency rate chirp jammers.

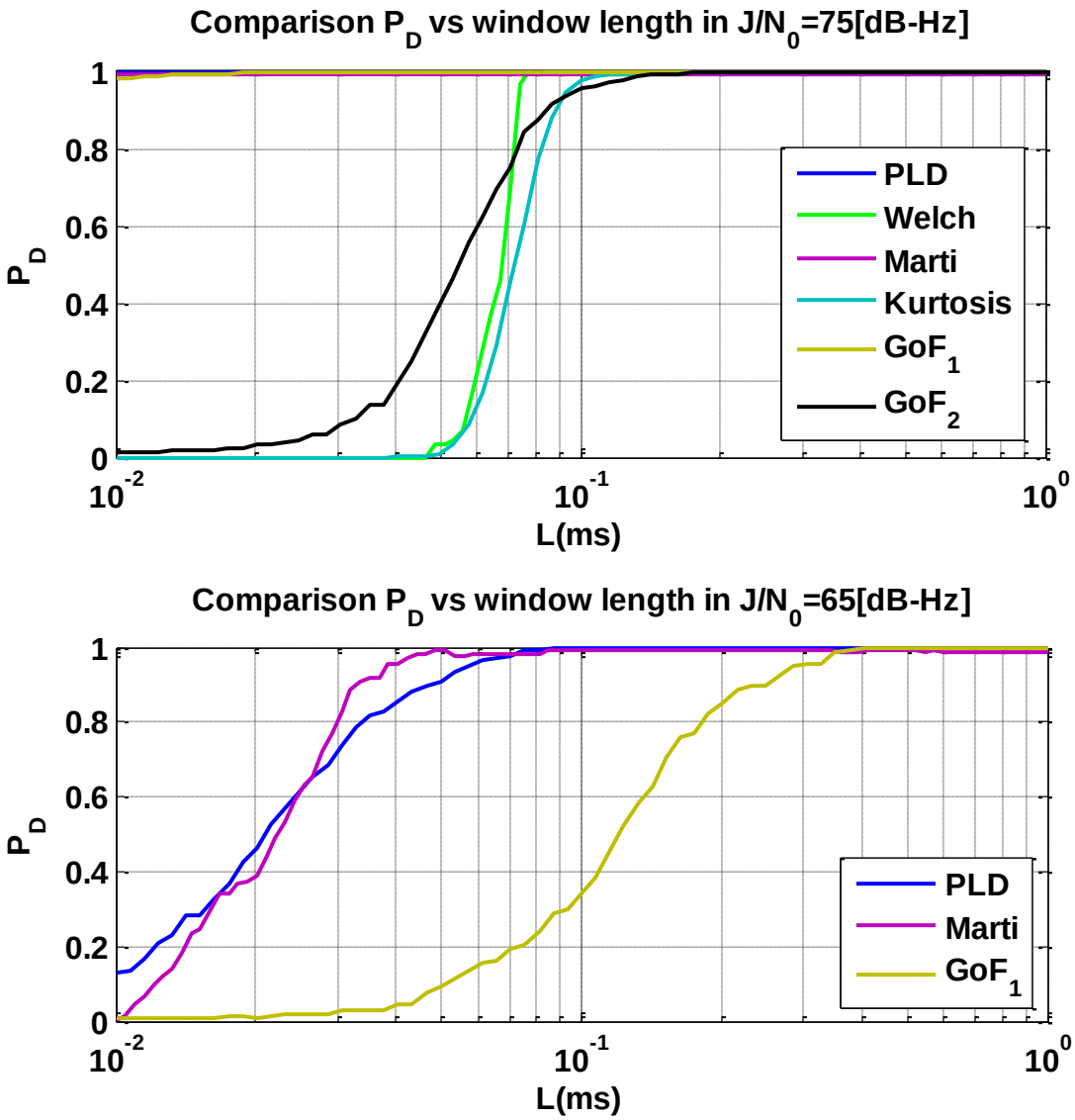

Figure 3-22 Detection probability with respect to window length for various detectors

The detection probability with respect to J/N_0 is shown in Figure 3-23. This curve complies with the two above figures and confirms that the PLD, Welch, Marti, and standard GoF methods, which require clean window information, have more or less the same performance and are better than the others.

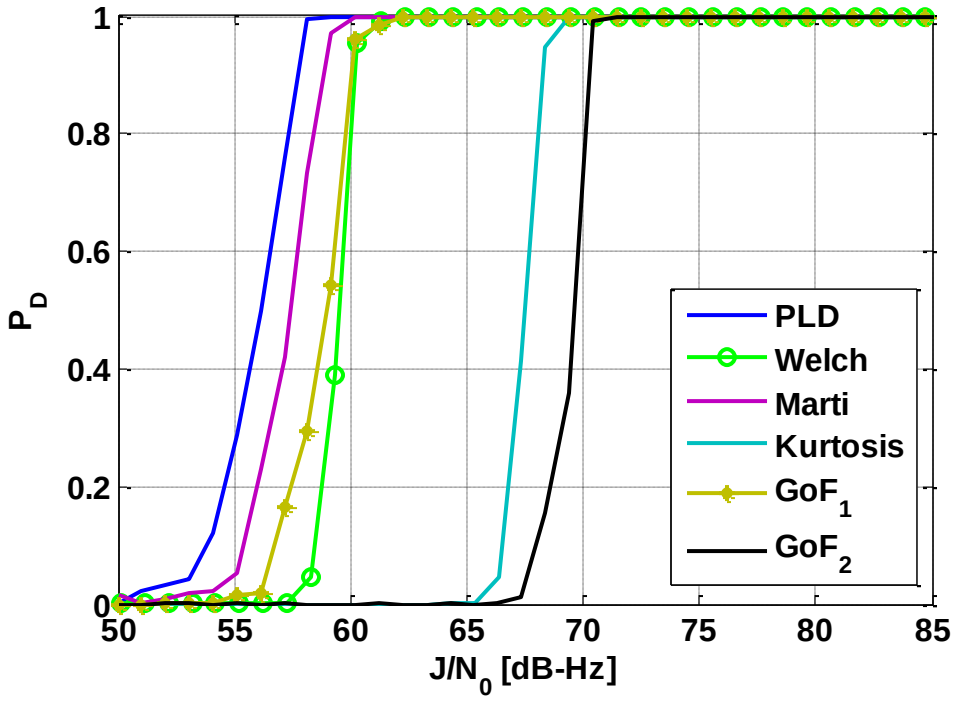

Figure 3-23. Detection probability with respect to J/N_0 for different detectors

3.6 Computational Complexity

One of the metrics used for the performance analysis of different methods is the computational burden. Table 3-3 quantifies the complexity of various detection methods. The complexity can be defined based on the number of addition, multiplication and/or other operators. The cost column indicates the complexity order (O). The O notation characterizes a function (e.g. complexity) according to its growth rate with a simpler function. In other words, it shows the function behaviour as the variable (i.e. N) tends to infinity. According to this table, the simplest method is the PLD and the most complicated detector is Marti's. The complexity of the blind-GoF is almost similar to the standard one.

Table 3-3 Complexity of different detection methods

Method	Computation	Cost			
		+	*	Other	
PLD	$\Gamma(x_l)=\frac{\sum_{n=1}^{N}x[n]^2}{N\times\sigma_0^2}$	N	N	-	O(N)
Welch	$X(k)=\sum_{n=0}^{N-1}x_i(n)\exp\left(-j\frac{2\pi nk}{N}\right)$	NlogN	NlogN	-	O(NlogN)
	$PSD_{X(k)}=\left(X(k)\right)^2$	-	N	-	O(N)
	$mean\left(PSD_{X(k)}\right)$	N	-	-	O(N)
Marti	$s(n)=x(n)\times h(n)$	-	N	-	O(N)
	$S(k)=fft(\mathrm{s(n)})$	NlogN	NlogN	-	O(NlogN)
	$PSD_{S(k)}=\left(S(k)\right)^2$	-	N	-	O(N)
	$mean\left(PSD_{S(k)}\right)$	N	-	-	O(N)
	$\mathrm{var}\left(PSD_{S(k)}\right)$	2N	N	-	O(N)
	$\Gamma(x_l)=\frac{c_1-mean\left(PSD_{S(k)}\right)}{\sqrt{c_2+\mathrm{var}\left(PSD_{S(k)}\right)}}$	2N	-	N	O(N)
Kurtosis	$\Gamma(x_l)=\frac{\frac{1}{N}\sum_{n=1}^{N}\left(x[n]-\mu\right)^4}{\left(\frac{1}{N}\sum_{n=1}^{N}\left(x[n]-\mu\right)^2\right)^2}$	3N	2N	-	O(N)
GoF_1	$\Gamma(x_l)=\sum_{i=1}^{k}\frac{(O_i-E_i)^2}{E_i}$	N+2k	2k	N	O(N)
GoF_2	$mean\left(x[n]\right)$	k	-	-	-
	$\mathrm{var}\left(x[n]\right)$	2k	k	-	-
	Normal distribution	k	k	-	-
	$\Gamma(x_l)=\sum_{i=1}^{k}\frac{(O_i-E_i)^2}{E_i}$	N+2k	2k	N	O(N)

Figure 3-24 provides a relative comparison of the computational complexity of previously discussed detection techniques. The execution time of each method is extracted using the MATLAB “profile” function on a windows server 2012 PC with a 2.6 GHz CPU and 32 GB of RAM. The computational requirement of each algorithm for the same data set is reported. It is observed that the lowest execution time corresponds to PLD. The execution time of Marti, standard GoF and Welch are higher and within the same order. The highest execution times correspond to non-trained PDF analysis methods i.e. the blind-GoF and Kurtosis techniques.

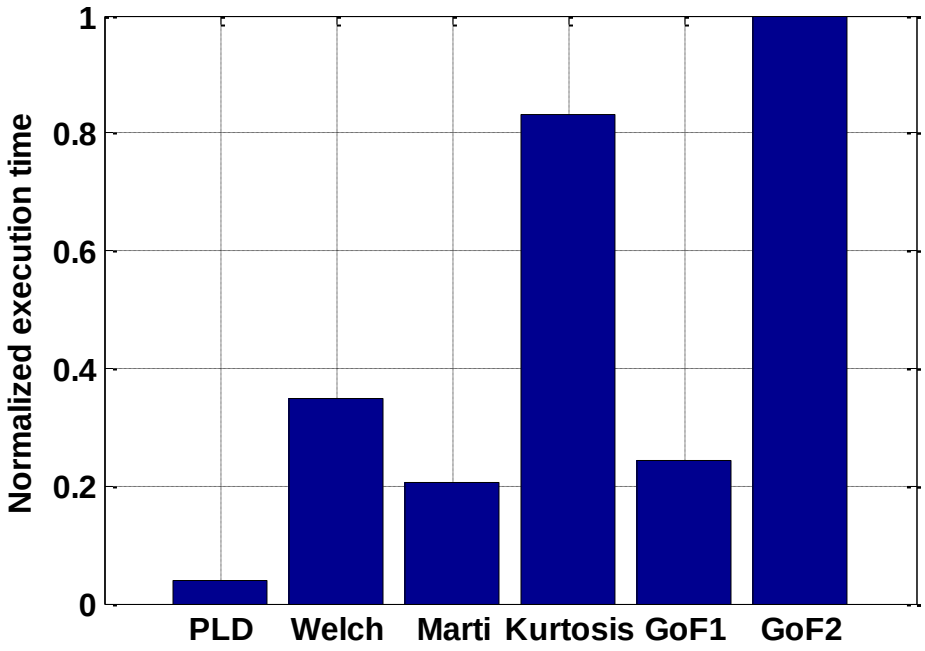

Figure 3-24 Detectors complexity comparison

3.7 Summary

This section provides a concise comparison among various jammer detectors in this chapter. Table 3-4 shows the performance comparison for different methods. Herein, P_{FA} is 10^{-6} for all detectors. The speed of detection column shows the required data size

for each detector to achieve detection probability very close to 1 (i.e. equal or better than 0.999). The J/N_0 for speed of detection calculation is equal to 75 dB-Hz and its value is obtained from Figure 3-22. The minimum jammer power column is the minimum power for the detectors for which their probability of detection becomes very close to 1 (i.e. equal or better than 0.999). In this case, a window length of 1 ms is chosen. The minimum jammer power is obtained from Figure 3-23.

Table 3-4 Performance comparison

Detector	**Speed of detection**	**Minimum jammer power**	**Complexity**	**Need a clean window**
PLD	High	Low	Low	Yes
Welch	Low	Low	Moderate	Yes
Marti	High	Low	Moderate	Yes
Kurtosis	Low	High	High	No
GoF_1	High	Low	Moderate	Yes
GoF_2	Low	High	High	No

Table 3-4 shows that the PLD has the lowest complexity and simplest structure. The PLD has also the fastest detection performance. In terms of interference detection sensitivity, the PLD, Welch, Marti and standard GoF methods show more or less the same performance with minimum jammer power of about -144 dBW. Despite the good performance of these methods, their main disadvantage is that they require a clean window for threshold determination before the detection operation. In contrast, Kurtosis

and the blind-GoF methods do not need any a priori information, but at the cost of lower performance.

In comparison with the blind-GoF method, Kurtosis has better performance. However, according to Bauza (2012), the Kurtosis method needs a complementary algorithm to cover all conditions of interference due to its blind-spots.

Chapter Four: GNSS Interference Characterization Based on Pre-Correlation Methods

4.1 Introduction

Jammer characterization is a key step in the interference suppression unit. To date, most civil-jammer signals have non-stationary behavior due to one or more time-varying parameters in the signal structure. However, most of the traditional signal analysis methods are based on the assumption of stationarity. Such methods can only provide analyses in term of the statistical average in time or frequency domain but do not consider the signal features in both time and frequency domains simultaneously. Thus, they are not appropriate for characterizing the jammer signals. The joint time-frequency representation (TFR) is an effective approach to address these issues. Methods based on TFR map a one-dimensional signal into a two-dimensional function of time and frequency. The time-frequency plane gives an indication of which spectral components are present at a specific time epoch. Hence, both constant and time varying frequency components can be revealed (Cohen 1995, Qian et al 1996, Flandrin 1999, Grochenig 2000, Boashash 2002 and Papandreou-Suppappola 2003). To date, various TFR methods have been proposed. The early methods include linear time-frequency representation and bilinear time-frequency distribution (Hlawatsch et al 1992, Hess-Nielsen et al 1996 and Mallat 2009). Linear TFR methods and bilinear TFR analysis need one or more primary assumptions about jammer parameters. In order to alleviate the assumptions in the characterization methods and to have a better resolution in various types of jammer structures, researchers have extended these methods to adaptive time-frequency representation. These decomposition-based methods can be

categorized into parametric and non-parametric analysis. Adaptive parametric time-frequency representation methods work based on atomic decomposition (Grochenig 2000). Atomic decomposition can present arbitrary signals using some optimal functions adaptively chosen from a library of functions. The performance of atomic decomposition methods depends on the diversity of atoms in the dictionary employed. To match complex signal structures, various dictionaries including Gabor, wavelet, chirplets, FM^{m}lets, as well as dopplerlets have been developed (Chen et al 1998, Bultan 1999, Yin et al 2002, Zou et al 2001, Zou et al 2004). As this thesis deals with chirp jammers, the chirplets are the main research focus and will be described in Section 4.4.2. In order to increase the estimation accuracy of the instantaneous frequency, adaptive non-parametric time-frequency methods have been developed (Huang et al 1998 and Huang et al 2008). Moreover, the time invariant autoregressive moving average (ARMA) models have been extended to time-frequency analysis to handle non-stationary signals. The disadvantages of these methods are their high computational complexity and low time-frequency resolution (Jachan et al 2007). In order to decrease the complexity of ARMA methods, the jammer characterization and mitigation sections are combined together and will be presented in Chapter 5.

This chapter first provides an overview on linear TFR including three major methods, namely the short time Fourier transform (STFT), the Wavelet transform (WT) and the S-transform. Subsequently, an overview of bilinear TFR methods including the Wigner-Ville distribution (WVD) and Cohen distribution (CD) will be discussed. Then, two different adaptive TFR methods, namely the Hilbert-Huang transform (HHT) and the matching pursuit (MP) will be presented. Finally, the computational complexity, benefits

and drawbacks of these methods will be inter-compared. The presented techniques are applied to various civil-jammer groups, which were comprehensively described in Section 2.6. In this chapter, the jammer signals in GPS L1 band are considered. However, these methods can be applied to other satellite frequency bands as well.

4.2 Linear Time-Frequency Representation

Linear TFRs are based on the superposition principle. These methods state that if $x(t)$ is a linear combination of several signal components, then the TFR of $x(t)$ is also a linear combination of the TFRs of each signal components:

$$x(t) = c_1 x_1(t) + c_2 x_2(t) \Rightarrow T_x(t,f) = c_1 T_{x_1}(t,f) + c_2 T_{x_2}(t,f) \qquad (4.1)$$

As mentioned in Section 2.6, one of the properties of civil jammer signals is their linearity. Hence, these methods are appropriate for characterizing this kind of interference signals. In general, for a received signal $x(t)$, the linear TFR is given by

$$LTF_x(t,f) = \int_{-\infty}^{\infty} x(\tau)\phi_{t,f}^*(\tau)d\tau = \langle x, \phi_{t,f} \rangle \qquad (4.2)$$

where $\phi_{t,f}$ represents the basis functions (also called TF atoms) and $*$ is the complex conjugate.

According to De Bruijn (1967), the TFR follows the Heisenberg uncertainty principle, which states that the time and the frequency contents of a signal cannot be simultaneously obtained through an arbitrary precision. Due to the trade-off between time localization and frequency resolution, the drawback of linear TFR methods is the

resolution in time and frequency domains which cannot reach their highest levels simultaneously.

4.2.1 Short Time Fourier Transform

This method, by considering the time-varying feature of the input signal, adds a short-time window to the fast Fourier transform equation. Thus, STFT is also known as windowed-Fourier transform. One of the assumptions of STFT is that the signal in each short-window is stationary, which means its properties (e.g. frequency content) remain constant during each window.

For any input signal $x(n)$, suppose $w(m-n)$ is a window function centered at time m (where m is a time variable). Sliding the short-window through the time axis and applying the Fourier transform to each window results in STFT. The discrete-time representation of STFT can be expressed as (Gu et al 2000)

$$STFT_x(m,\omega_k) = \sum_{n=-\infty}^{+\infty} x(n)w(m-n)e^{-j\omega_k n}, k \in \{0,1,...,N-1\} \qquad (4.3)$$

where $\omega_k = \frac{2\pi f_k}{N}$ is the k th angular frequency which is evenly distributed between zero and sampling frequency, N is the number of frequency bins and the basis function is equal to $w(m-n)e^{-j\omega_k n}$. According to Equation 4.3, STFT estimator performance is dependent on window size due to its limited combined time-frequency resolution. Once the window function and its length are chosen, the time-frequency resolution of STFT remains constant. In fact, there is a trade-off between the time and frequency resolution of STFT. A larger window size results in a better frequency resolution but a poorer time

resolution. In contrast, a shorter window length leads to a finer time resolution but a coarser frequency resolution. For instance, a piecewise-constant frequency signal with dwell time equal to 90 μs and frequency sampling of 20 MHz is simulated to show the effect of choosing the window length in the STFT method. Figure 4-1 shows the result of STFT jammer characterization with different window lengths, i.e. 4 μs and 40 μs. A Hanning window with 50% overlap is assumed. The frequency resolution is defined as the error between the actual and estimated frequency for a given time. The time resolution is the time difference between the actual and estimated frequency jump at each point. Obviously, the shorter window (4 μs) has a better time resolution as it can respond to frequency changes on time at the expense of lower frequency resolution (inaccurate frequency estimation). In contrast, the longer window size (40 μs) estimates the instantaneous frequency very precisely at the expense of lower time resolution (at the frequency changes).

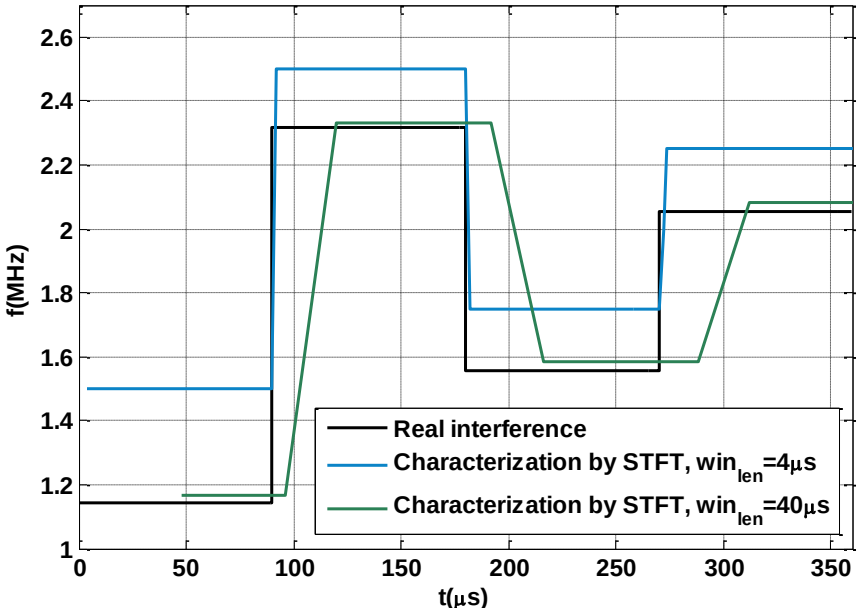

Figure 4-1 Time-frequency representation of CW-type interference signal and its estimation by STFT

Obviously, as the finest time location and the best frequency resolution cannot be reached at the same time, STFT lacks adaptability. Hence, it is only suitable to analyze quasi-stationary signals that are stationary at the scale of the analysis window, but is not appropriate to analyze highly transient jamming signals such as impulses and chirps.

4.2.2 Wavelet Transform

One of the appropriate TFR techniques for civilian jammer characterization is the Wavelet transform. In comparison to the STFT transform that uses a constant window length, the Wavelet transform uses a varying window length. The WT basically uses a "wide" time windows for low frequency analysis and "narrow" time windows for high frequency analysis to provide a good balance between time and frequency resolution (Jiang et al 2011).

The Discrete Wavelet transform (DWT) for a received signal $x(n)$ is defined as (Daubechies 1992)

$$WT_x(n,a) = \frac{1}{\sqrt{a}} \sum_{n=0}^{N-1} x(n) \Psi\left(\frac{n-b}{a}\right) \qquad (4.4)$$

where n is a discrete time variable, b is time-like translation variable and $a > 0$ is a dimensionless frequency scale variable. Moreover, Ψ represents the analyzing Wavelet function at position b and with scale factor a (which is referred to as the dilation). Herein, the scale factor $\frac{1}{\sqrt{a}}$ is a real normalization parameter.

The first step to characterize the received signal using WT is to choose an appropriate analysing Wavelet function. Several types of Wavelet functions have been proposed (Meyer 1993). In this research, a Meyer Wavelet is chosen as the analyzing Wavelet function as it is a proper choice for chirp-type signals (Meyer 1993). It is defined as

$$\Psi(\zeta)=\begin{cases}\dfrac{1}{\sqrt{2\pi}}\sin\left(\dfrac{\pi}{2}\nu\left(\dfrac{3|\zeta|}{2\pi}-1\right)\right)e^{i\zeta/2}, & \dfrac{2\pi}{3}<|\zeta|<\dfrac{4\pi}{3}\\ \dfrac{1}{\sqrt{2\pi}}\cos\left(\dfrac{\pi}{2}\nu\left(\dfrac{3|\zeta|}{2\pi}-1\right)\right)e^{i\zeta/2}, & \dfrac{4\pi}{3}<|\zeta|<\dfrac{8\pi}{3}\\ 0, & \textit{otherwise}\end{cases} \tag{4.5}$$

where ν is an auxiliary function and can be defined by (Meyer 1993)

$$\nu(t)=\begin{cases}t^4\left(35-84t+70t^2-20t^3\right), & 0<t<1\\ 0, & \textit{otherwise}\end{cases} \tag{4.6}$$

Figure 4-2 shows an example of a Meyer Wavelet in time and frequency domains. It illustrates the transfer functions of each branch of the non-uniform filters bank obtained by a dyadic scaling operation of the Meyer Wavelet function. Choosing a large scale factor causes an increase in time domain resolution and a decrease in frequency domain resolution and vice versa. Moreover, as shown, each Meyer Wavelet is in fact a uniform bandpass filter with a decreased bandwidth as their central frequency decreases. Herein, the sampling frequency and the number of samples are 16 MHz and 1024 respectively.

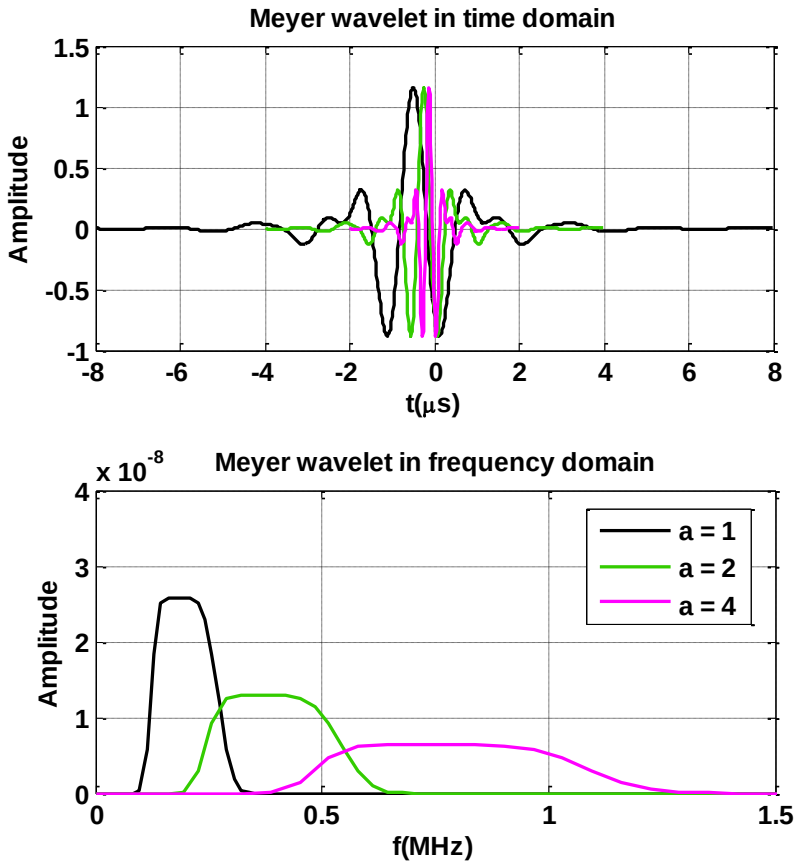

Figure 4-2 Example of Meyer Wavelets in time and frequency domains

As shown in Equation 4.4, Wavelet coefficients are functions of the scale factors and the positions. These coefficients are calculated for different values of scales and positions.

The variable time localization and frequency resolution nature of the Wavelet transform, i.e. adaptive windowing capability, makes it a suitable candidate for stationary signal analysis. For higher frequency components, the Wavelet transform has a better time localization and a lower frequency resolution. In contrast, for lower frequency components, the frequency resolution is higher at the cost of lower time localization resolution. The Wavelet transform is essentially a time-scale analysis method and thus is effective in analyzing self-similar signals. An example of this concept is shown in

Figure 4-3 where a dyadic DWT time-scale plane is illustrated. Herein, the scale changes by factors of two and the samples widen by factor of two for each successive scale. Each component is investigated based on the resolution matched to its scale. As a result, a narrow window in the time domain is able to localize the time-varying nature of the signal more precisely with respect to a wider window. Various types of Wavelet bases have been proposed. However, the question of how to choose a suitable one among them to match the signal structure remains an open issue.

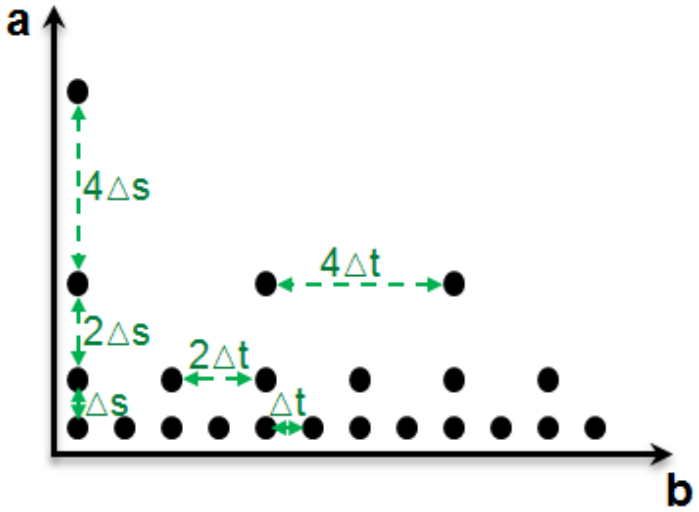

Figure 4-3 Dyadic DWT time-scale plane

4.2.3 S-Transform

The S-transform is a time-frequency analysis method that combines the properties of both STFT and WT. it provides a frequency dependent resolution while maintaining a direct relationship with the Fourier spectrum. Since this method is an extension of the STFT technique, it follows Equation 4.3. This equation, in continuous form, is given by

$$STFT_x(\tau,f) = \int_{-\infty}^{+\infty} x(t)w(t-\tau)e^{-j2\pi ft}dt \qquad (4.7)$$

As mentioned in Section 4.2.1, according to the uncertainty principle, the time-bandwidth product cannot be arbitrarily small. A Gaussian window is used in the S-transform and is defined as

$$w(t) = \frac{1}{\delta\sqrt{2\pi}} e^{-\frac{t^2}{2\delta^2}} \tag{4.8}$$

According to the nature of a Gaussian window, the standard deviation, δ, is the scale factor to change the width of Gaussian window. In order to have a better self-adaptability to different frequency components, δ is defined by $\delta(f) = \frac{1}{|f|}$ which is a frequency-related function. Hence, the new function can be written as

$$w(t,f) = \frac{|f|}{\sqrt{2\pi}} e^{-\frac{t^2 f^2}{2}} \tag{4.9}$$

The expression of S-transform can be written as (Stockwell 2007)

$$\begin{aligned} st(\tau,f) &= \int_{-\infty}^{+\infty} x(t) w(t-\tau,f) e^{-j2\pi ft} = \\ &= \int_{-\infty}^{+\infty} x(t) \left\{ \frac{|f|}{\sqrt{2\pi}} e^{-\frac{f^2(\tau-t)^2}{2}} e^{-j2\pi ft} \right\} dt \end{aligned} \tag{4.10}$$

The advantage of this method over STFT is that δ (which is the window length) is a function of f rather than a constant number in case of STFT. In contrast to WT, the S-transform basis function is divided into two parts as shown within the brackets of Equation 4.10. The first one is a slowly varying envelope (the Gaussian window) which localizes the time and the second component is the oscillatory exponential kernel which selects the frequency being localized. The difference with the Wavelet kernel is the time

localizing Gaussian component that is translated while keeping the oscillatory exponential kernel stationary. Herein, the oscillatory exponential kernel does not shift or scale with frequency. Hence, it retains the absolute phase information of the signal along with its amplitude spectrum which is not provided by WT.

The discrete S-transform of received signal $x(n)$ is defined as (Stockwell et al 1996)

$$s[l,m]=\sum_{n=0}^{N-1}x(n)\frac{|m|}{M\sqrt{2\pi}}e^{-\frac{1}{2}\left(\frac{m(l-n)}{M}\right)^2}e^{-j2\pi\frac{nm}{M}} \tag{4.11}$$

where l is the time index ($l=0,1,...,N-1$) and N is the number of samples, $m=-\frac{M}{2},...,\frac{M}{2}-1$ and $M=\frac{f_s}{f_0}$. Herein, f_s is the sampling frequency and f_0 is the frequency step.

4.2.4 Simulation Results

In order to characterize different chirp jammers, a series of chirps with different sweep times are now defined and simulated. For the rest of this section, the following chirp jammers are used as the input of TFR methods. The sweep time of the chirps are T_{sw1} = 2.5 μs, T_{sw2} = 5 μs, T_{sw3} = 12 μs, T_{sw4} = 41 μs, T_{sw5} = 144 μs, T_{sw6} = 500 μs. A lower sweep time shows a frequency spike which is an abrupt frequency variation within a window. However, the high sweep time shows slow time-varying frequency trends. The other jammer properties includes a bandwidth of 5 MHz, a J/N_0 of 150 dB-Hz (i.e. JNR = 80 dB) and a sampling frequency of 20 MHz.

Figure 4-4 shows the result of a chirp-type jammer characterization for the linear TFR methods compared to the actual time-frequency behavior of the input signal. For the

STFT method, a Hanning window with a 50% time overlap was applied to the input samples and a window size equal to 10 μs was chosen. It is observed that the performance of STFT is poor for the first three chirp sweeps due to their short periods. In this case, two or more chirp periods reside in each STFT window. Hence, STFT is unable to determine the time-frequency relationship of the jammers since the selected window contains a wide range of frequencies. This figure shows that STFT is able to characterize the signal more precisely for the following chirps with longer periods.

Herein, a Meyer-based DWT with 32 scales was implemented. In comparison to STFT, the performance of DWT for the first chirp with lower sweep time is better. The results indicate that the performance of DWT for characterizing small sweep times is more accurate than that of the STFT method.

The S-transform method was implemented with a δ value of 100. Figure 4-4 shows that the accuracy and resolution of this method is better than the STFT and WT methods for different sweep times. However, none of these methods can estimate the start time of lower sweep time (T_{sw1} = 2.5 μs) properly.

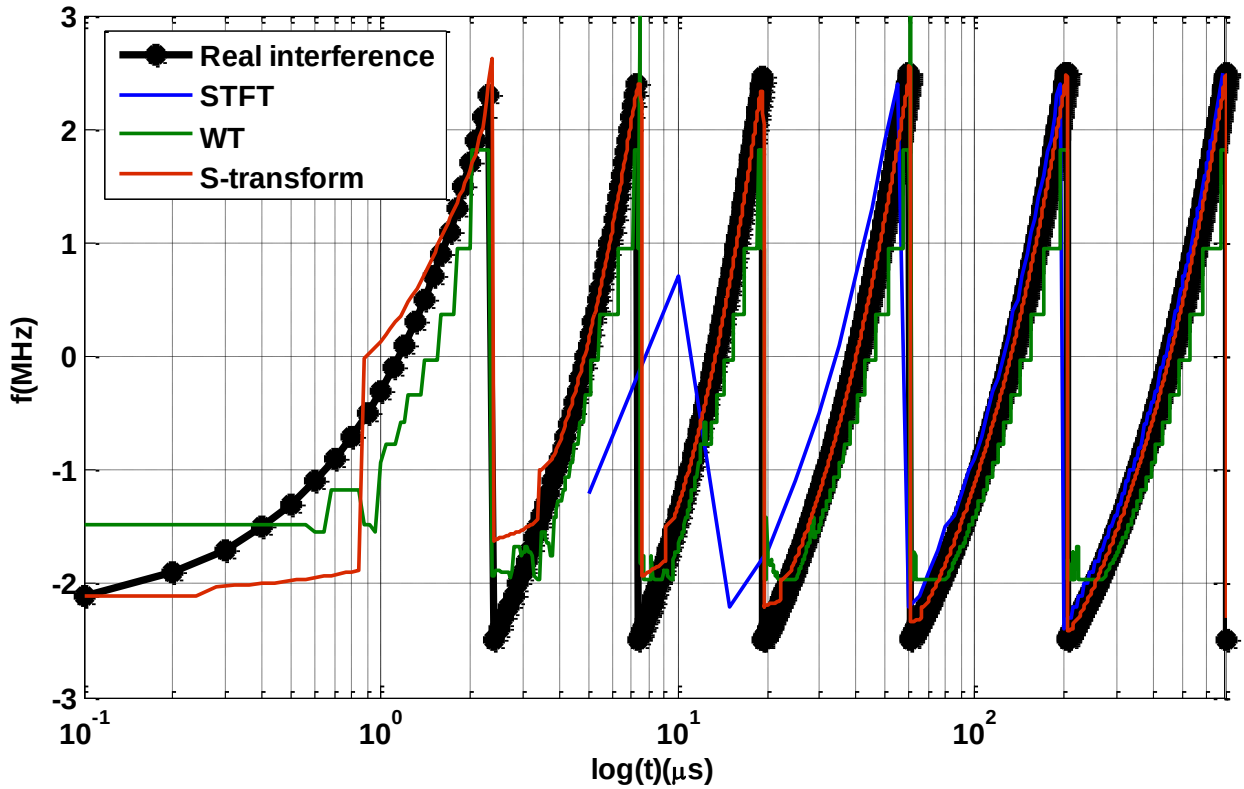

Figure 4-4 Time-frequency representation of chirp-type interference signal and its characterization using linear TFR methods

4.3 Bi-Linear Time-Frequency Representation

Bilinear TFR represents the signal energy distribution in the joint time-frequency domain. The Wigner-Ville distribution is the basis of almost all the bilinear time-frequency distributions (Cohen 1989). It has the highest time-frequency resolution. However, for multi-component signals, it suffers from the inevitable cross-term interference, thus it is not suitable for many practical applications. In order to maintain a higher resolution and to suppress the cross-term interference in the Wigner-Ville distribution, improved versions such as the Cohen class distribution method have been proposed (Cohen 1989, Rioul et al 1992). A mathematical description of bilinear TFRs for the received signal $x(t)$ is given by (Cohen 1995)

$$BTF(t,\omega,\phi)=\frac{1}{4\pi^2}\int_{-\infty}^{+\infty}\int_{-\infty}^{+\infty}\int_{-\infty}^{+\infty}x\left(u+\frac{\tau}{2}\right)x^*\left(u-\frac{\tau}{2}\right)\phi(\theta,\tau)e^{-j(\theta t+\tau\omega-\theta u)}dud\tau d\theta \quad (4.12)$$

where $\phi(\theta,\tau)$ is a two-dimensional kernel function which determines the specific representation in bilinear TFR. The Wigner distribution and Choi-Williams distribution are some of the commonly used methods for obtaining time frequency distributions (TFDs) (Cohen 1995).

4.3.1 Wigner-Ville Transform

For a given signal $x(n)$, the discrete Wigner-Ville distribution is defined by (Qiu 1993)

$$WVD_x(I,\omega)=2\sum_{n=-N/2+1}^{N/2-1}x(I+n)x^*(I-n)w(n)w(-n)e^{-2\omega n} \quad (4.13)$$

where I is the time variable, ω is the angular frequency variable, N is the number of samples and $w(n)$ is a symmetrical real window (such as Hamming) with length $2N-1$. In Equation (4.13), the signal appears twice and thereby this method is referred to as the bilinear distribution. As the WVD is not linear, the WVD of a sum of multiple signal components is not equal to the sum of the WVDs of these signal components. For instance, the WVD of signal $x(t)=x_1(n)+x_2(n)$ is

$$WVD_x(I,\omega)=WVD_{x_1}(I,\omega)+WVD_{x_2}(I,\omega)+2\mathrm{Re}\left[WVD_{x_1x_2}(I,\omega)\right] \quad (4.14)$$

where

$$WVD_x(l,\omega) = 2\sum_{n=-N+1}^{N-1} x_1(l+n)x_2^*(l-n)w(n)w(-n)e^{-2\omega n} \qquad (4.15)$$

In Equation (4.14) the first two terms are auto-terms and the third one is known as the cross-term. The cross-term results from the interference between time and frequency due to nonlinear quadratic transform. This term is real and its time-frequency characteristics reside between the auto-terms. Each pair of auto-terms result in one cross-term. Hence, for a signal with k components, there are $k(k-1)/2$ cross-terms. For multi-component signals in real applications, cross-terms produce a pseudo distribution and may overlap with the auto-terms on the time-frequency plane. In this case, the interference is even more complicated leading to blurred time-frequency features and making it more difficult to interpret the physical meaning of the WVD.

4.3.2 Cohen Distribution

To suppress the cross-terms of the WVD method, various techniques have been proposed so far [e.g., see Lerga et al (2009), Flandrin et al (1990) and Stankovic et al (2000)]. In general, these methods can be categorized into non-parameterized and parameterized TFR. These methods are a trade-off between cross-terms suppression and TFR concentration. The time-frequency methods, which use extra signal dependent parameters, are referred to as parameterized time-frequency analysis and will be considered in Section 4.4.2. The non-parameterized time-frequency analysis use the signal-independent parameter, i.e., window length (used to calculate instantaneous autocorrelation in WVD). Cohen class distributions are categorized into non-parametrized techniques and were introduced to filter cross terms of the WVD using a

kernel function (Rioul et al 1992). An effective kernel for the TFR should be able to diminish the effects of the interfering cross terms while inducing the desirable properties which can sustain the validity of the time-frequency distribution. Each kernel corresponds to a specific distribution such as Bessel, Born-Jordan, Choi-Williams, Page, Rihaczek and Zhao-Atlas-Marks distributions. In this research, the Choi-Williams distribution (CWD) (so called exponential distribution) is chosen for the chirp signals analysis (Ma et al 1997). CWD can be expressed by an exponential form as (Choi et al 1989)

$$\phi(\eta,\tau) = e^{-\tau^2\eta^2/\sigma^2} \tag{4.16}$$

Here σ is a positive-valued scaling factor. It controls the amount of attenuation. If σ is large enough, then the kernel approaches 1 and CWD representation approaches the WVD. For a small σ, it peaks at the origin and falls off rapidly away from the axis. This property contributes to suppressing cross-terms.

A discrete Cohen distribution for received signal is defined by (Cardoso et al 1996)

$$CD_x(n,k) = 2\sum_{\tau=-N/2+1}^{N/2-1}\left(W(\tau)W^*(-\tau)e^{\frac{-j2\pi k\tau}{N}}\sum_{\mu=-M}^{M}\sqrt{\frac{1}{4\pi\tau^2/\sigma}}e^{\frac{-\mu^2}{4\tau^2\sigma}}x(\mu+n+\tau)x(\mu+n-\tau)\right) \tag{4.17}$$

where n is the time variable and k is the frequency variable. σ is the parameter used to control the properties of the distribution. Large σ implies more smoothing and reduction of the cross-terms. However, this also leads to a greater loss of resolution. $w(n)$ is a symmetrical window (such as Hamming) which has non-zero values in the

interval $-N/2$ to $N/2$ and $w(\tau)$ is a uniform rectangular window with a value of 1 in the range $-M/2$ to $M/2$. The chosen values for N and M on these windows determine the frequency resolution of the CWD and a range where the function is defined.

Bilinear TFR methods can be extended to higher order moment spectral (HOS) domain (Cohen 1989). HoS methods are based on the higher order extensions to the WVD. Although higher order spectra have better resolution, they suffer from an increased number of cross-term interference when dealing with multi-component signals. The cross-terms can be mitigated by incorporating higher order statistics with several methods i.e. Cohen class distributions (Fonollosa et al 1993, Fonollosa et al 1994). In this research higher order spectra were not considered due to similar results to bilinear TFR methods as well as high computational burden.

4.3.3 Simulation Results

Figure 4-5 shows the result of a Chirp-type jammer characterization using the aforementioned bilinear TFR methods compared to the actual time-frequency behavior of the input signal. The WVD method uses of a window size of 10 μs. It depicts auto terms and cross terms attitude by changing the sweep time of the chirp signals. Obviously, increasing the sweep time causes an increase in the accuracy of the auto terms. The downside is that in case more than one chirp resides in the selected window, the WVD method suffers from cross-terms. Using the Cohen distribution with a proper kernel function removes the effect of cross terms. However, it decreases the resolution of the results. Especially, it can be seen in the chirp jammers with lower sweep times. Herein, the value of σ is chosen to be 10^8. Comparing Figure 4-4 with Figure 4-5 shows

that utilizing bilinear TFR methods leads to more accurate estimation with respect to linear TFRs in case of short sweep times (e.g. T_{sw1} = 2.5 μs).

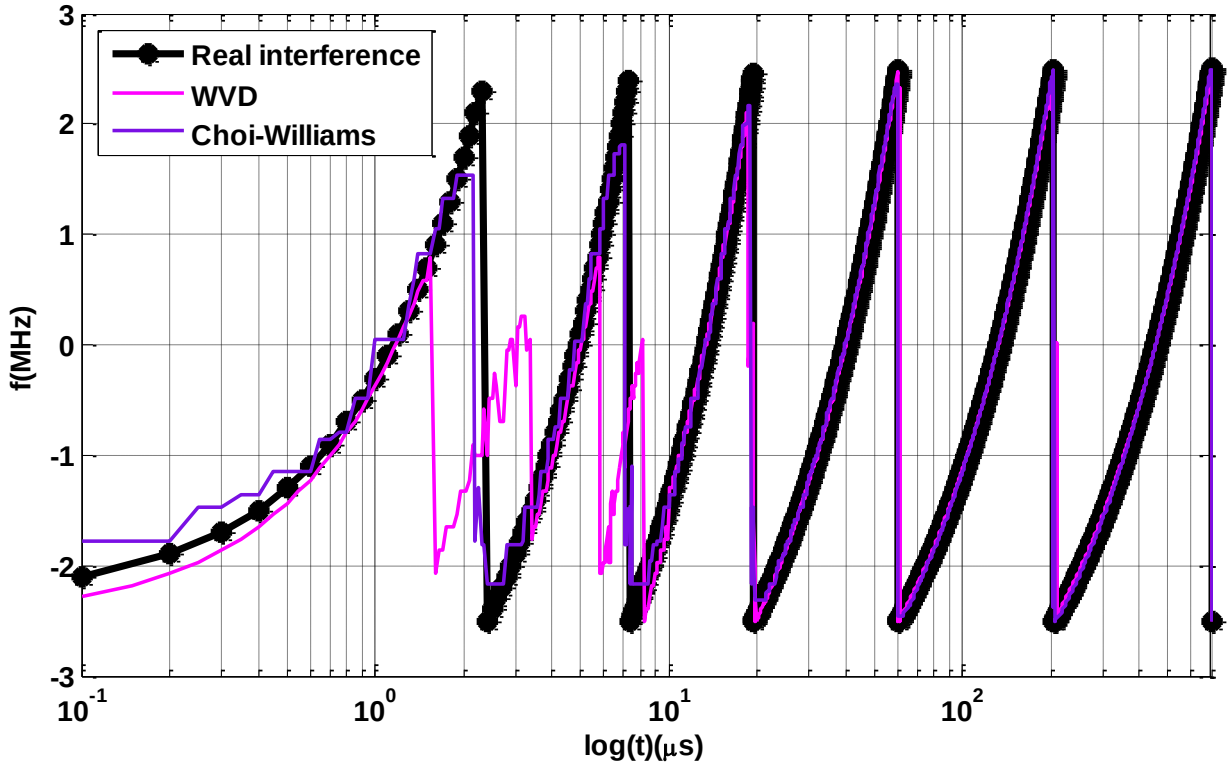

Figure 4-5 Time-frequency representation of chirp-type interference signal and its estimation using bilinear TFR methods

4.4 Adaptive Time-Frequency Analysis

Adaptive TFR methods include adaptive parametric and non-parametric time-frequency analyses. Adaptive parametric time-frequency analysis is based on atomic decomposition methods and represents a signal by a model to best match the time-frequency features according to the signal structural characteristics. Using this technique, it is possible to determine the true constituent signal components, thereby completely removes the cross-terms and obtains a TFR in higher resolution.

Adaptive non-parametric TFR methods include empirical mode decomposition (EMD) based time-frequency analysis methods. They extract the intrinsic mode functions

(IMFs) of the input signal by either data sifting or data smoothing. Hence these approaches are completely signal-driven and there is not any basis function for signal decomposition.

In this section the windowed Hilbert Huang transform and matching pursuit method are considered as adaptive non-parametric and parametric techniques, respectively.

4.4.1 Windowed Hilbert-Huang Transform

In this section, a windowed HHT method is proposed for RFI characterization and its performance is compared with the traditional HHT. HHT, introduced by Huang et al (1998), is a signal decomposition method that assumes the signal is the superposition of a finite number of sub-signals. Unlike other signal analysis tools such as STFT which has a set of known basis functions, HHT does not require any a priori bases and the bases are constructed according to input signal characteristics. The HHT algorithm consists of two parts. Firstly, the primary signals are decomposed into series of time-dependent intrinsic mode functions (IMFs). Secondly, the instantaneous frequency and amplitude are obtained from the Hilbert transform of each IMF.

The process of decomposing input signals into IMFs is known as empirical mode decomposition. The IMF must satisfy the following two conditions:

i. The number of extrema and the zero crossing must be equal or distinct at most by one.
ii. At each point, the mean value of the envelope defined by the local maxima and the envelope defined by the local minima are zero.

The complexity of the traditional HHT is very high due to the number of recursions in

IMFs calculations for the input signal. Since one of the main goals of the characterization is to extract the interference properties, there is no need to calculate noise-related IMFs. In other words, only the IMFs which include significant parts of the jammer are decomposed from the input signal.

The sifting process involves recursive IMFs and signal residual calculations. For the proposed method, this process is modified by a recursion termination condition based on an interference detector chosen from methods described in Chapter 3. The process can be described as follows:

a. Find all the extrema points of the l^{th} window of the real part of the input signal denoted by $x_l(n)$.
b. Connect all the extrema points by cubic spline interpolation to determine the upper and lower envelopes.
c. Compute the average of the upper and lower envelopes (i.e. $ave_l(n)$).
d. Find the difference between the signal $x_l(n)$ and its average calculated in step c (i.e. $x_{1\_l}(n)$):

$$x_{1\_l}(n) = x_l(n) - ave_l(n) \tag{4.18}$$

e. Treat $x_{1\_l}(n)$ as $x_l(n)$, and repeat the steps a to d until $x_{1\_l}(n)$ satisfies the above conditions of an IMF. In this case, $x_{1\_l}(n)$ is called an IMF (i.e. $I_i(n)$).
f. Subtract $I_i(n)$ from $x_l(n)$ to get the residue (i.e. $r(n)$):

$$r(n) = x_l(n) - I_i(n) \tag{4.19}$$

g. Analyze $r(n)$ with a jammer detector to detect the presence of jammer in the residue part of the input signal. If the jammer signal is not detected, the process will be terminated.

h. Treat the residual ($r(n)$) as $x_l(n)$. Repeat the aforementioned process to obtain the other IMFs until $r(n)$ is a monotone or constant function.

According to the above procedure, the sifting process continues only if a jammer can be detected in the residual term. The EMD process flowchart is shown in Figure 4-6.

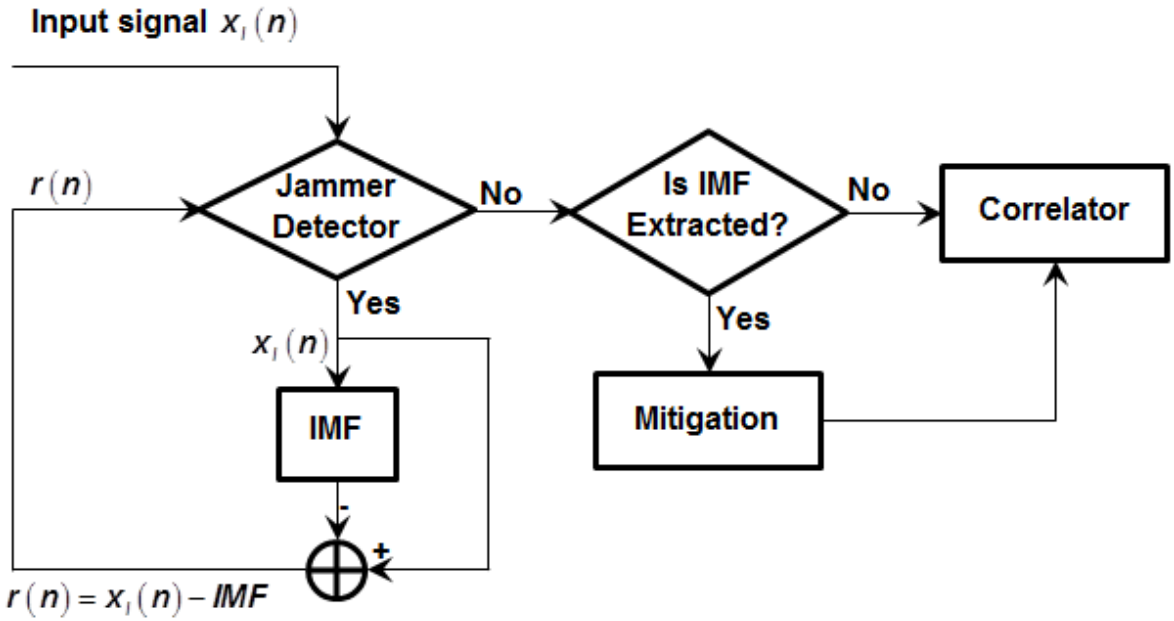

Figure 4-6- Flowchart of HHT characterization section

Figure 4-7 shows an example of signal decomposition into IMFs and the residuals for a Group II chirp signals using the traditional HHT. For the proposed windowed-HHT

method, only the first IMF is extracted. Hence, the computational burden is reduced significantly.

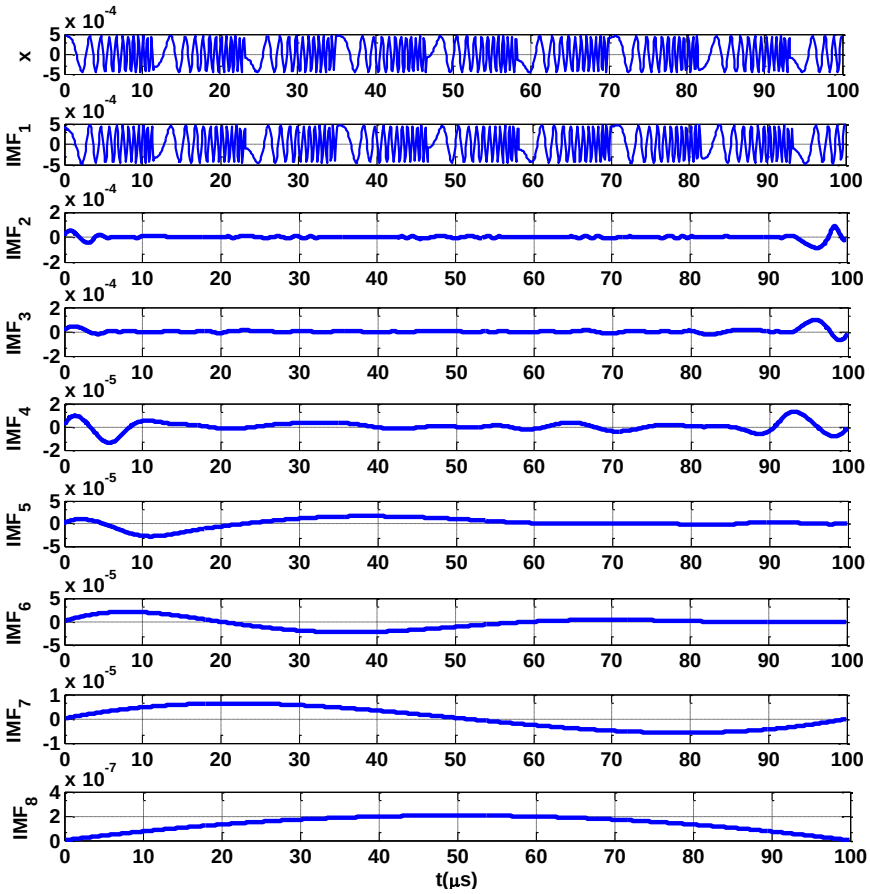

Figure 4-7 IMFs and residual plots of a Group II jammer

After IMF calculations, the Hilbert transform is utilized for each IMF to derive its corresponding imaginary part defined in continuous-time as (Huang et al 1998)

$$\tilde{I}_i(t) = \frac{1}{\pi} pv \int \frac{I_i(\tau)}{t-\tau} d\tau \qquad (4.20)$$

where pv is the Cauchy principal value of this integral. Assuming a Hilbert transform, the analytical signal for the i th IMF is defined as

$$Z_i(n) = I_i(n) + j\left(\tilde{I}_i(n)\right) \tag{4.21}$$

The amplitude $a_i(n)$ and phase $\theta_i(n)$ functions can be described as follows:

$$\begin{cases} a_i(n) = \sqrt{\left(I_i(n)\right)^2 + \left(\tilde{I}_i(n)\right)^2} \\ \theta_i(n) = \tan^{-1}\left(\dfrac{\tilde{I}_i(n)}{I_i(n)}\right) \end{cases} \tag{4.22}$$

Thus, the instantaneous frequency can be expressed as

$$f_i(n) = \frac{\theta_i(n) - \theta_i(n-1)}{2\pi \times T_s} \tag{4.23}$$

4.4.2 Matching Pursuit

As mentioned in Section 4.3.2, parametrized TFR methods are among the best approaches to suppress the WVD cross terms. These methods attract considerable attention because of their signal-dependent resolution and highly concentrated TFR. An appropriate example of parameterized methods is the matching pursuit (MP). The MP algorithm was first proposed by Mallat et al (1993) and Qian et al (1994) to adaptively decompose a signal into optimally matched chirplets. Chirplets are obtained through translating, scaling and shearing a mother chirplet and are a suitable choice for characterizing chirp-type signals. The mother chirplet is a function specially designed for linear modulated signal analysis. By using an extra parameter, i.e. chirp rate, the chirplet transform can obtain a well concentrated TFR. For chirp argument estimation, this research is denoted the standard chirplet transform that uses a unified chirp rate.

A received signal $x(n)$ can be presented as a weighted sum of Chirplet functions (Cui et al 2005):

$$x(n) = \sum_{i=1}^{N} A_i e^{j\varphi_i} \Omega(m_i, t_i, \omega_i, c_i, d_i) \tag{4.24}$$

where φ is the phase shift of the wave and $\Omega(m_i, t_i, \omega_i, c_i, d_i)$ is the Gaussian Chirplet function given by

$$\Omega(m, t_0, \omega, c, d) = \left\{ \frac{1}{\sqrt{d\sqrt{2\pi}}} e^{-\left(\frac{m-t_0}{2d}\right)^2} \right\} \times \left\{ e^{j\left[c(n-t_0)+\omega\right](n-t_0)} \right\} \tag{4.25}$$

where t_0, ω, c and d represent the location of time, frequency, chirp rate and duration of the Gaussian Chirplet respectively and m is the time variable. In Equation 4.25, the first bracket shows a Gaussian envelope where t identifies the centre of the energy concentration in time and d shows the spread of the envelope. The second bracket presents the linear modulation of a chirp signal. An example of a Gaussian Chirplet function is illustrated in Figure 4-8.

Chirplet decomposition selects a group of optimal chirplets from a pre-defined atom dictionary. Multi-dimensional parameters including time (t_0), frequency center (ω), chirp-rate (c) and time duration (d) are chosen from pre-defined ranges and are known as discretized atoms of the dictionary.

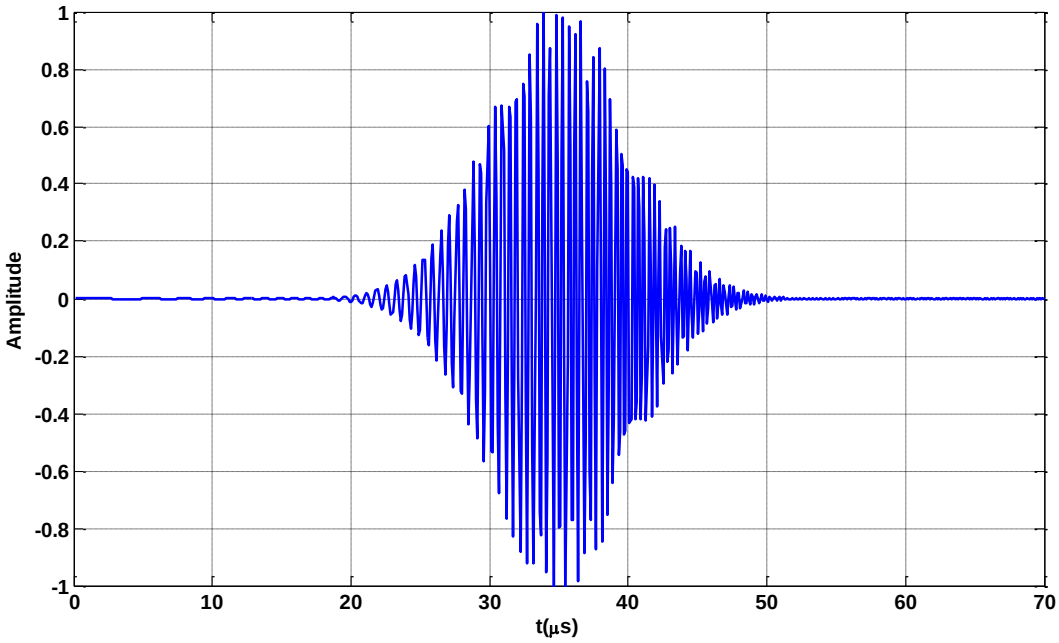

Figure 4-8 Gaussian chirplet function (with d =5x10-6, t_0 =10-10(s), c =6x1010(Hz/s) and sampling frequency = μ(MHz))

This transform comprised four basic operations including scaling, time shift, frequency shift and rotation. Assume an input chirp signal of the form of

$$x(t) = Ae^{i\left(\omega_0 t + \lambda_0 t^2/2\right)} \tag{4.26}$$

where ω_0 and λ_0 are initial frequency and chirp rate, respectively. In this case, the instantaneous frequency is equal to $f(t) = \omega_0 + \lambda_0 t$. Figure 4-9 illustrates the raw signal frequency as well as the rotation and shift operation in chirplet transform to estimate the initial frequency and slope of the chirp signal. The rotation operator rotates the input signal by angle $\theta = \tan^{-1}(-c)$ in time-frequency plane. The shift operator relocates the frequency component from ω to $\omega + ct_0$.

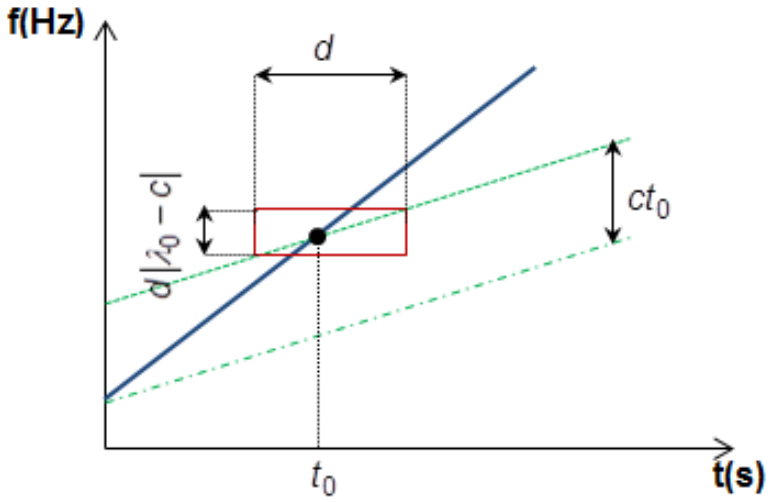

Figure 4-9 An illustration of rotation and shift operators (Blue line: IF of the signal, green dot-dash line: frequency rotation, green dot-dot: frequency shift)

It can be seen from Figure 4-9 that the time bandwidth is d and frequency bandwidth of the widowed signal is $d\left|\lambda_0 - c\right|$(Yang et al 2014). Hence, when $\lambda_0 = c$, the frequency rotation reaches its minimum value.

As mentioned before, the disadvantage of WVD is the production of inevitable cross-terms. To alleviate this adverse effect, a standard chirplet transform is proposed. In so doing, the input signal is decomposed into its mother chirplets. Then, each mother chirplet is used as the input of a WVD.

The decomposition method, as described by Cui et al (2005), is an adaptive windowed chirplet. The first step in this method, also known as matching pursuit (MP), is to divide the input signal into short block windows. The procedure for finding the optimal widow length is described by Cui et al (2006). The second step is to choose a chirplet atom from a dictionary (Ω) such that the amplitude of the inner product (chirplet coefficient) between this atom and signal $x(t)$, i.e.$\left|\langle x,\Omega_0 \rangle\right|$ is maximum (the chosen dictionary for

n^{th} iteration is referred to as Ω_n). Then, the residual signal r_1 is obtained from $r_1 = x - \langle x, \Omega_0 \rangle$. This iterative procedure is applied to the subsequent residues as follows

$$\begin{cases} r_0 = x; \\ r_{n+1} = r_n - \langle r_n - \Omega_n \rangle, n \in \mathbf{Z} \end{cases} \tag{4.27}$$

where n is the number of iterations. Hence, the signal $x(t)$ is decomposed into the sum of several chirplet atoms and a residual component.

$$x = \sum_{n=0}^{m} \langle r_n, \Omega_n \rangle \Omega_n + r_{n+1} \tag{4.28}$$

Each chirplet atom includes the best estimation of chirp rate (c), time (t_0), frequency center (ω) and the duration (d).

Figure 4-10 shows a 10 μs window of input signal analyzed with the MP method. The input signal is decomposed into three chirplets. Each chirplet atom includes a rough estimation of a section of the selected window. It is used as the input of the WVD method to obtain a more accurate result. Since each decomposition part has the information of only one chirp signal, the cross-terms of the WVD method are eliminated

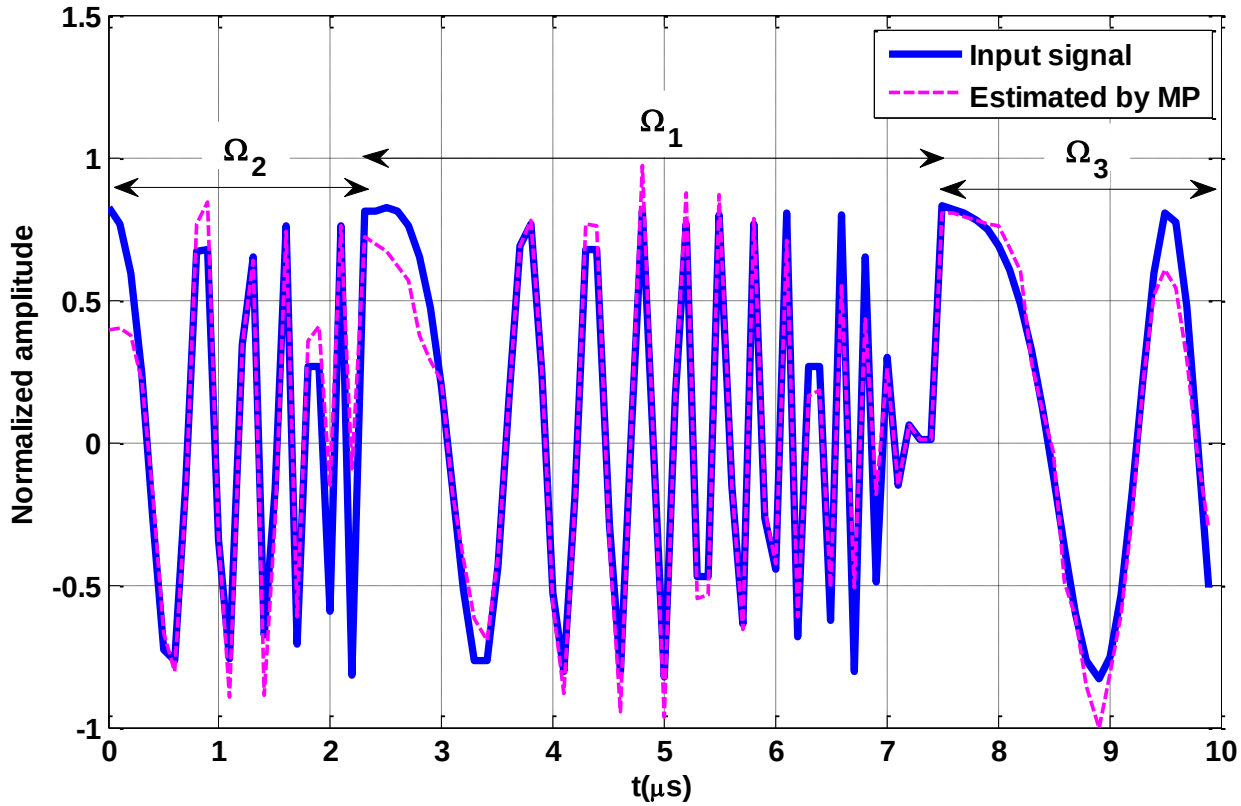

Figure 4-10 Example of estimating the jammed signal using MP method

4.4.3 Simulation Results

Figure 4-11 shows the result of a chirp-type jammer characterization using adaptive TFR methods compared to the actual time-frequency behavior of the input signal. The simulation scenario is described in Section 4.2.4. A window size equal to 10 μs was chosen for the windowed-HHT method. It can be seen that the windowed-HHT method can adaptively resolve the time-frequency plane. Furthermore, its performance is not affected significantly by window size as long as it is not overly small compared to one chirp length. The estimated instantaneous frequency by windowed-HHT fluctuates around its true value. In order to reduce the uncertainty in frequency estimation while using windowed HHT method, a smoothing operation using Hough transform will be proposed in Section 5.4.

This figure also shows the simulation result of the MP method. As observed, this method is a precise technique to characterize chirp signals with different sweep times and the performance is comparable to smoothed-HHT.

Adaptive time-frequency analyses are applicable for the chirps with very short sweep-times such as the first chirp of Figure 4-11. Hence, these methods are useful when there is an abrupt frequency change within the window of interest.

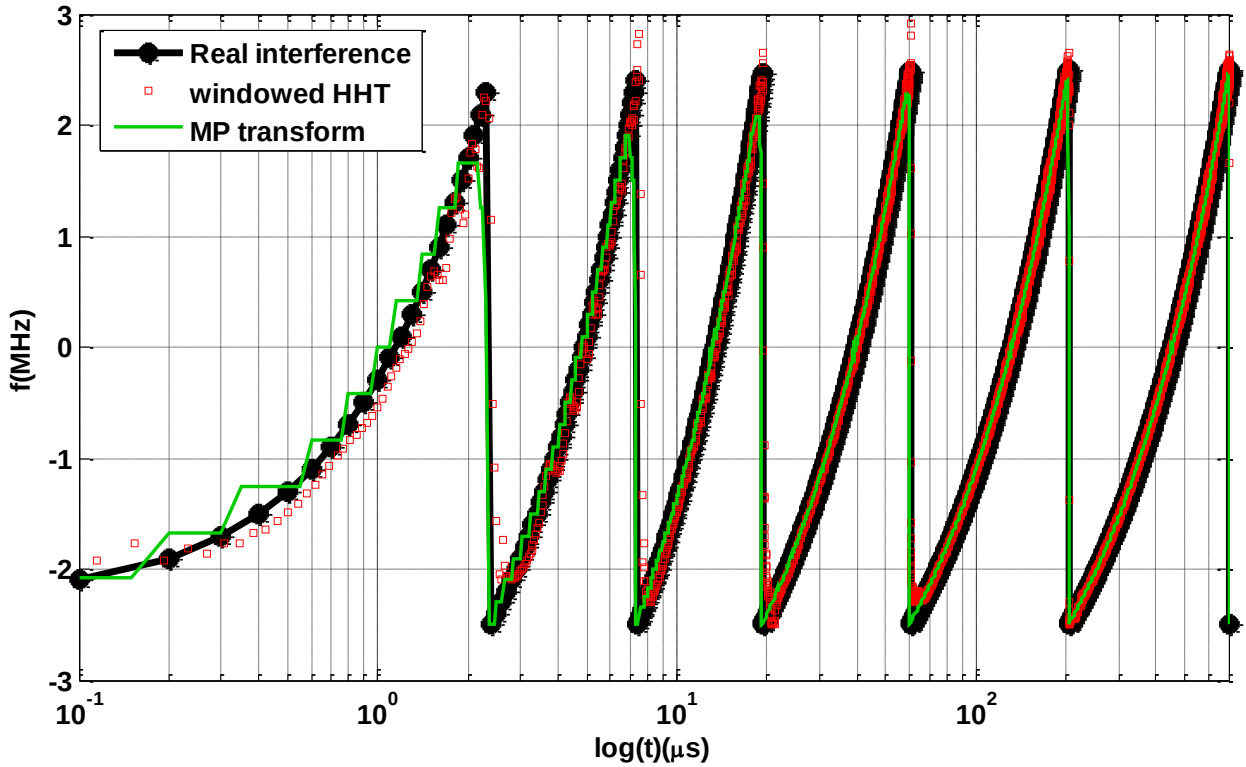

Figure 4-11 Time-frequency representation of chirp-type interference signal and its estimation using adaptive TFR methods

4.5 Computational Complexity

One of the key steps in algorithm selection for jammer characterization and mitigation is the computational burden. It is especially important when low-cost devices are being used as the hardware platform for interference suppression. Generally speaking, more complex algorithms may result in better performance but at the cost of a higher

computational burden. This section analyses the computational complexity of the various TFR characterization algorithms. As a globally accepted notation, hereafter, the symbol $O(\ )$ (known as big-O) is used for this purpose. The $O(\ )$ notation provides an approximation of the number of operations required by a specific algorithm. It should be mentioned that the complexity is a function of both the number of operations and the cost of different operators such as addition and multiplication. The former is independent of the hardware platform and is an intrinsic property of the algorithm, whereas the latter is merely hardware-dependent. Since a specific method can be implemented on various platforms, the literature excludes the cost of operators. Likewise, hereafter it is presumed that operators cost (which are mostly math and logical operators) are unity and are excluded from the analyses.

In STFT method, the FFT method is based on the divide-and-conquer approach and the The N-point FFT computation requirement is in the order of $O(N\log N)$. Herein, N denotes the window width of the STFT method.

Rioul et al (1991) have studied the computational complexity of Wavelet transforms. In general, an efficient implementation is possible due to decimation of input samples in each level. Each level of Wavelet decomposition consists of two filters through which the signal is divided into low and high frequency bands. The details of the filter structure and coefficients will be described in Section 5.3. For now, it is assumed that the filters are L-taps Finite Impulse Response (FIR). The filtered outputs at each step are decimated by a factor of 2. This necessitates the computation of those signal samples that are not thrown away. Consider an input set of N samples. For the first level, each

filter computes $N/2$ samples, leading to the total number of N samples generated at the low-pass and high-pass filters in level-1 of Wavelet. Similarly, each filter in the second-level computes $N/4$ samples, and the total number of samples computed at level-2 is $N/2$. It is trivial to show that a L-taps FIR requires L multiplications as well as $L-1$ addition in order to compute one output sample. Therefore, the total number of multiplication in an m-level Wavelet can be expressed as

$$NL\left(1+\frac{1}{2}+...+\frac{1}{2^{m-1}}\right)=2NL\left(1-2^{-m}\right) \qquad (4.29)$$

and the total number of additions is

$$N\left(L-1\right)\left(1+\frac{1}{2}+...+\frac{1}{2^{m-1}}\right)=2N\left(L-1\right)\left(1-2^{-m}\right) \qquad (4.30)$$

Assuming that the number of levels and the number of filter taps are much larger than one, the computational complexity can be simplified as $O\left(NL\right)$.

According to Equation 4.11, the S-transform coefficients are calculated for all *M* frequency bins and all *N* time epochs. For each coefficient, it requires *N* operations due to the summation. Hence, for a signal of length N , the discrete S-transform generates $N.M$ coefficients and requires N^2M operations. Since it is possible to take advantage of the FFT algorithm, the minimum complexity of the S-transform is equal to $NM\log(N)$. Therefore, large amount of calculation time is required for transforming even a moderate size signal into its discrete S-transform coefficients.

Similar to the S-transform, the complexity of the Wigner-Ville distribution is equal to $O(N^2 \log N)$ according to Equation 4-13 and assuming N frequency bins.

Considering Garcia-Nocettif et al (2002) and Equation 4.17, the computational complexity of the Choi-Williams distribution requires $\left(8N^2 - 4N\right)$ complex multiplications and $\left(4N^2 - 6N + 2\right)$ complex additions for every specific time variable n.

In the windowed-HHT method, the computation burden at each step includes the extrema search, interpolation of upper and lower envelopes, as well as sifting means and ensemble IMFs. Defining N_E as the number of ensembles, N_I as the number of IMFs, N_{Ave} the number of average extrema per IMF and N as the window length, the computational complexity for each section is

- $N_E \times N_I \times N$ addition operations for the exterma determination.
- $N_E \times N_I \times N_{Ave}$ division operations, $N_E \times N_I \times \left(N_{Ave} + N\right)$ addition operations and $N_E \times N_I \times \left(N_{Ave} + N\right)$ multiplication operations for interpolating the upper and the lower envelopes.
- $N_E \times N_I \times N$ addition operations for sifting.
- $N_E \times N_I \times N$ addition operations and $N_I \times N$ multiplication operations for the ensemble IMFs.
- In order to calculate the computational complexity of Hilbert transform, instead of implementing the integral, it is approximated by a FIR filter of length L. Hence, the complexity of the filter is $\left(L - 1\right)$ addition operations and L multiplication operations.

As the size of window length is N, the computational complexity of Hilbert transform is $O\left(N\times\left(\left(L-1\right)+\mathrm{L}\right)\right)$.

In most cases in the proposed method, N_I is equal to 1. Moreover, if it is assumed that the cost of addition, multiplication and division are the same, then ones can assume that the computational complexities of different EMD steps are approximately similar to each other and equal to $O\left(kN\right)$.

The MP algorithm is an iterative method. For each iteration, the correlation between the received signal and a chirplet function is calculated with different parameters from the dictionary. Let's assume that there are L iterations for N samples of received signal. Furthermore, the dictionary size is assumed to be K. Therefore, the computational burden of the MP method is $O(L\times N\times K)$. However, the coarse output of MP at each iteration is fed into the WVD for fine frequency estimation whenever there is a change in the estimated slope. In other words, in the worst case the WVD algorithm is called L times over N samples. As previously mentioned, the WVD complexity in this case is equal to $O(\mathrm{N}^2\mathrm{logN})$. Therefore, the worst case computational load of the MP method is $O(\mathrm{N}+\mathrm{N}^2\mathrm{logN})$.

Figure 4-12 provides a relative comparison of the computational complexity of various discussed characterization techniques. The execution time of each method is extracted by MATLAB "profile" function on a windows server 2012 PC with a 2.6 GHz CPU and 32 GB of RAM. The computational requirement of each algorithm for the same data set is reported. The lowest execution time corresponds to the STFT, WT and WVD

techniques. The execution time of the S-transform and windowed HHT (wHHT) are higher. The highest execution times correspond to Cohen distribution analysis and matching pursuit method. For every method, the simulation was executed 1000 times and the processing times were averaged and normalized. It should be mentioned that this is a rough estimation since these values depend on the computer architecture and algorithms implementation details.

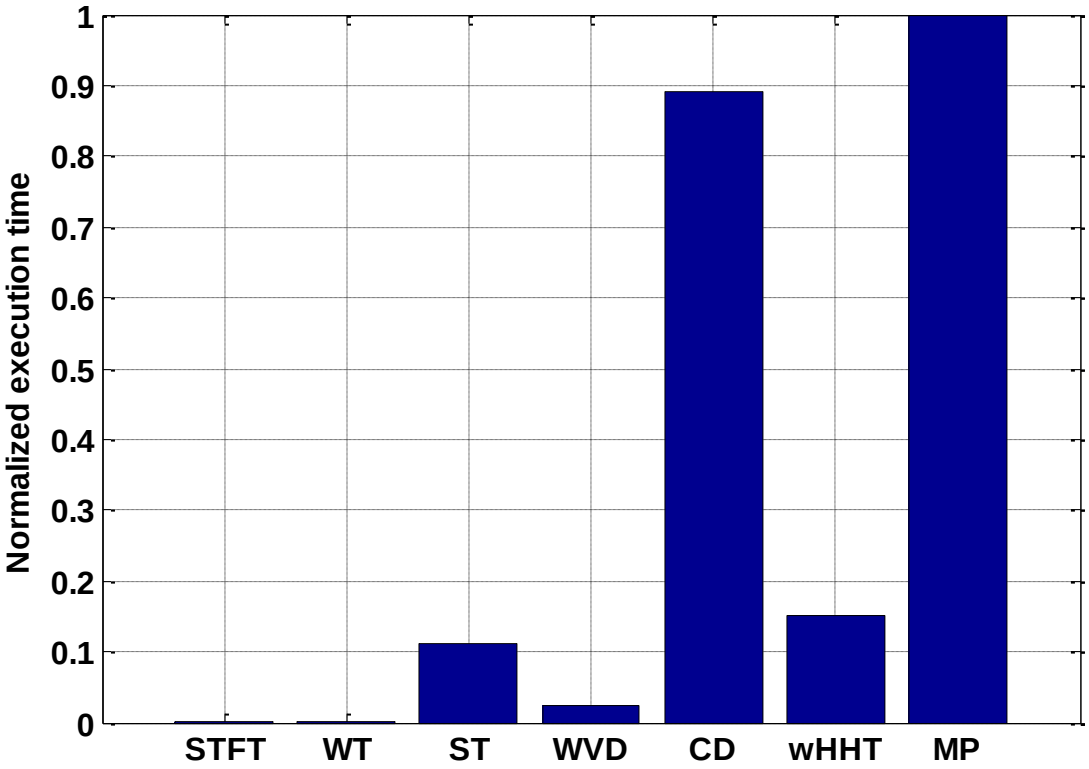

Figure 4-12 Normalization of processing time for characterization techniques

4.6 Summary

This chapter compared several time-frequency representations for characterizing chirp-type interference sources on GNSS signals. Table 4-1 shows a comparison among the advantages, disadvantages and cost of all discussed methods.

Table 4-1 Comparison of several TFRs

Method	Advantages	Disadvantages	Computational Cost
STFT	Free from cross-terms, fast implementation	Constant window width limits TFR resolution	Low
WT	Free from cross-terms, effective in detecting transients	Does not maintain the absolute phase of the signal components. Challenging in wavelet basis selection.	Low
S-Transform	Variable resolution. Absolute phase of each component is Maintained	Higher computational complexity among linear TFR methods	Moderate
WVD	High time-frequency resolution	cross-term interference of multi-component signals	Low
CD	Suppressed cross-terms	Suppression of cross-terms can lead to reduced TFR resolution	High
Windowed-HHT	High time-frequency resolution, adaptive signal decomposition	Difficult to resolve signal components when there is an abrupt frequency change in the chirp signal	Moderate
MP	Free from cross-terms, High time-frequency resolution	Needs a priori knowledge to construct dictionary, high computational complexity	High

Chapter Five: GNSS Interference Mitigation based on Pre-Correlation Methods

5.1 Introduction

The focus in this chapter is to investigate different chirp-type jammer mitigation methods. Time-frequency mitigation techniques usually rely on using characterization section parameters. This information is employed to control the coefficients of an excision filter that adaptively removes the interference signal (Tazebay et al 1998) or to generate a replica signal similar to the jammer. Accordingly, there are two general approaches for interference mitigation. The first approach cancels the effect of jammer through a filtering operation. Generally, an adaptive band-stop filter that tracks and nullifies the instantaneous frequency content of the jammer is implemented. Figure 5-1 shows the structure of the interference suppression unit (ISU) based on this approach. The filtering operation can be performed either in the time or frequency domain. In this regards, the notch filtering method is considered time-domain excision whereas the Fractional Fourier transform (FrFT) and Wavelet packet decomposition (WPD) methods can be considered frequency-domain filtering approaches to jammer mitigation.

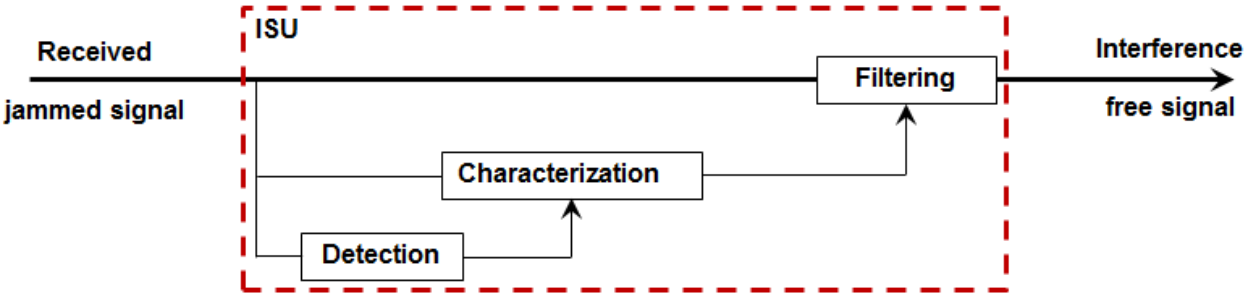

Figure 5-1 Structure of proposed filtering based ISU

The second approach synthesizes the interference by an inverse transform and subtracts the local replica from the input signal. This replica resembles the jammer and

nullifies the RFI effects. Figure 5-2 shows the structure of the ISU based on this approach. The Hilbert-Huang Hough transform (HHHT) is an example of this approach.

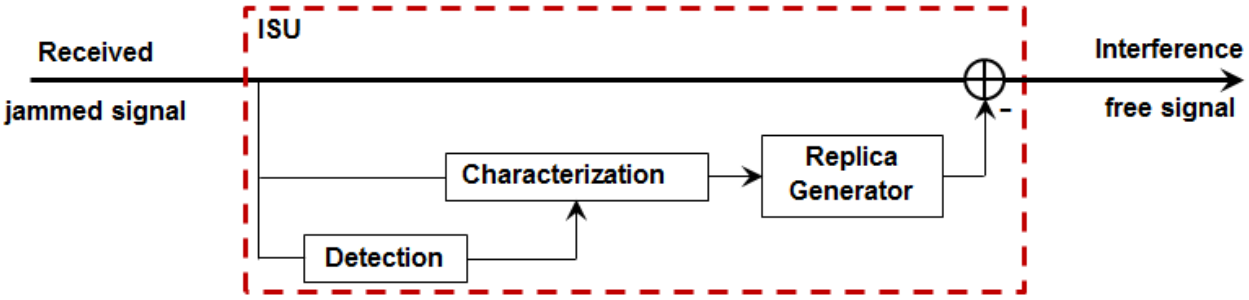

Figure 5-2 Structure of proposed jammer synthesis ISU using replica generator

This chapter presents FrFT, WPD, HHHT and notch filtering mitigation techniques. One of the main goals is to compare their performance and computational complexity. In so doing, a realistic GPS signal is combined with chirp-type jammers with various levels of JNR. The jammed signal is fed into a proposed ISU unit. The output jammer mitigated signal is then fed to a GPS software receiver to see how well the ISU can eliminate the destructive jammer effects. For this purpose, the GSNRx^{TM} software receiver is utilized (Petovello et al 2008).

The proposed mitigation techniques can be applied to all civil-jammer groups, which were described in Section 2.6. In this chapter, the jammer signals in GPS L1 band are considered. However, these methods are not related to the specified center frequency and can also be applied to other GNSS frequency bands.

5.2 Filtering Based Mitigation Methods

The filtering methods are in fact adaptive filters that remove the time-varying jammer contents from the received signal. In this research, FrFT, WPD and notch filtering are considered in this category.

5.2.1 Fractional Fourier Transform

The FrFT is a variant of the Fourier transform utilized for jammer mitigation. It is a generalization of the ordinary Fourier transformation whereby the signal is rotated in the time-frequency plane (Ayaz 2013). Hence, this is a suitable method for suppression of chirp-type signals by measuring the angular distribution of signal's energy in the time-frequency plane. For the input signal $x(n)$, the definition of the FrFT for the α^{th} rotation angle is given by (Sejdić et al 2011)

$$\begin{aligned} X_\alpha(m) &= A_\alpha \times \exp\left(\frac{j}{2}\cot\left(\alpha m^2 \Delta u^2\right)\right) \\ &\times \sum_{n=-N}^{N}\left(\exp\left(-j\frac{2\pi nm}{2M+1}\right)\times\exp\left(\frac{j}{2}\cot\left(\alpha n^2 T_s^2\right)\right)\times x(n)\right) \end{aligned} \tag{5.1}$$

where m and T_s are the variable in the a^{th}-order fractional Fourier transform and sampling time respectively. $X_\alpha(m) = X_\alpha[m\Delta u]$ and α is known as the rotation angle and is equal to $\alpha = \frac{\pi \times a_{opt}}{2}$. Moreover, the optimum transform order (a_{opt}) is given by (Ayaz 2013) as

$$a_{opt} = -\frac{2}{\pi}\tan^{-1}\left(\frac{F_s^2 \times T_{sw}}{2 \times N \times BW}\right) \tag{5.2}$$

where F_s is sampling frequency, T_{sw} and BW are sweep time and bandwidth of jammer, respectively. In addition, N and M are the number of points in the time (window length) and frequency domain and the constraint of $M \geq N$ must be satisfied. The A_α parameter is calculated by (Sejdić et al 2011)

$$A_\alpha = \begin{cases} \sqrt{\dfrac{-\sin\alpha - j\cos\alpha}{2M+1}} & \alpha \in 2D\pi + (-\pi, 0), D \in \mathbf{Z} \\ \sqrt{\dfrac{\sin\alpha - j\cos\alpha}{2M+1}} & \alpha \in 2D\pi + (0, \pi), D \in \mathbf{Z} \end{cases} \tag{5.3}$$

The FrFT of a chirp with a matched sweeping rate is localized as an impulse with the maximum value for a specific jammer signal power. The position of the peak is a function of the chirp start frequency and frequency sweep slope. The order parameter has to be chosen properly for the chirp signal that tunes the transformation to give optimal response. After determining the chirp slope and initial frequency using one of the proposed methods in Chapter four, the mitigation method attempts to cancel out the interference by frequency-rate domain filtering. The basic idea is that filtering in the time-domain is equivalent to frequency-domain multiplication to the filter frequency response. Hence, a notch filter (frequency masking operation) containing 0s at chirp location (delta bins) and 1s at the other frequency bins is multiplied by the FrFT transform of the signal and then transformed back into the time-domain. The back transformation into the time domain is performed using an inverse FrFT operation which is simply an FrFT with a rotation angle of $-\alpha$ (Sejdić et al 2011). Figure 5-3 shows the block diagram of the FrFT RFI mitigation method.

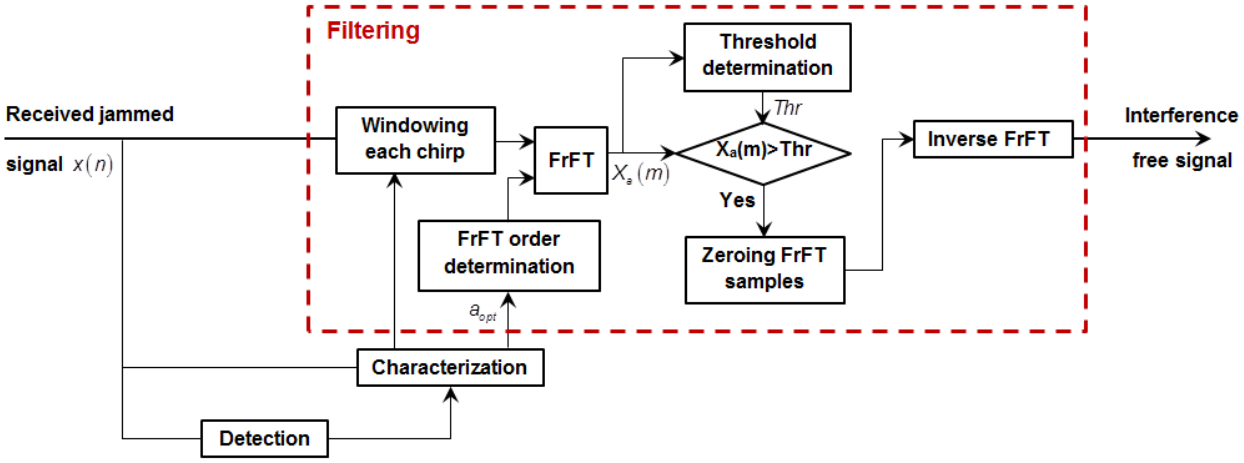

Figure 5-3 Flow chart of FrFT mitigation technique

The outputs of the mitigation section before and after the frequency masking operation are illustrated in Figure 5-4. The threshold is calculated using the maximum value of the FrFT bins of interference free segment of the signal.

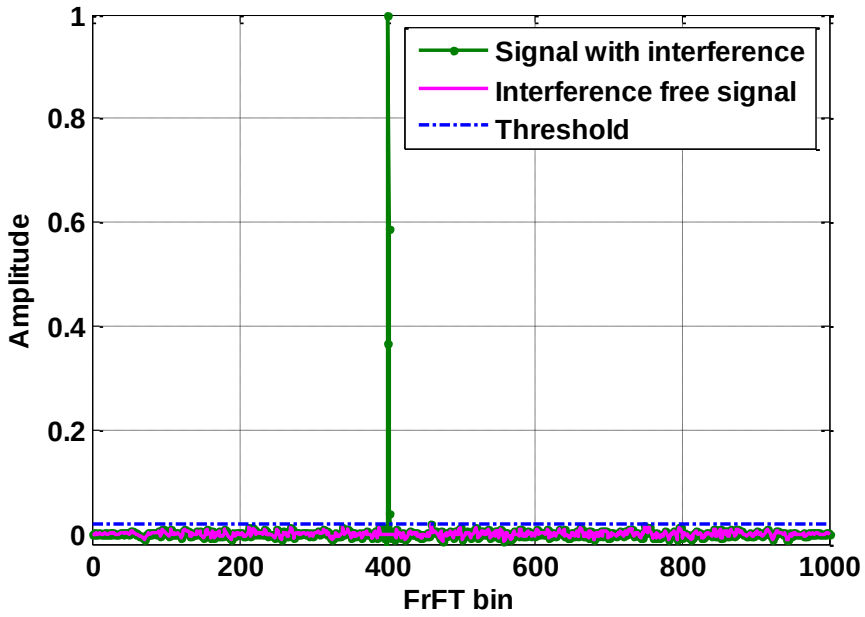

Figure 5-4 Frequency masking of the bins containing interference

The numerical threshold value can be defined by (Millioz et al 2012)

$$\gamma = -\sigma^2 \ln\left(1-\left(1-P_{fa}\right)^{1/N}\right) \tag{5.4}$$

where σ^2 is the variance of FrFT of clean window of size *N* and P_{fa} is the pre-defined probability of false alarm. Herein, a P_{fa} equal to 10^{-5} is selected for threshold calculation.

5.2.2 Wavelet Packet Decomposition

The definition of DWT can be expanded by calculating wavelet packets decomposition (WPD) (Musumeci et al 2013) where the discrete time input signal ($x(n)$) is passed through a wavelet based filter bank, as shown in Figure 5-5. The scaling and shifting process (defined in Section 4.2.2) are iterated in a filter bank. The output of each filter provides a set of coefficients (scales). Each scale presents a determined frequency portion of the incoming decomposed signal.

Initially, the input samples are passed through a low pass filter (LPF) with an impulse response of LPF_1. The resulting output y(n) is determined by the convolution operation as

$$y(n) = (x * LPF_1)(n) = \sum_{k=-\infty}^{+\infty} x(k) LPF_1(n-k) \tag{5.5}$$

Equation 5.5 results in the so-called approximation coefficients. Similarly, the signal is also decomposed simultaneously using a high pass filter (HPF) which gives the so-called detail coefficients. These two filters, which are related to each other, are called quadrature mirror filters. Since half of the frequencies of the signal is removed after filtering, the decomposition has halved the time resolution. Hence, the filter outputs can be sub-sampled by 2.

In this research, the Meyer wavelet function is used for mitigation purpose. As shown in Figure 4-2, the transfer functions for each branch of the filters bank obtained by a dyadic scaling operation of the wavelet function.

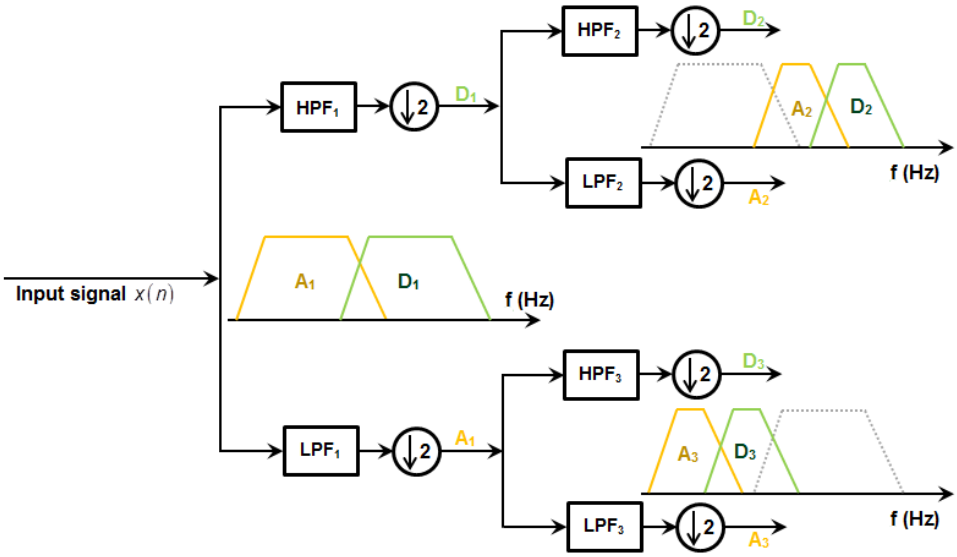

Figure 5-5 Wavelet packet decomposition in a 3-level filter bank by a dyadic scaling operation

The mitigation algorithm, which is shown in Figure 5-6, is based on WPD and describes on three steps (Musumeci et al 2013, 2014). The decomposition (characterization) step extracts the time-scale representations. The second step, known as the detection-mitigation step, performs a blanking operation on each scale. Since the wavelet filtering levels are performed with unitary energy filters, hence a pre-defined threshold is adequate for all scales after masking operation. The values that are greater than threshold are supposed to be interference and are suppressed. For a given false probability P_{fa}, the threshold can be calculated as (Musumeci et al 2013).

$$\gamma = \sqrt{2} \times \sigma_{IF} \times erfc^{-1}(P_{fa}) \tag{5.6}$$

which in $\sigma_{IF}^{\ 2}$ is the variance of interference free signal and $erfc(\ )$ is the complementary error function defined as.

$$erfc(x) = \frac{2}{\sqrt{\pi}} \int_{x}^{\infty} \exp\left(-t^2\right) dt \tag{5.7}$$

The last step in WPD is the reconstruction stage which involves passing all frequency masked scales through the reconstruction filter banks. A reconstruction filter bank performs the inverse operation with respect to the decomposition filter bank. In other words, every downsampling operation in the decomposition is replaced with an upsampler in the reconstruction. Likewise, each LPF is replaced with its equivalent HPF. The same Wavelet function that is used for decomposition must be employed for signal reconstruction as well.

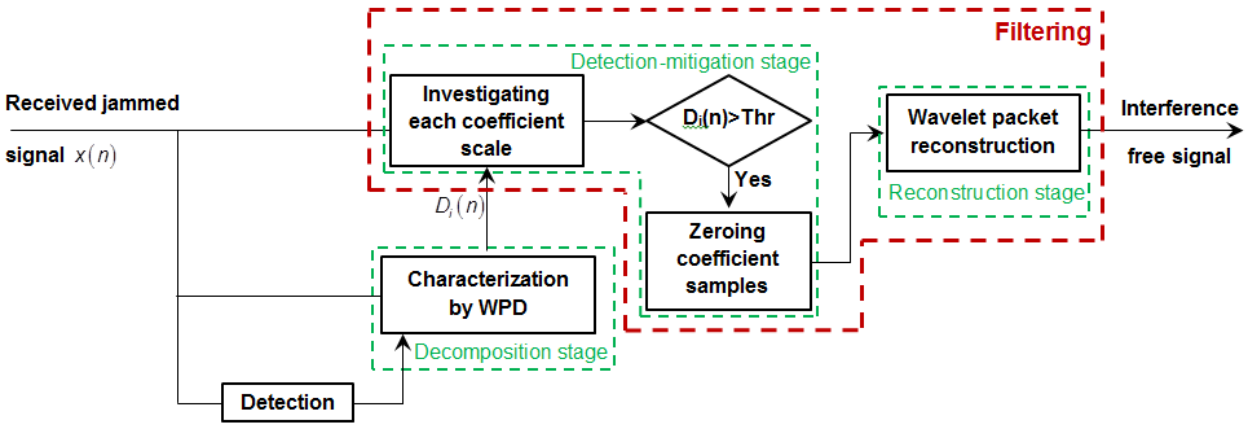

Figure 5-6 Flow chart of WPD mitigation technique

5.2.3 Notch Filtering

The adaptive notch filtering is one of the commonly used pre-despreading mitigation techniques due to its simplicity, especially for low cost receivers. In contrast to FrFT and

WPD which perform masking operation in the time-frequency domain, the adaptive notch filter attempts to cancel out the interference effect solely in the time domain. The core idea is to adaptively adjust the frequency response of a band-stop filter such that the jammer spectrum is rejected at each time epoch.

This method, by providing attenuation on the interfering signal, preserves the GNSS signal spectral components. One of the most common notch filtering methods is based on infinite impulse response (IIR) digital filters. Compared to finite impulse response (FIR) filters, IIR filters have recursive and simpler structure. In fact, an IIR filter provides the same performance as an equivalent FIR one but with lower order (less number of taps and operations). The downside is non-linear phase responses of IIR filters which introduces frequency-dependent group delays and adversely affects on GNSS measurements such as carrier phase and code delay. This effect is more destructive especially in the case of GLONASS signals which use a frequency division multiple access (FDMA) channel access scheme.

The distribution of a single real CW jammer presents two spectral lines at the frequencies f_i and $-f_i$. The effect of this interference can be removed using the following filter with two complex conjugate 0s corresponding to the frequencies z_0 and z_0^*:

$$H_{MA}(z) = \left(1 - z_0 z^{-1}\right)\left(1 - z_0^* z^{-1}\right) = 1 - 2\mathrm{Re}\{z_0\} z^{-1} + |z_0|^2 z^{-2} \tag{5.8}$$

The above equation is the moving average (MA) part of the filter where $z_0 = \beta e^{j2\pi f_i}$. An auto-regressive (AR) block is added to compensate the effect of MA part on the other frequencies:

$$H_{AR}(z) = \frac{1}{\left(1 - z_0 k_\alpha z^{-1}\right)\left(1 - z_0^* k_\alpha z^{-1}\right)} = \frac{1}{1 - 2k_\alpha \,\mathrm{Re}\{z_0\} z^{-1} + k_\alpha^2 |z_0|^2 z^{-2}} \tag{5.9}$$

The parameter $0 < k_\alpha < 1$ is known as the pole contraction factor and specifies the bandwidth of the notch filter (Musumeci et al 2015). Thus, the transfer function of two-pole notch filter to mitigate the CW interference is

$$H(z) = H_{AR}(z) H_{MA}(z) = \frac{1 - 2R\{z_0\} z^{-1} + |z_0|^2 z^{-2}}{1 - 2k_\alpha R\{z_0\} z^{-1} + k_\alpha^2 |z_0|^2 z^{-2}} \tag{5.10}$$

The closer k_α to 1, the narrower notch filter is, which means a distortion reduction on the GNSS signal. The β parameter determines pole amplitude. In fact, the filter has two complex conjugate poles at $\beta k_\alpha e^{\pm j2\pi f_i}$. Since the stability condition for discrete-time systems mandates all poles to be inside the unit circle, $|\beta k_\alpha| < 1$ must be satisfied for the filter's proper operation.

Examples of notch filter frequency responses for different pole contraction factors are shown in Figure 5-7 where Fs, f_i and β are equal to 50MHz, 12.5 MHz and 0.999, respectively. In this case, the value of k_α cannot be chosen randomly close to 1 for stability reasons as mentioned above. According to Musumeci et al (2015), a k_α value of 0.85 provides the best jamming removal performance in terms of measured post-correlation SNR.

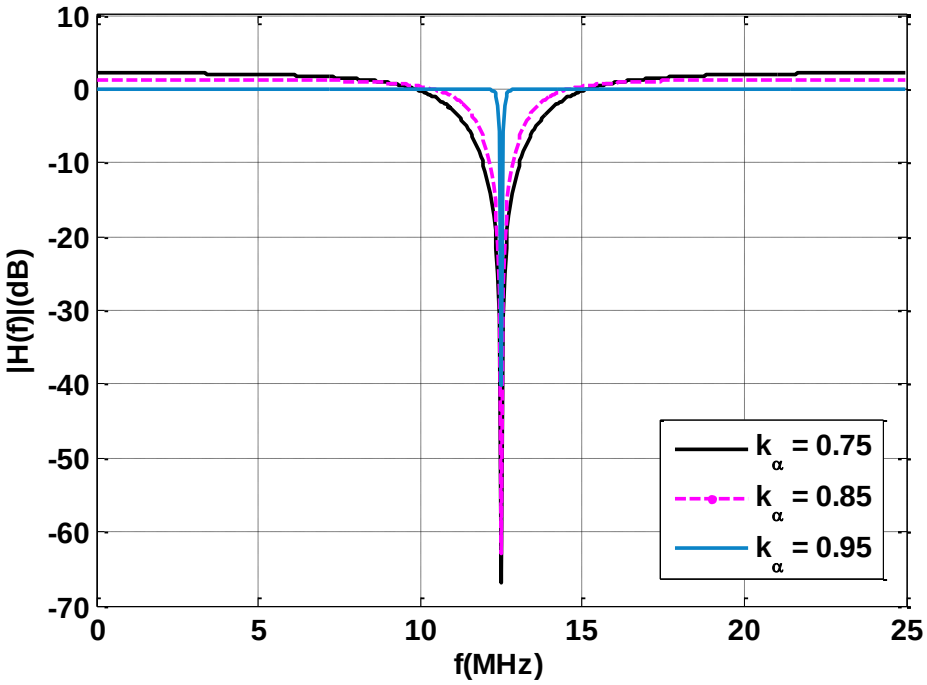

Figure 5-7 Notch filter frequency responses as a function of k_α

For a chirp-type jammer which sweeps around the receiver GNSS frequency band, the instantaneous jamming frequency obtained from any of proposed characterization methods in chapter 4 can be used to adjust the notch filter zero-pole location.

5.3 Jammer Synthesis Mitigation Method

The jammer synthesis methods generate a replica signal that is similar to the jammer. In fact, the replica is a noise-free version of the jammer and the mitigation is done by subtracting the replica from the received signal. The HHHT method is investigated in this category.

5.3.1 Hilbert-Huang Hough Transform (HHHT)

After characterizing the received signal using windowed-HHT, as discussed in Section 4.4.1, the signal parameters including chirp rate and instantaneous phase can be calculated using the Hough transform. The Hough transform is a pattern recognition method for calculating the number of points that satisfy a parametric constraint. It can be applied to the estimated angular frequency of HHT method. In order to calculate the angular frequency, Equation 4.23 can be rewritten as

$$\omega_i(n) = diff\left(\theta_i(n)\right) \tag{5.11}$$

where $diff(\ )$ represents the difference operation. The total Hilbert spectrum for all of the obtained IMFs (M) can be expressed as

$$H(\omega,n) = \sum_{i=1}^{M} a_i(n)\eta_i(n) \tag{5.12}$$

where n is the time variable and

$$\eta_i(n) = \begin{cases} 1, & \omega_i(n) = \omega \\ 0, & Otherwise \end{cases} \tag{5.13}$$

The Hilbert-Huang Hough transform is given by (Ye et al 2013)

$$h(\Theta) = \sum_{n=0}^{K-1} H(\omega,n) = \sum_{n=0}^{K-1} H\left(\omega(n;\Theta),n\right) \tag{5.14}$$

where K is the number of features to be estimated and $\omega(n;\Theta) = diff\left[\theta(n;\Theta)\right]$. For a linear chirp signal, the instantaneous phase $\theta(n;\Theta)$ can be written as

$$\theta(n;\Theta) = \omega_0 n + mn^2, \qquad \Theta = (\omega_0, m) \tag{5.15}$$

In the above expression, ω_0 represents the initial angular frequency and m is the chirp rate which are donated by Θ vector.

Figure 5-8 shows the block diagram of mitigation algorithm using the Hilbert-Huang Hough transform (HHHT) (Ye et al 2013).

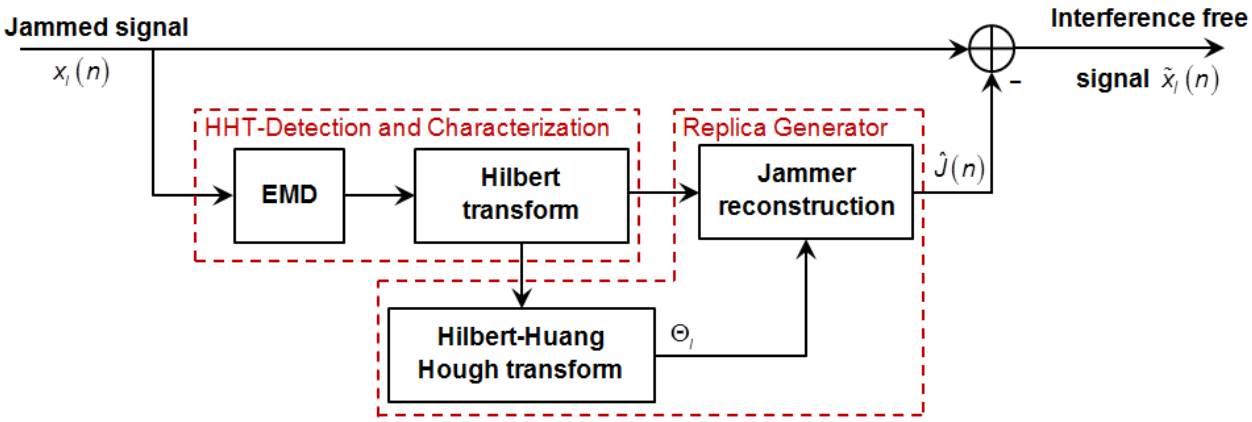

Figure 5-8 Jammer mitigation using Hilbert-Huang Hough transform

After decomposition the input signal into its IMFs, according to the flowchart of Figure 4-6 and calculating the Hilbert transform for each of IMF component, the Hilbert spectrum is calculated by Equation 5.9. Then, $h(\Theta)$ is obtained using the Hough transform, which is an iterative algorithm. At the l^{th} iteration, a search space is defined for the $\Theta_l = (\omega_{0l}, m_l)$ pair with quantized parameters. The candidate $\Theta_l = (\omega_{0l}, m_l)$ is determined, corresponding to the maximum of $h(\Theta)$. Hence, the l^{th} jammer component can be constructed as

$$\hat{J}_l(n) = H(\omega_{ol} + m_l n, n)\cos(\theta(\omega_{ol} + m_l n, n)) \tag{5.16}$$

The masking operation of lth maximum of $h(\Theta)$ is expressed as

$$\tilde{h}(\Theta) = h(\Theta)M(\Theta), \quad M(\Theta) = \begin{cases} 0, & \Theta \in R(\omega_{0l}, m_l) \\ 1, & \textit{Otherwise} \end{cases} \tag{5.17}$$

where $R(\omega_{0l}, m_l)$ is a narrowband region of the (ω_0, m) plane, centred at point (ω_{0l}, m_l). Repeating this routine, all chirp jammers can be estimated. Finally the interference free signal can be obtained by

$$\hat{x}_l(n) = x_1(n) - \hat{J}(n) \tag{5.18}$$

where $\hat{J}(n) = \sum_{l=1}^{K} \hat{J}_l(n)$ and K is the number of chirp components.

5.4 Simulation Results

In order to evaluate the performance of the proposed mitigation methods, GPS L1 C/A signals were received through a line of sight NovAtel 702 GG antenna and fed into a National Instrument (NI) RF front-end to collect raw IF samples at a 10 MHz sampling rate. The received signals were combined with a Group II chirp-like jammer generated by a MATLAB-based software simulator. The chirp signal has 12 μs sweep time and 5 MHz bandwidth. GSNRx^{TM} was employed to evaluate the performance of the GNSS receiver before and after interference mitigation. Figure 5-9 shows the block diagram of the data collection scenario where several datasets were considered with different jammer powers. Although it is possible to simulate the GPS signal in MATLAB, herein real data is used for convenience since all equipment and experience necessary were available. In addition, by utilizing real GPS signals, the effects of different parts of RF front-end such as front-end bandwidth and noise figure are also considered.

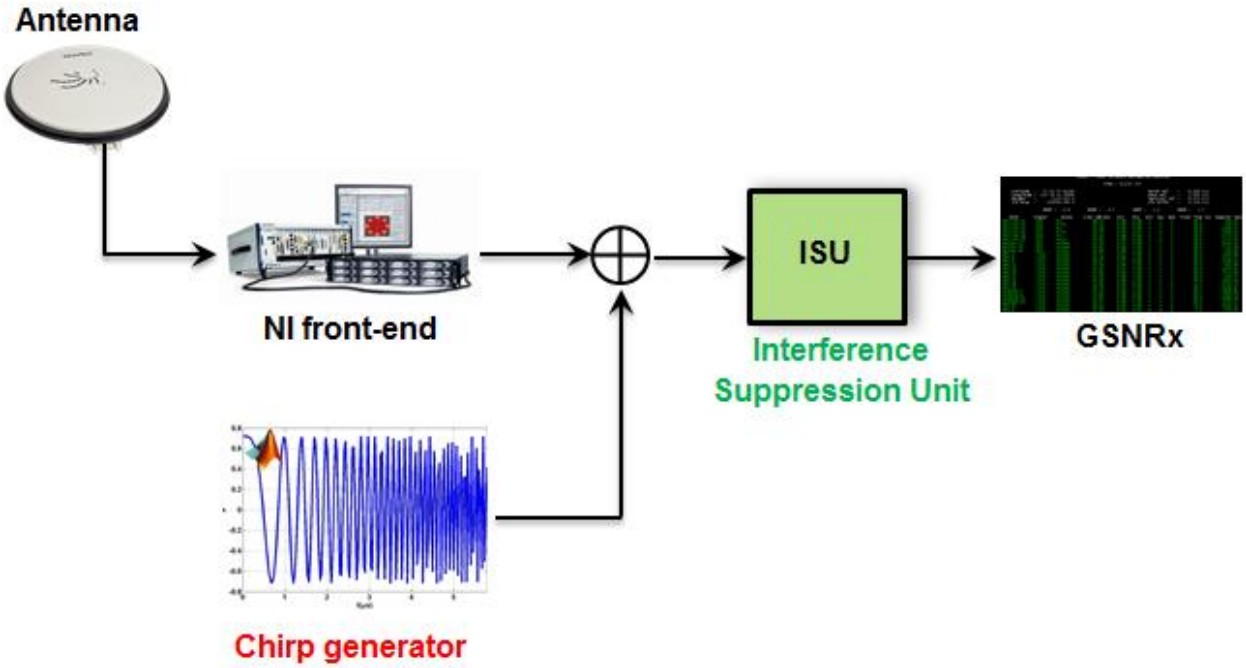

Figure 5-9 Block diagram of data collection

The simulated jammer was combined with the IF samples after 5 s from the beginning of data collection. This initial interference-free signal allows the acquisition block to function properly and let the GNSS receiver to move into tracking mode. The proposed method was applied to produce a new interference-free version of the signal. Herein, two scenarios were investigated with jammer powers to noise spectral density ratio (J/N_0) of 60 dB-Hz and 100 dB-Hz.

Figure 5-10 shows the results of estimated Carrier-to-Noise spectral density ratios (C/N_0) for different satellites (PRNs) in view when the received signals are interference-free. When a jammer is combined with the received signals, the effective C/N_0 for all satellites is reduced. In the rest of this chapter, PRN 7 is chosen for ISU performance assessment without loss of generality. Similar results are expected for other SVs.

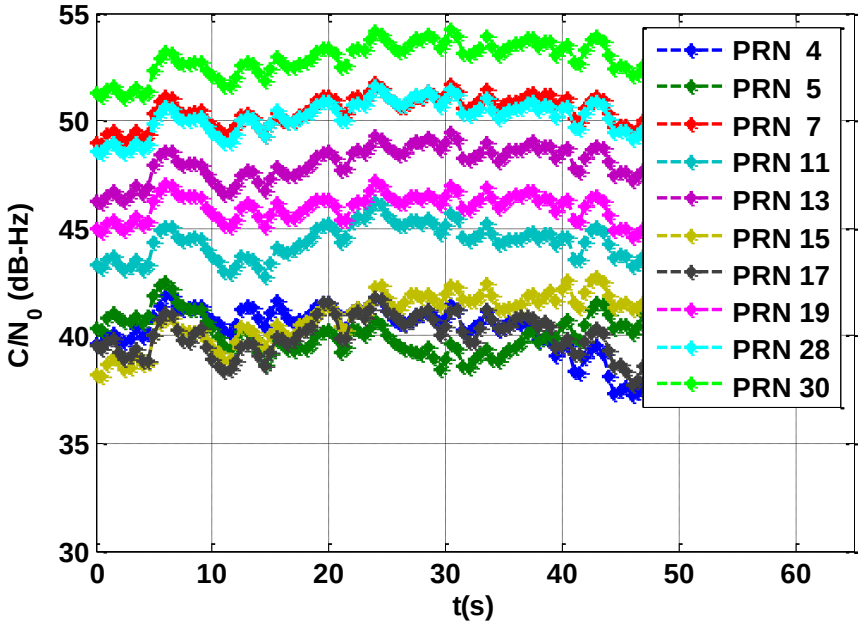

Figure 5-10 C/N_0 with respect to time for different available PRNs before adding jammer signals

Figure 5-11 shows the C/N_0 values for PRN 7 over time before and after adding different jammer powers with and without interference mitigation. The upper figure shows that adding a 60 dB-Hz jammer reduces the C/N_0 about 12 dB-Hz. It is observed that in this case the performance of the proposed mitigation methods is more or less the same. This jammer can be considered weak since the GNSS receiver is able to track the satellite signal. However, the performance of GNSS degrades in the presence of the jammer. In both FrFT and notch filtering methods, the STFT characterization approach is chosen to estimate the jammer properties. However, other characterization methods, described in Chapter 4, can also be used as the input of these mitigation methods.

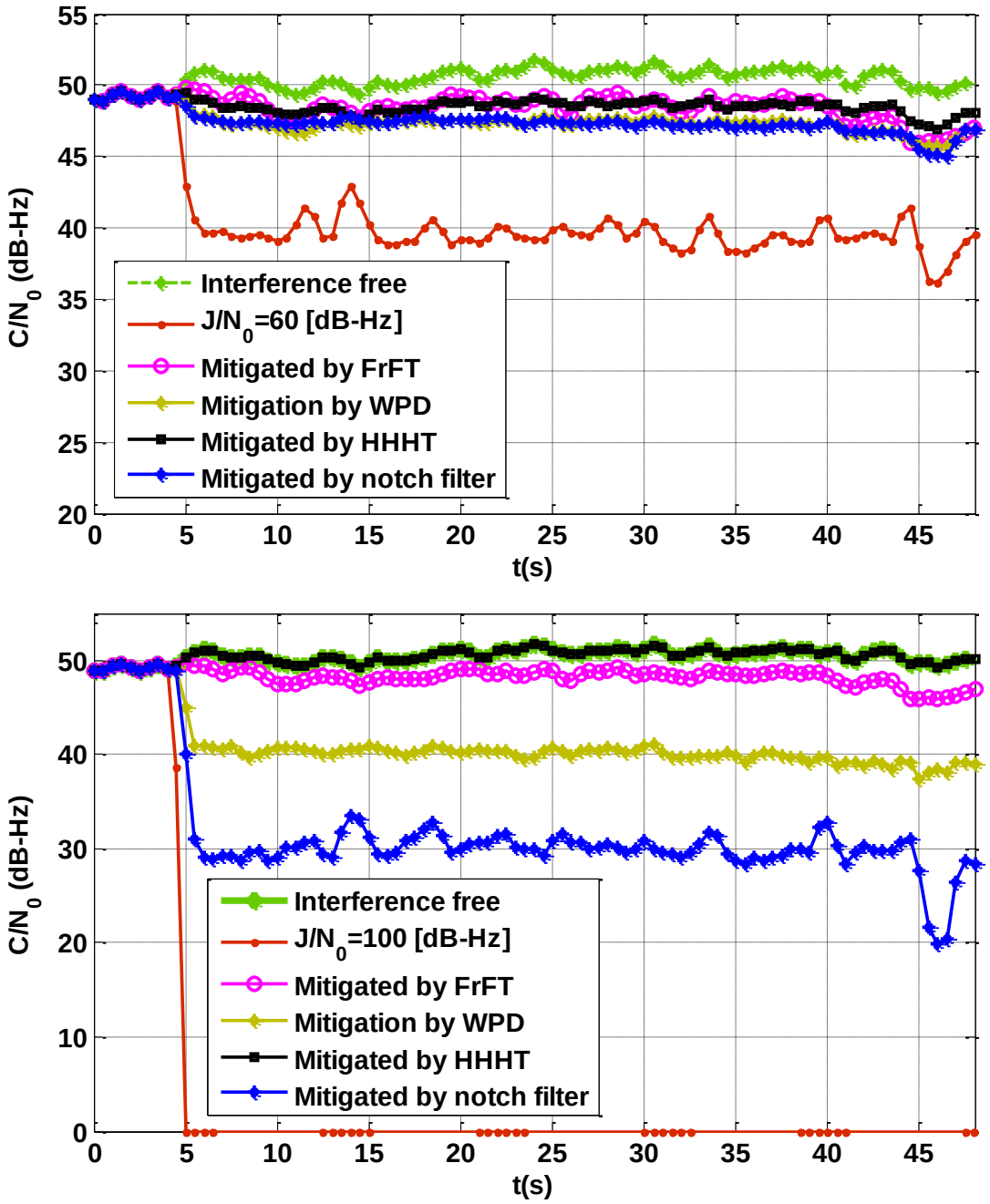

Figure 5-11 C/N_0 values before and after ISU unit for different J/N_0 values

The lower plot of Figure 5-11 depicts the effect of adding a 100 dB-Hz jammer to the GNSS signal. As observed, after 5 s the jammer negatively affected the signal severely such that the receiver is no longer able to track the signal. Increasing the J/N_0 to this level, FrFT and HHT methods are still capable of removing the effect of chirp-type

jammer well, but notch filter does not function properly. Comparing the two figures, increasing the J/N_0 value decreases the performance of FrFT, WT and notch filtering methods. However, it improves the efficiency of HHHT as it causes better estimation of chirp-rate of the jammer signal.

The upper plot of Figure 5-12 shows the results of Frequency lock indicator (FLI) for PRN 7 for different J/N_0 values. The FLI is a metric that indicates the stability of the received signal frequency (carrier Doppler in case of GNSS). This parameter is defined as (Van Dierendonck 1996)

$$FLI = \frac{dot^2 - cross^2}{dot^2 + cross^2} \tag{5.19}$$

where

$$\begin{aligned} cross &= i_{k-1} q_k - q_{k-1} i_k \\ dot &= i_k i_{k-1} + q_k q_{k-1} \end{aligned} \tag{5.20}$$

where i_k and q_k are the real and imaginary parts of the correlator output at k^{th} integration time epoch. FLI is measured by a number between 1 and -1 in which a value closer to 1 implies more stable frequency tracking.

Obviously, adding a jammer to the input signal degrades the FLI values in all the cases. For smaller J/N_0 values, all of the interference mitigation outputs lead to more stable estimates. Moreover, for a strong J/N_0 (100 dB-Hz), the FLI results of mitigation using HHT and FrFT are very close to one which shows that they are appropriate mitigation methods. However, the poor results of WT and notch filtering lead the GNSS tracker to lose lock.

The lower plot of Figure 5-12 shows the results of the phase lock indicator (PLI) for PRN 7 for 60 and 100 dB-Hz J/N_0 values. The PLI is a metric that indicates the stability of the received signal phase (carrier phase in case of GNSS). This parameter is defined as (Van Dierendonck 1996)

$$PLI = \frac{i_k^{\,2} - q_k^{\,2}}{i_k^{\,2} + q_k^{\,2}} \tag{5.21}$$

where i_k and q_k are observed real and imaginary parts of the correlator output at k^{th} integration time epoch. The estimated phase quality is measured by a number between -1 and 1. A value closer to 1 implies more stable phase tracking.

Similar to the FLI case, the PLI metric degrades significantly when a jammer is added to the signal. After RFI mitigation using FrFT and HHT, the PLI outputs for both J/N_0 are very close to one. However, notch filtering has a reasonable result merely for lower J/N_0 values. The performance of WT is worse than FrFT and HHT and better than notch filtering. The stable phase has a major advantage on providing a more accurate positioning solution as well as faster ambiguity resolution in high accuracy receivers.

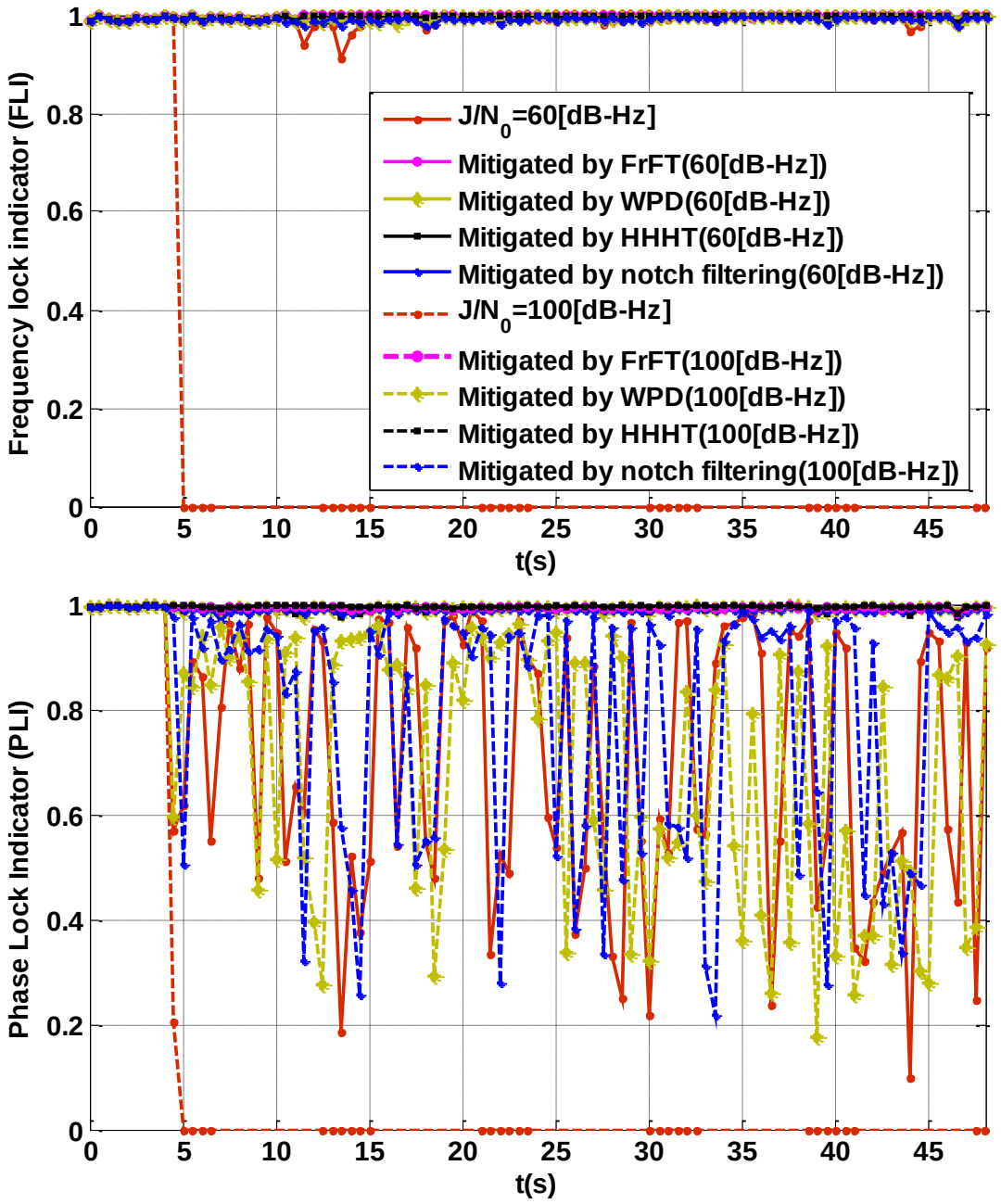

Figure 5-12 FLI and PLI before and after ISU for different JNRs

Figure 5-13 compares the performance of different jammer mitigation methods. Herein, the C/N_0 of the PRN 7 is employed as the assessment metric. The received signal has a strength of about 52 dB-Hz and is corrupted through a chirp jammer with different J/N_0 values. The notch filtering method has the worst performance as the output C/N_0 drops

severely when increasing the jammer power. As expected, the HHHT method exhibits the best performance by considering the fact that the jammer estimation is more precise as the J/N_0 increases. Using the WPD method, it is possible to mitigate jammers up to 120 dB-Hz. As it is shown, one might assume that the FrFT mitigation method is almost independent of jamming power. However, the performance of this method degrades for higher jammer power.

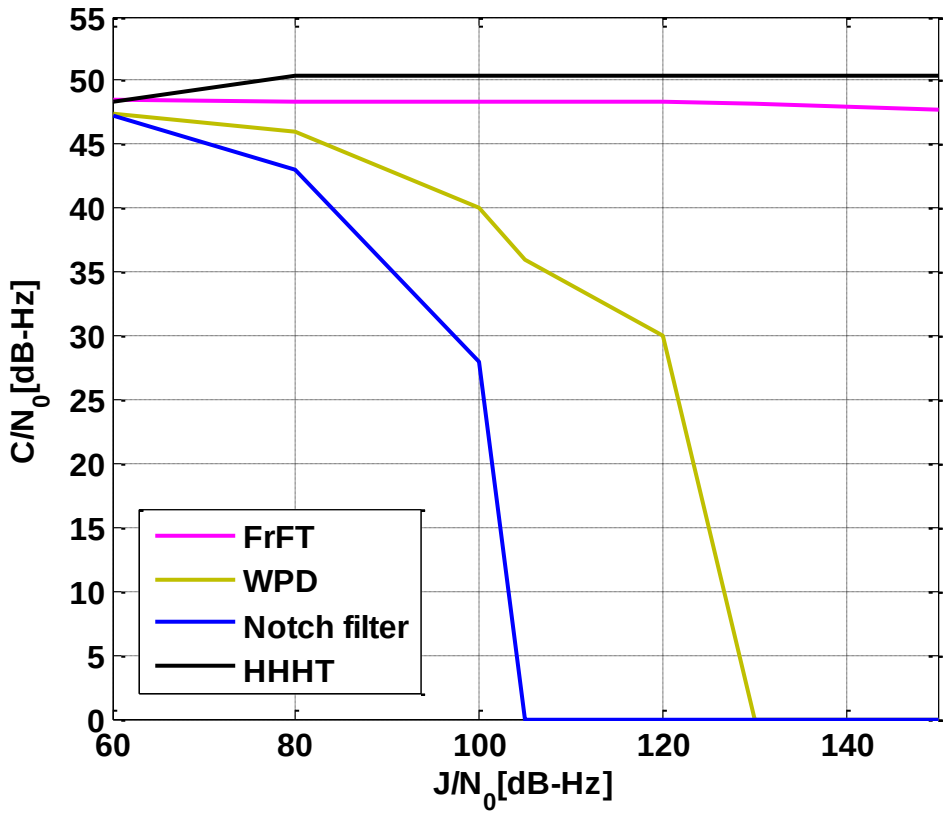

Figure 5-13 Performance comparison of different mitigation methods versus J/N_0 values

5.5 Computational Complexity

This section presents a short description on the computational complexity of the aforementioned mitigation algorithms. As mentioned in Section 4.5, the symbol $O(\ )$ represents the order of computational complexity.

The cost of FrFT is $N\log N$ which is the complexity of a FFT where N is the number of samples. Hence, the total computational load is in the order of $O(N\log N)$.

The complexity of WPD for input signal decomposition is described in Section 4.5 [$O(4NL)$where L and N are the number of FIR taps and samples respectively]. Since WPD requires the results of DWT characterization, the overall complexity of WPD is on the order of ($O(NL)$).

The same as for WPD, the complexity of Hilbert-Huang transform is expressed in Section 4.5. The cost of the mitigation method is roughly similar to the cost of HHT characterization. In fact, as only one straight line is estimated for the chirp jammer, the Hough transform can be implemented using a simple 1st order polynomial curve fitting for initial frequency and frequency-rate. Hence, its computational burden is much lower than that of HHT method.

Concerning the adaptive notch filtering complexity, a detailed analysis is provided in (Borio et al 2008) where the authors state that for each input sample, 5 sums, 6 products and 1 division are required for the ARMA part of notch filtering. Hence, the computational load of notch filtering for N input samples in of the order of $O(N)$.

Figure 5-14 provides a relative comparison among the computational complexity of different mitigation techniques. The execution time of each method is extracted by the MATLAB “profile” function on a Windows server 2012 PC with a CPU at 2.6 GHz and 32 GB of RAM. The computational requirement of each algorithm for the same data set is reported. For the simulations, the STFT characterization algorithm is used for both FrFT and notch filtering mitigation methods. It is observed that the lowest execution time

corresponds to notch filtering. Afterwards, the execution time of FrFT and WPD are higher than notch filtering. In addition, the most time-consuming algorithm is the HHHT method. For each method, the simulation was executed for 1000 times and the processing times were averaged and normalized. It should be mentioned that this is a rough estimation since these values depend on the computer architecture and algorithms implementation details.

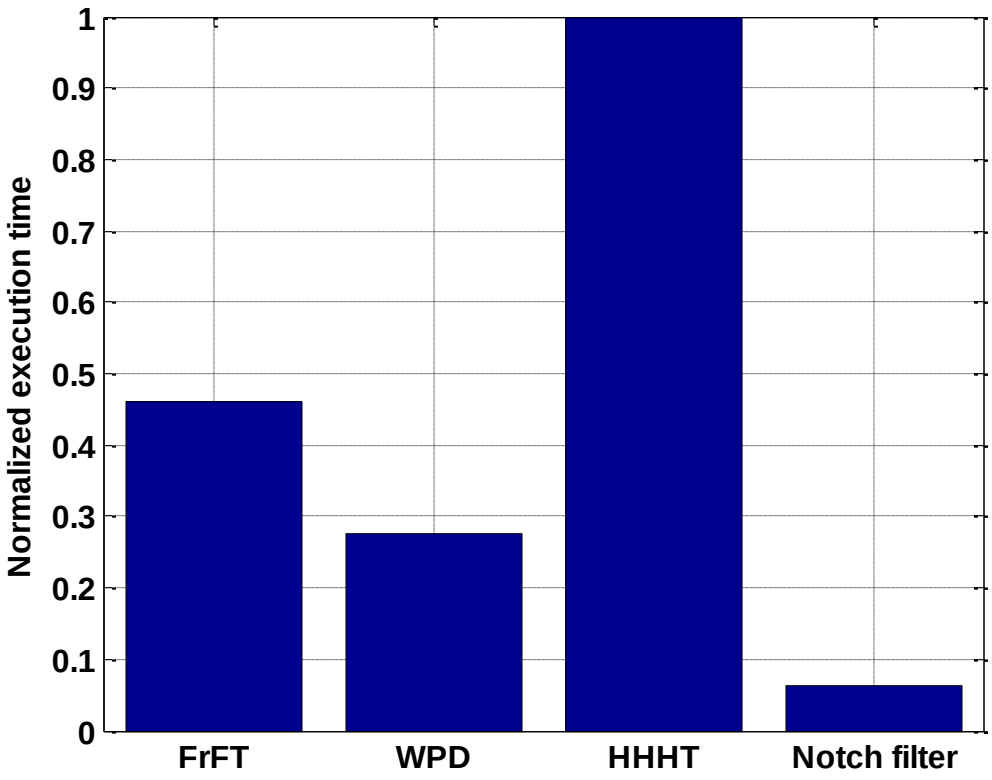

Figure 5-14 Normalized processing time for mitigation techniques

5.6 Summary

This chapter compared several main mitigation techniques for chirp-type interference sources on the GPS L1 C/A signal. Table 5-1**Error! Reference source not found.** summarizes the advantages, disadvantages and cost of the aforementioned methods.

Table 5-1 Comparison of mitigation methods

Method	Advantages	Disadvantages	Cost
FrFT	Simple structure, takes advantage of FFT	$\cot(\ )$ can take enormous values leading to an outlier	Moderate
WPD	Variable resolution	Scale factor must be assumed as a priori information, The characterization method must be DWT	Moderate
HHHT	High TFR resolution, adaptive signal decomposition, Improved performance for high power jammers	High computational burden	High
Notch Filtering	Low complexity, Adequate performance for CW jammers	Relatively poor mitigation for chirp-type jammers	Low

Chapter Six: Conclusions and Recommendations

This chapter summarizes the major findings of this research and presents concluding remarks. Recommendations for future work are also provided to enhance the research obtained so far.

6.1 Conclusions

The main goal was to investigate possible methods for civil RF jammer detection, characterization and mitigation. In this regard, chirp-type jammers were considered as they are widely used for service denial of GNSS receivers. To this end, various well-known temporal, spectral and joint time-frequency algorithms were implemented and evaluated for the sake of receiver functionality enhancement. The proposed ISU rejects the effects of RF jammers before the GNSS receiver processes the signal. The ISU operates at the pre-correlation level. The main advantage of a pre-correlation ISU is decoupling the interference suppression functionality from that of GNSS receiver. Hence, the receiver internal structure does not require any modification. It is especially useful considering the fact that end users do not incur any extra cost for receiver's upgrade or re-design.

Several jammer detection algorithms such as power content analysis (i.e. PLD), PSD analysis and normality analysis have been discussed. It was shown that the Welch spectrum analysis, as a PSD analysis method, provides an appropriate detection performance with low latency in the presence of narrowband interference. However, this method is of limited performance in the presence of wideband interference. Marti's method is a joint PSD/PDF analysis approach which works appropriately for different interference signals but at a higher computational cost. This method also needs some

clean data training sequence as well as enough data length (on the order of ms) for jammer detection. The PLD method is a high performance approach which is able to detect different types of interference based on the increased power content of received signals and with a low latency as well as very low computational complexity. An interference-free training dataset is required for proper threshold definition of PLD technique. Among normality analysis methods, the performance of GoF and Kurtosis were analysed and the results shows that the performance of the traditional GoF method is the same as that of the PLD and PSD methods. However, the performance of Kurtosis and the blind-GoF methods are lower than them.

Chirp-type jammer characterizations can be categorized into linear, bilinear and adaptive time-frequency methods. Considering the linear class, it was shown that STFT had the least computational complexity at the cost of a constant time-frequency resolution. In fact, it suffers from the uncertainty principle and provides a coarse estimation of the instantaneous frequency, especially in the case of chirps with short sweep times. For the Wavelet transform, an appropriate Wavelet function has to be selected to match the signal structure. Otherwise, an improper function may yield misleading diagnosis results. The advantage of WT is its ability to characterize jammers with short sweep times with more than one chirps in each window and thereby abrupt frequency changes occur. The accuracy of S-transform method is better than that of WT at the cost of high computational complexity even if the FFT is utilized for fast calculations. In addition, S-transform does not require any a priori knowledge about the jammer properties in contrast to WT which a proper Wavelet function must be chosen beforehand.

Bilinear jammer characterization algorithms are all based on the WVD and thus are subject to the inherent cross-term interference. For multi-component signals, a priori knowledge about signal structure is necessary to identify the true components. Optimal kernel methods (i.e. Cohen distribution) can be utilized to effectively suppress cross-terms and improve time-frequency resolution at the cost of increased complexity.

In the case of adaptive characterization methods, the windowed HHT requires the least a priori knowledge about the signal properties and gives an adequate resolution. However, its computational load in comparison with the linear TFR method is high. The matching pursuit method works based on atomic decomposition. The procedure requires a proper time-frequency dictionary to be pre-constructed according to the signal structure which is often computationally demanding. Nevertheless, this method might be a good choice for multi-component signals with complex time-frequency structure provided that the signal structure is known.

This research compared the performance of four different jammer mitigation techniques, namely FrFT, WPD, HHHT and notch filtering. Two chirp-type jammer signals with J/N_0 equal to 60 dB-Hz and 100 dB-Hz were used to test the mitigation methods. In the case when no excision method is applied, the receiver is jammed; hence the signal tracking loses lock.

It was demonstrated that applying the proposed methods result in improvement in the performance of GNSS signal tracking in terms of the estimated C/N_0. The FrFT method can take advantage of the FFT operator and requires moderate computational load compared to other methods. The mitigation can properly reject both kinds of moderate and severe jammers.

It was shown that the effective range of J/N_0 which WPD is able to remove is less than HHT and FrFT but more than notch filtering. Although the WPD computational load is moderate, the disadvantages of this method are the requirement for a priori knowledge about the properties of jammer signal to choose an appropriate scale and its requirement for using DWT for signal characterization. The benefits of the HHHT method are high time-frequency resolution and its adaptive nature which implies that no knowledge of the jammer signal structure is required. However, it is very computationally demanding. Notch filtering is the simplest mitigation method which needs very few operations at the expense of the poorest performance.

One of the key questions regarding aforementioned methods is the possibility of their implementation and usage in real-time. Obviously, the answer to this question depends on the hardware platform as well as the level of software/firmware availability. Nowadays, there are powerful processors available in mobile units such as smartphones that can alleviate the computational requirement barrier for advanced signal processing algorithms. For example, Qualcomm Snapdragon 800 series, used in scores of smartphones, such as the Samsung Galaxy series, have four to eight cores running at 2-2.5 GHz. This computational power is comparable with those of laptops and even personal computers and makes these devises ideal for more complex signal processing tasks. In this research, a MATLAB profile function is used to evaluate the execution time of each algorithm on a personal computer. If the execution time of a block of data is less than the length of that data for a specific algorithm, real-time processing is feasible. The notch filtering, WPD and FrFT are able to operate in real-time. Another important factor for the execution time is the language with which the

algorithm is implemented and the optimality of the code. Herein, a high level interpreter programming language (MATLAB) is used which is convenient for rapid prototyping but slow in run-time. In contrast, using low level compiler languages such as C and assembly and utilizing optimized libraries can reduce the execution time significantly. Therefore, it is still possible to employ more complex methods such as HHHT in real time.

6.2 Recommendations for Future Work

Following the above findings, the following recommendations are proposed for potential future work:

1. This research has focused on single saw-tooth chirp-type jammers which can be characterized by their initial frequency and frequency slope parameters. A more general case of multiple saw-tooth chirp jammers could also be considered for ISU design and evaluation. For instance, as mentioned by Alkishriwo (2013), FrFT is unable to mitigate two chirps happening simultaneously. In this case, the use of other methods or modifications to the proposed ones must be investigated.
2. The performance of ISU techniques have evaluated for only GPS L1 C/A signals. However, applying these methods to other GNSS can help quantify better the performance of ISU functionality. Moreover, other metrics such as GNSS measurements (e.g. carrier phase and Doppler) and/or positioning accuracy may also be considered for performance analysis. It is especially of interest when comparing the performance of jamming mitigation techniques for FDMA signals (e.g. GLONASS) with those of CDMA ones.

3. It is very informative to investigate the estimation accuracy lower bounds. In this way, it is possible to determine how well these characterization methods operate compared to the theoretical limits.
4. Cohen distribution and matching pursuit methods were introduced in order to eliminate the effect of WVD cross-terms. Due to the high complexity of these methods, investigations using distributions with lower complexity would be of interest.
5. Future research could be conducted using a real RF chirp jammer. In this case, the true RF jammer would be combined to the GNSS signal and fed into the ISU. In this way, jammer impairments such as its oscillator frequency drifts are also included. Moreover, the other unaccounted effects such as ADC saturation, limited number of ADC bits, etc. can also be investigated.

References

Abdizadeh, M (2013) *GNSS Signal Acquisition in The Presence of Narrowband Interference*, PhD thesis, Report No. 203888, Department of Geomatics Engineering, University of Calgary, Calgary, Alberta, Canada, pp. 24- 25.

Ahmed, F. M., K. A. Elbarbary, and A. R. H. Elbardawiny (2006) "Detection of sinusoidal signals in frequency domain." In *IEEE CIE'06. International Conference on Radar,* Cairo, Egypt, pp. 1-5.

Alkishriwo, O. A. S (2013) *The Discrete Linear Chirp Transform and Its Applications*, PhD Thesis, Department of Electrical and Computer Engineering, University of Pittsburgh, USA, pp. 27-34.

Atapattu, S., C. Tellambura, and H. Jiang (2014) “Conventional Energy Detector,” [Chapter 2] in *Energy Detection for Spectrum Sensing in Cognitive Radio*, SpringerBriefs in Computer Science, New York, NY, USA.

Auger, F., and P. Flandrin (1995) “Improving the readability of time–frequency and time-scale representations by the reassignment method,” *IEEE Trans. SignalProcess.*, vol. 43, no. 5, pp. 1068–1089.

Ayaz, A. S. (2013) Weak and Degraded Signal Acquisition Techniques in GNSS Software Receiver, PhD thesis, Department of Aerospace Engineering, UNIVERSITÄT DER BUNDESWEHR, Munich, Germany, pp. 88- 114.

Balaei, A. T. (2007) *Detection, Characterization and Mitigation of Interference in Receivers for GNSS*, PhD Thesis, Department of Electrical Engineering, University of New South Wales, Sydney, Australia, pp. 65-86.

Bauernfeind, R., and B. Eissfeller (2014), “Softwrare-Defined Radio based Roadside Jammer Detector: Architecture and Results,” in *Position, Location and Navigation Symposium - PLANS 2014, 2014 IEEE/ION,* May 2014, pp. 1293 – 1300, doi: 10.1109/PLANS.2014.6851504

Bauernfeind, T. Kraus, A. S. Ayaz, D. Dotterbock and B. Eissfeller (2012), “Analysis, Detection and Mitigation of Incar GNSS Jammer Interference in Intelligent Transport Systems,” in *Deutscher Luft Raumfahrtkongress*. *Document ID. 281260*, 10 pages.

Betz, J. W. (2001) “Effect of partial-band interference on receiver estimation of C/N0: Theory” in *Proceedings of ION 2001*, Long Beach, CA, Jan. 22-24, pp. 872-881.

Boashash, B. (2002) *Time-Frequency Signal Analysis and Processing*, Prentice Hall, New York.

Borio. D (2010) “GNSS acquisition in the presence of continuous wave interference,” *IEEE Transactions on Aerospace and Electronic Systems*, vol. 46, no. 1, pp. 47–60.

Borio, D., L. Camoriano, and L. Lo Presti (2008) “Two Pole and Multi Pole Notch Filters: A Computationally Effective Solution for GNSS Interference Detection and Mitigation,” in *IEEE Systems Journal*, Vol. 2, No. 1, pp. 38-47.

Borowski, H., O. Isoz, F. M. Eklöf, S. Lo and D. Akos (2006) "Detecting False Signals with Automatic Gain Control," *GPS World,* vol. 23, no. 4, pp. 38-43.

Bultan, A. (1999) “A four-parameter atomic decomposition of chirplets”, IEEE Trans. Signal Process. 47, pp. 731–744.

Capozza P. T., B. J. Holland, T. M. Hopkinson and R. L. Landrau (2000) “A Single-Chip Narrow-Band Frequency-Domain Excisor for a Global Positioning System (GPS) Receiver,” in *IEEE Journal of Solid State Circuits. vol. 35, no. 3,* pp. 401–411.

Cardoso, J. G. Ruano and P. Fish (1996), “Nonstationary Broadening Reduction in Pulsed Doppler Spectrum Measurements Using Time-Frequency Estimators,” in *IEEE Transactions on Biomedical Engineering*. vol.43, no.12, pp.1176-1186.

Chen, S.S., D.L. Donoho and M.A. Saunders (1998) “Atomic decomposition by basis pursuit”, SIAM J. Sci. Comput. 20, pp. 33–61.

Choi, H.-I., Williams, W.J. (1989) "Improved time-frequency representation of multicomponent signals using exponential kernels," in *Acoustics, Speech and Signal Processing, IEEE Transactions on* , vol.37, no.6, pp.862-871, Jun 1989

Cohen, L., (1989) *Time–frequency distributions: a review*, Proc. IEEE 77, pp. 941–981.

Cohen, L., (1995) *Time-Frequency Analysis*, Prentice Hall, Englewood Cliffs, NJ.

Cui. J., W. Wong, and S. Mann (2005) “Time-frequency analysis of visual evoked potentials using chirplet transform,” *Electron. Lett.*, vol. 41, no. 4, pp. 217–218.

Cui, J., and Wong, W (2006) "Optimal Window Length in the Windowed Adaptive Chirplet Analysis of Visual Evoked Potentials," in *Engineering in Medicine and Biology Society, 2006. EMBS '06. 28th Annual International Conference of the IEEE* , vol., no., pp. 4580 - 4583.

De Bruijn, N. G., *Uncertainty principles in Fourier analysis*, Inequalities, Academic Press, New York, 1967.

De Roo, R. D., S. Misra, and C. S. Ruf (2007) “Sensitivity of the Kurtosis Statistic as a Detector of Pulsed Sinusoidal RFI,” in *IEEE Trans. on Geoscience and Remote Sensing*, July 2007, vol. 45, no. 7, pp. 1938-1946.

Dovis, F. (Ed.). (2015). *GNSS Interference Threats and Countermeasures*. Artech House, Boston, USA.

DragoSeviC, M. V. and S. S. Stankovic (1995) “An Adaptive Notch Filter with Improved Tracking Properties,” in *Transaction of Signal Processing. vol. 43, no. 9,* pp. 2068–2078.

Duda, R. O. and P. E. Hart (1972) “Use of the Hough transformation to detect lines and curves in pictures,” in *Communications of the ACM*, vol. 15, no. 1, pp. 11–15.

Flandrin, P (1999) *Time-Frequency/Time-Scale Analysis*, Academic Press, San Diego, CA.

Flandrin, P., F. Auger, and E. Chassande-Mottin (2003) “Time-frequency reassignment: From priciples to algorithms,” *Appl. Time-Frequency Signal Process.*, vol. 5, pp. 179–203.

Rioul, O., and P. Flandrin (1992) "Time-scale energy distributions: a general class extending wavelet transforms," in *Signal Processing, IEEE Transactions on* , vol.40, no.7, pp.1746-1757.

Feng, Z., M. Liang and F. Chu (2013) “Recent Advances in Time-Frequency Analysis Methods for Machinery Fault Diagnosis: A Review with Application Example,” in *Mechanical Systems and Signal Processing of Elsevier journal,* March 13, no. 38, pp. 165-205.

Gardner, W. A (1988) *Statistical Spectral Analysis a Nonprobabilistic Theory*, Prentice Hall, New Jersey, USA.

Garcia-Nocettif, F., J. Solano Gonzalez, E. Rubio Acosta, and E. Moreno Hernandez (2002) "High performance computing of time frequency distributions for Doppler ultrasound signal analysis." In *World Congress*, vol. 15, no. 1, pp. 961-961.

Graps, A., (1995) "An introduction to wavelets." *Computational Science & Engineering, IEEE* 2, no. 2, pp. 50-61.

Grochenig, K (2000) *Foundations of Time-Frequency Analysis*, Birkhauser, Basel.

Gu, Y., and M. H. Bollen (2000) “Time-frequency and time-scale domain analysis of voltage disturbances,” in *Power Delivery, IEEE Transactions on*, vol.15, no.4, pp. 1279-1284.

Hess-Nielsen, N., and Wickerhauser, M.V. (1996) "Wavelets and time-frequency analysis", in *Proceedings of the IEEE*, Apr 1996, vol.84, no.4, pp.523-540.

Hlawatsch, F., and G. F. Boudreaux-Bartels (1992) “Linear and quadratic time-frequency signal representations”, in *IEEE Signal Processing Magazine*, April 1992, vol. 9, no. 2, pp. 21-67.

Huang, N. E., Z. Shen (1998) “The empirical mode decomposition and the hilbert spectrum for non-linear non-stationary time series analysis”. In *Proceedings R. Soc*., London.

Huang, N. E., Z. Wu (2008) “A review on Hilbert–Huang transform: method and its applications to geophysical studies” Rev. Geophys. 46 (2008) 1–23. RG2006.

ICD-GPS-200 (2000) Navstar GPS Segment / Navigation User Interface, Interface Control Document.

Irsigler, M., Avila-Rodriguez, J. A., and Hein, G. (2005) “Criteria for GNSS multipath performance assessment,” in *Proceedings of the 18th International Technical Meeting of the Satellite Division of The Institute of Navigation* (ION GNSS 2005), Long Beach, CA, Sept. 13-16, 2005, pp. 2166-2177.

Jachan, M., G. Matz and F. Hlawatsch (2007) “Time–frequency ARMA models and parameter estimators for underspread nonstationary random processes,” in IEEE Trans. Signal Process. 55 (9) (2007), pp. 4366–4381.

Jafarnia-Jahromi, A. Broumandan, S. Daneshmand, and G. Lachapelle (2015) “Vulnerability Analysis of Civilian L1/E1 GNSS Signals against Different Types of Interference,” in *processing of ION GNSS+2015*, Tampa, FL, Sept 14-18, 10 Pages.

Jafarnia-Jahromi, A., N. Fadaei, S. Daneshmand, A. Broumandan, and G. Lachapelle (2015) “A Review of Pre-despreading GNSS Interference Detection Techniques,” in 5th ESA International Colloquium Scientific and Fundamental Aspects of the Galileo, 27-29 Oct, Braunschweig, Germany, 8 Pages.

Jiang, X., and S. Mahadevan (2011) “Wavelet Spectrum Analysis approach to model validation of dynamic systems,” in *Mechanical Systems and Signal Processing*, 25(2011)575-590

Kaplan, E. D., and C. J. Hegarty (2006) *Understanding GPS Principles and Applications*, Artech House, Boston, London, pp. 243-281.

Kay, S. M (2009) *Fundamentals of statistical signal processing Volume II Detection Theory*, Prentice Hall PTR, Upper Saddle River, New Jersey, USA, 14th publication.

Landry, R. J., and A. Renard (1997) “Analysis of potential interference sources and assessment of present solutions for GPS/GNSS receivers,” in *4th Saint Petersburg International Conference on Integrated Navigation Systems*, Saint Petersburg, Russia, May 26-28.

Lehtomäki, J. (2005) *Analysis of energy based signal detection*, PhD Thesis, Faculty of Technology, University of Oulu, Oulu, Finland.

Lerga, J., and V. Sucic (2009) “Nonlinear IF estimation based on the pseudo WVD adapted using the improved sliding pairwise ICI rule,” *IEEE Signal Process. Lett.*, vol. 16, no. 11, pp. 953–956.

Liu Ming cai. *The wavelet analysis and its application*, Tsinghua university press,2005.9

Lung, M. L., W. J. Ma, Y. R. Chien and C. H. Ku (2011) “New Adaptive All-pass Based Notch Filter for Narrowband/FM Anti-jamming GPS Receivers,” in *Journal of Circuits, Systems, and Signal Processing*, Volume 30, Number 3, pp. 527-542.

Mallat, S.G (2009) *A Wavelet Tour of Signal Processing: the sparse way*, Academic Press, San Diego, CA, 2009.

Mallat, S.G. and Z. Zhang (1993) “Matching pursuit with time-frequency dictionaries,” *in IEEE Transactions on Signal Processing*, vol. 41, pp. 3397- 3415.

Mann, S., and S. Haykin (1992) “Chirplets’ and ‘warblets’: Novel time-frequency methods,” *Electron. Lett.*, vol. 28, no. 2, pp. 114–116.

Mann, S., and Haykin, S. (1995). The chirplet transform: Physical considerations. *Signal Processing, IEEE Transactions on*, *43*(11), 2745-2761.

Marti L. M. (2004) *Global Positioning System Interference and Satellite Anomalous Event Monitor*, PhD Thesis, Department of Electrical, Ohio University, Athens, Ohio, US, PP. 68-129.

McBride, A. C., and F. H. Kerr (1987) “On Namias's fractional Fourier transforms,” in *IMA Journal of applied mathematics* 39, no. 2, pp.159-175.

Meyer, Y., *Wavelets Algorithms and Applications*, Society for Industrial and Applied Mathematics, 1993.

Mihovilovic, D., and R. Bracewell (1991) “Adaptive chirplet representation of signals on time-frequency plane,” *Electron. Lett.*, vol. 27, no. 13, pp. 1159–116.

Misra, P., and P. Enge. Global Positioning System, Signals, Measurements and Performance, volume 2. Ganga-Jamuna Press, 1996. ISBN 0-9709544-1-7.

Mitch, R. H., R. C. Dougherty, M. L. Psiaki, S. P. Powell, B. W. O’Hanlon, J. A. Bhatti and T. E. Humphreys (2011) “Signal Characteristics of Civil GPS Jammers,” in *Proceedings of ION GNSS 2011*, 13 pages.

Montloin, L. (2010) *Impact of interference mitigation techniques on a GNSS receiver*, MSc Thsis, Ingenieur de l’Ecole Nationale de l’Aviation Civile, Sep. 2010.

Montgomery, P., T. Humphreys and B. Ledvina (2009) “A multi-antenna defense: Receiver autonomous GPS spoofing detection,” *Inside GNSS,* vol. 4, no. 2, pp. 40-46.

Motella, B., and L. Presti (2014) “Methods of goodness of fit for GNSS interference detection,” in *IEEE Transactions on Aerospace and Electronic Systems,* vol. 50, no. 3, pp. 1690-1700.

Nam, S (2013) “An Uncertainty Principle for Discrete Signals,” in *arXiv Journal,* July 24th, 4 pages.

Namias, Victor (1980) “The fractional order Fourier transform and its application to quantum mechanics,” in *IMA Journal of Applied Mathematics* 25, no. 3, pp. 241-265.

Ndili, A., and P. Enge (1998) “GPS receiver autonomous interference detection,” in Proceedings IEEE/ION Position Location and Navigation Symposium (PLANS), April 1998, vol. 123, no. 130, pp. 20-23.

Nighswander, T., R. Brumely, B. Ledvina, D. Brumely and J. Diamond (2012) “GPS Software Attacks,” in *CCS’ 12*, 16-18 October, 12 pages, Raleigh, North California, USA.

Ouyang, X. and M. G. Amin (2001) “Short-time Fourier transform receiver for non-stationary interference excision in direct sequence spread spectrum communications,” IEEE Trans. Signal Processing, April 2001, vol. 49, no. 4, pp. 851–863.

Ozaktas, H., (1996) “Digital computation of the Fractional Fourier Transform,” in *IEEE Signal Processing Transactions, Vol. 44, No 9*.

Papandreou-Suppappola, A., (2003.) *Applications in Time-Frequency Signal Processing*, CRC Press, Boca Raton, FL.

Petovello, M. G., C. O’Driscoll, G. Lachapelle, D. Borio, H. Murtaza (2008) “Architecture and Benefits of an Advanced GNSS Software Receiver,” in *International Symposium on GPS/GNSS*, November 2008, Tokyo, Japan, 11pages.

Pinnegar, C. Robert, and David W. Eaton (2003) "Application of the S transform to prestack noise attenuation filtering." *Journal of Geophysical Research: Solid Earth* 108, no. B9.

Poor, H. V (1994) *An Introduction to Signal Detection and Estimation*, Springer-Verlag, New York, USA.

Poularikas, Alexander D. (2010) ed. *Transforms and applications handbook*. CRC Press.

Qian, S., D. Chen (1996) *Joint Time-Frequency Analysis- Methods and Applications*, Prentice Hall, Engle wood Cliffs, NJ.

Qian, S. and D.P. Chen (1994) “Signal representation using adaptive normalized Gaussian functions,” in *Signal Processing*, vol. 36, pp. 1-11.

Qiu, L. (1993) "Wigner-Ville distribution and windowed Wigner-Ville distribution of noisy signals," in *Networks, 1993. International Conference on Information Engineering '93. 'Communications and Networks for the Year 2000', Proceedings of IEEE Singapore International Conference on* , vol.1, no., pp.388-392 vol.1. doi: 10.1109/SICON.1993.515792

Saarnisaari, H. (2004) “Consecutive mean excision algorithms in narrowband or short time interference mitigation,” *Position Location and Navigation Symposium 2004. PLANS 2004*, pp, 447-454, doi: 10.1109/PLANS.2004.1309028

Smith, S. (2005) “The local mean decomposition and its application to EGG perception data,” in J. R. Sec. Interference 2, pp. 443-454.

Stankovic, L., and V. Katkovnik (2000) “Instantaneous frequency estimation using higher order L-Wigner distributions with data-driven order and window length,” *IEEE Trans. Inf. Theory*, vol. 46, no. 1, pp. 302–311.

Stockwell, R. G. (2007) “A Basis for Efficient Representation of the S-transform”, in *Digital Signal Processing*, vol. 17, no. 1, pp. 371-393.

Stockwell, R. G., L. Mansinha, and R. P. Lowe (1996) “Localization of the complex spectrum: The S transform,” in *IEEE Trans. on Signal Processing*, vol. 44, no. 4, pp. 998-1001.

Tani, A., and R. Fantacci (2008) "Performance evaluation of a pre-correlation interference detection algorithm for the GNSS based on non-parametrical spectral estimation," in *IEEE Systems Journal,* Mar. 2008, vol. 2, no. 1, pp. 20-26.

Tarongi Bauza, J. M. (2012). *Radio frequency interference in microwave radiometry: statistical analysis and study of techniques for detection and mitigation,* PhD Thesis, Department of Signal Theory and Communications, Universitat Politecnica de Catalunya – Barcelona Tech, Spain, pp. 51 - 80.

Tarongi Bauza, J. M., and A. Camps (2010) "Normality Analysis for RFI Detection in Microwave Radiometry," in *Remote Sensing Journal,* Feb. 2010, pp. 191-210, doi: 10.3390/rs2010191.

Tazebay, M. V. and A. N. Akansu (1998) “A performance analysis of interference excision techniques in direct sequence spread spectrum communications,” IEEE Trans. Signal Processing, September, vol. 46, no. 9, pp. 2530–2535.

Titus, L. B. M., J. W. Betz, C. J. Hegarty, R. Owen (2003) “Inter-system and intra-system interference analysis methodology,” in *Proceedings of the 16th International*

Technical Meeting of the Satellite Division of The Institute of Navigation (ION GPS/GNSS 2003), Portland, OR, 9-12 September, pp. 2061-2069.

Tsui, J. B. Y. (2005) *Acquisition of GPS C/A Code Signals*, John Wiley & Sons, Inc., Hoboken, NJ, Chapter 2.

Urkowitz, H. (1967) "Energy detection of unknown deterministic signals," in *Proceedings IEEE,* April 1967, vol. 55, p. 523–531.

Van Dierendonck, A. J. (1996) “GPS Receivers,” in Global Positioning System: Theory and Applications, B. W. Parkinson and J. J. Spilker Jr, Eds., vol. 1. American Institute of Aeronautics and Astronautics (AIAA), 1996, pp. 329–407

Van Trees, H. L. (2001). *Detection, estimation, and modulation theory Part I*. John Wiley & Sons Inc, New York, USA.

Vaydianathan, P.P. (1990) “Multirate Digital Filters, Filter Banks, Polyphase Networks, and Applications: A tutorial,” in *Processing of the IEEE*, vol. 78, no. 1, pp. 56-93.

Yang, Y., Peng, Z. K., Dong, X. J., Zhang, W. M., & Meng, G. (2014). General parameterized time-frequency transform. *Signal Processing, IEEE Transactions on*, *62*(11), 2751-2764.

Yin, Q., S. Qian and A. Feng (2002) “A fast refinement for adaptive Gaussian chirplet decomposition”, IEEE Trans. Signal Process. 50, pp. 1298–1306.

Yun, L., X. Xiaochun, L. Bin, and P. Jingfeng (2013) “Time-frequency Analysis Based on the S-transform,” in *International Journal of Signal Processing and Pattern Recognition*, Vol.6, No.5, pp. 245-254.

Zou, H., Y. Chen, J. Zhu, Q. Dai, G. Wu and Y. Li (2004) “Steady-motion-based Dopplerlet transform Application to the estimation of range and speed of a moving sound source”, IEEE J. Ocean. Eng. 29 (3) (2004), pp. 887–905.

Zou, H., Q. Dai, R. Wang and Y. Li (2001) “Parametric TFR via windowed exponential frequency modulated atoms”, IEEE Signal Process. Lett. 8 (2001), pp.140–142.